COPERNICUS SPACE COMPONENT SENTINEL OPTICAL IMAGING

MISSION PERFORMANCE CLUSTER SERVICE

Data Quality Report

Sentinel-3 OLCI

April 2024

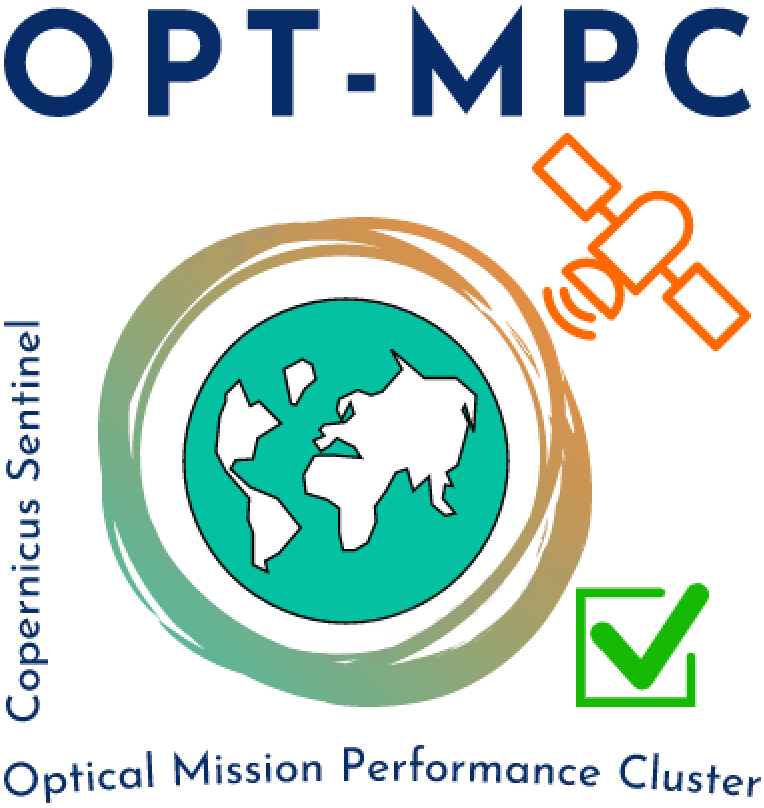

Ref.: OMPC.ACR.DQR.03.04-2024
Issue: 1.0
Date: 13/05/2024
Contract: 4000136252/21/I-BG

Customer:	ESA	**Document Ref.:**	OMPC.ACR.DQR.03.04-2024
Contract No.:	4000136252/21/I-BG	**Date:**	13/05/2024
		Issue:	1.0

Project:	COPERNICUS SPACE COMPONENT SENTINEL OPTICAL IMAGING MISSION PERFORMANCE CLUSTER SERVICE		
Title:	Data Quality Report - OLCI		
Author(s):	OLCI ESL team		
Approved by:	L. Bourg, OPT-MPC OLCI ESL Coordinator S. Clerc, OPT-MPC Optical ESL Coordinator	**Authorized by**	C. Henocq, OPT-MPC S3 Technical Manager
Distribution:	ESA, EUMETSAT, published in Sentinel Online		
Accepted by ESA	S. Dransfeld, ESA TO		
Filename	OMPC.ACR.DQR.03.04-2024 - i1r0 - OLCI DQR April 2024.docx		

Changes Log

Version	Date	Changes
1.0	13/05/2024	First version

List of Changes

Version	Section	Answers to RID	Changes

Table of content

List of Figures

List of Tables

1 Processing Baseline Version

1.1 Sentinel3-A

IPF	IPF / Processing Baseline version	Date of deployment
OL1	06.17 / OL__L1_.003.03.02 (with uncertainties activated)	27/02/2024
OL2 LAND	06.19 / OL__L2L.002.12.00	28/02/2024
SY2	06.28 / SYN_L2_.002.20.00	28/02/2024
SY2_VGS	06.13 / SYN_L2V.002.09.01	25/07/2023
SY2_AOD	01.08 / AOD_NTC.002.08.01	25/07/2023

1.2 Sentinel3-B

IPF	IPF / Processing Baseline version	Date of deployment
OL1	06.17 / OL__L1_.003.03.02 (with uncertainties activated)	27/02/2024
OL2 Land	06.18 / OL__L2L.002.12.00	27/02/2024
SY2	06.25 / SYN_L2_.002.20.00	27/02/2024
SY2_VGS	06.13 / SYN_L2V.002.09.01	18/07/2023
SY2_AOD	01.08 / AOD_NTC.002.08.01	18/07/2023

2 Instrument monitoring

2.1 CCD temperatures

2.1.1 OLCI-A

The long-term monitoring of the CCD temperatures is based on Radiometric Calibration Annotations (see Figure 1). Variations are very small (0.09 C peak-to-peak) and no trend can be identified. Data from current reporting period (rightmost data points) do not show any specificity.

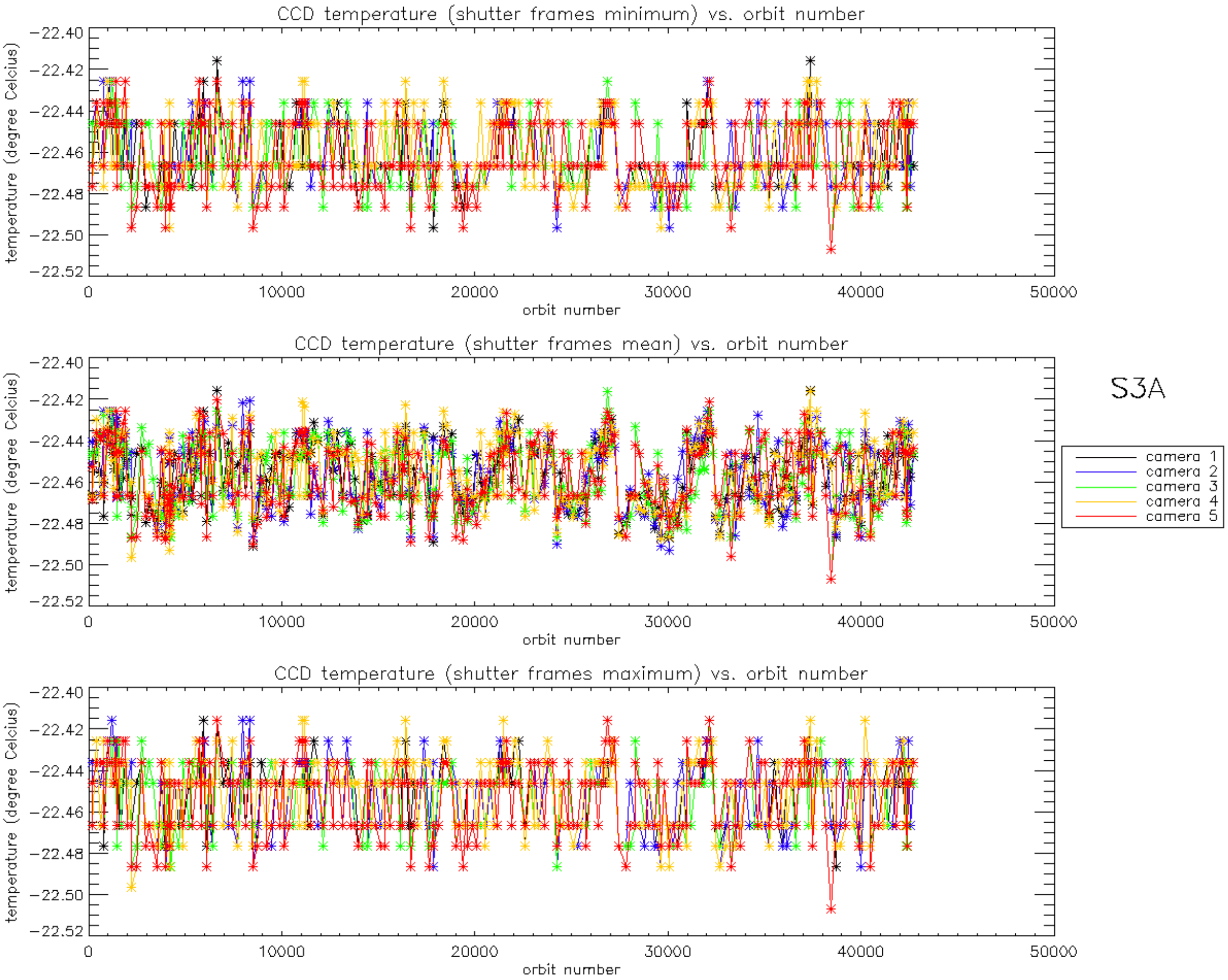

Figure 1: long term monitoring of OLCI-A CCD temperatures using minimum value (top), time averaged values (middle), and maximum value (bottom) provided in the annotations of the Radiometric Calibration Level 1 products, for the shutter frames, all radiometric calibrations so far except the first one (absolute orbit 183) for which the instrument was not yet thermally stable.

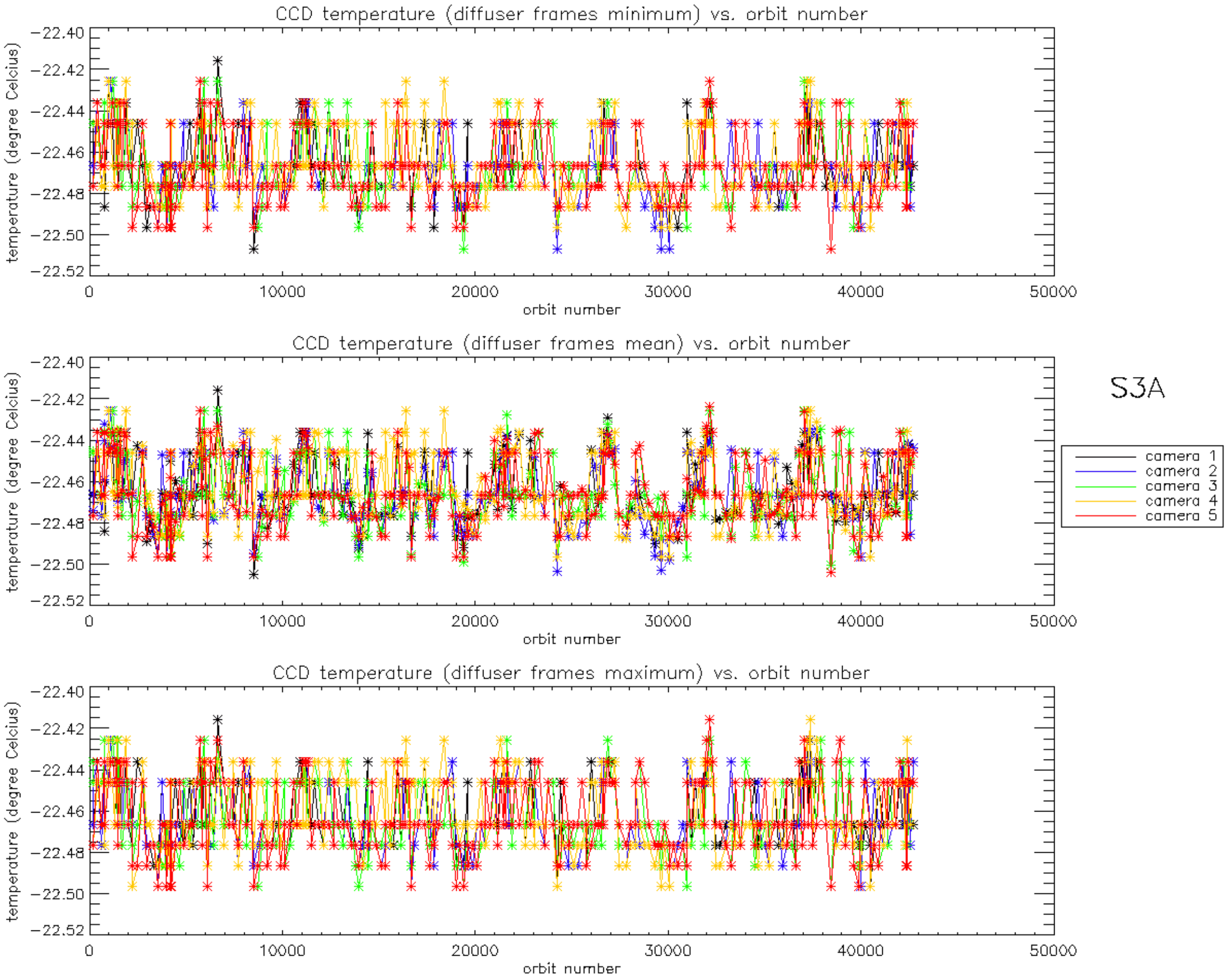

Figure 2: Same as Figure 1 for diffuser frames.

2.1.2 OLCI-B

As for OLCI-A, the variations of CCD temperature are very small (0.08 C peak-to-peak) and no trend can be identified. Data from current reporting period (rightmost data points) do not show any specificity.

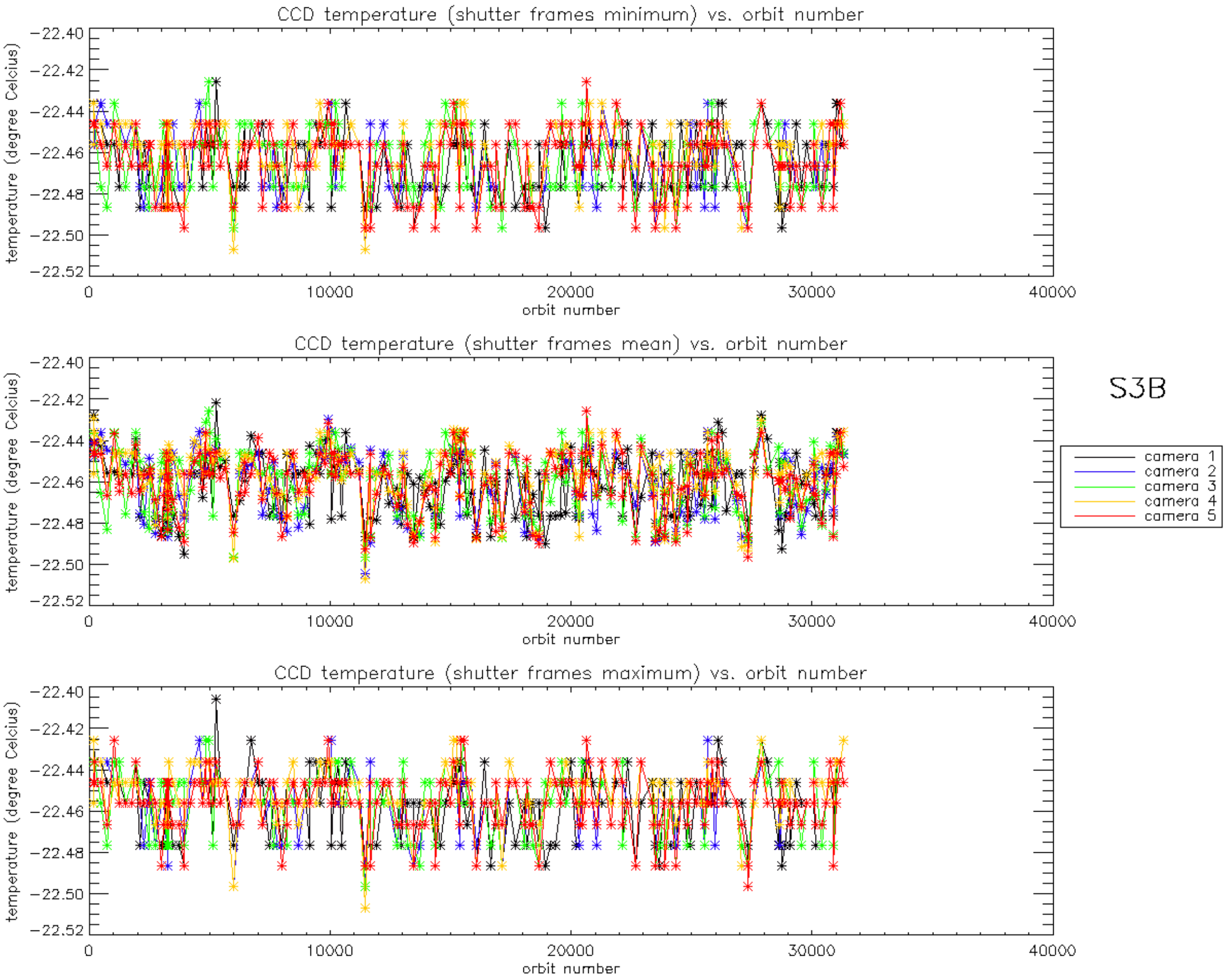

Figure 3: long term monitoring of OLCI-B CCD temperatures using minimum value (top), time averaged values (middle), and maximum value (bottom) provided in the annotations of the Radiometric Calibration Level 1 products, for the Shutter frames, all radiometric calibrations so far except the first one (absolute orbit 167) for which the instrument was not yet thermally stable.

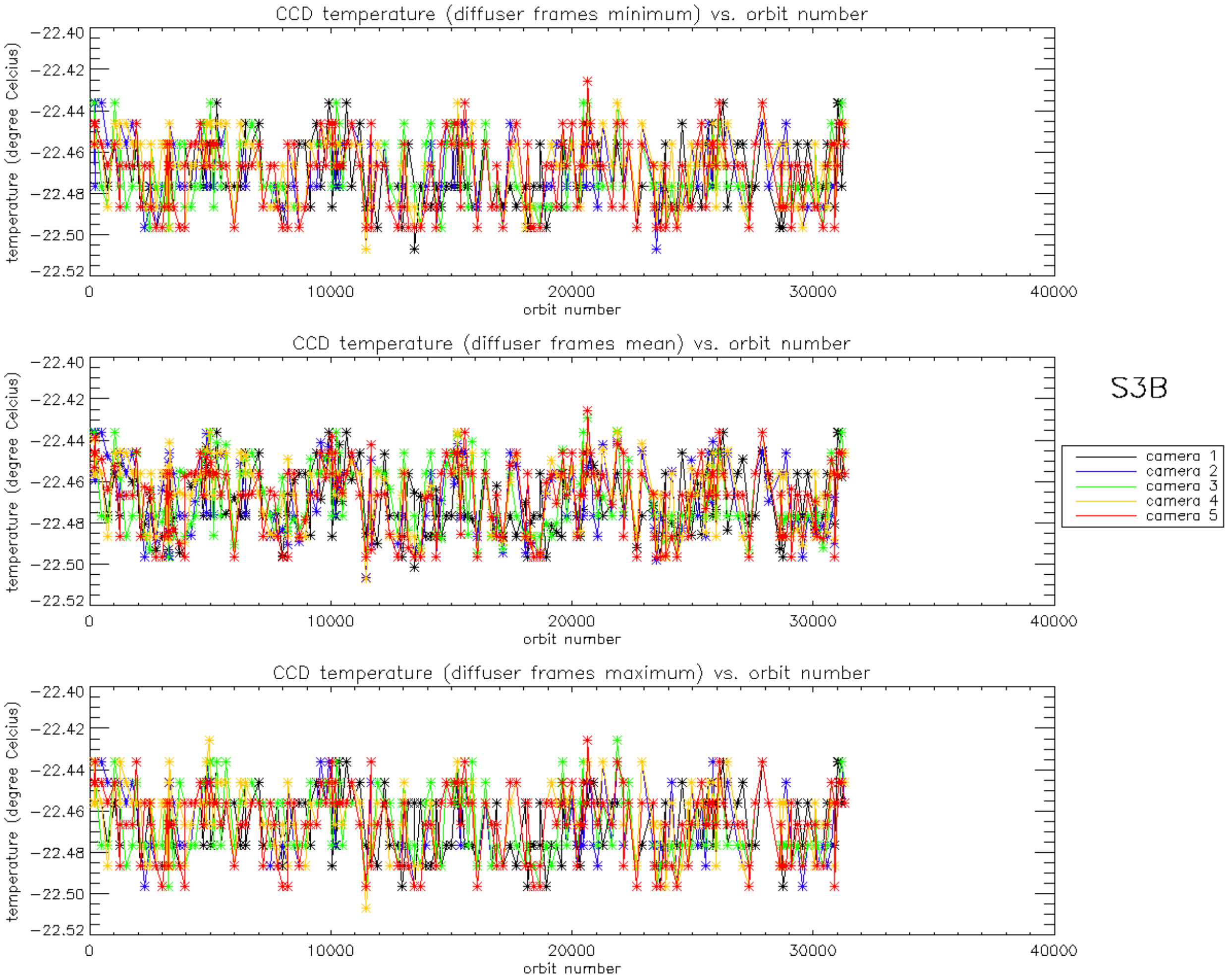

Figure 4: same as Figure 3 for diffuser frames.

2.2 Radiometric Calibration

For OLCI-A, five Radiometric Calibration sequences have been acquired during the reported period:

- S01 sequence (diffuser 1) on 03/04/2024 10:54 to 10:56 (absolute orbit 42331)
- S01 sequence (diffuser 1) on 08/04/2024 07:02 to 07:04 (absolute orbit 42400)
- S01 sequence (diffuser 1) on 12/04/2024 20:26 to 20:27 (absolute orbit 42465)
- S01 sequence (diffuser 1) on 20/04/2024 05:08 to 05:10 (absolute orbit 42570)
- S01 sequence (diffuser 1) on 30/04/2024 02:27 to 02:29 (absolute orbit 42711)

For OLCI-B, four Radiometric Calibration sequences have been acquired during the reported period:

- S01 sequence (diffuser 1) on 07/04/2024 10:11 to 10:13 (absolute orbit 30994)
- S01 sequence (diffuser 1) on 11/04/2024 18:32 to 18:34 (absolute orbit 31056)
- S01 sequence (diffuser 1) on 19/04/2024 04:56 to 04:57 (absolute orbit 31162)
- S01 sequence (diffuser 1) on 28/04/2024 17:49 to 17:51 (absolute orbit 31298)

The acquired Sun azimuth angles are presented on Figure 5 for OLCI-A and Figure 6 for OLCI-B, on top of the nominal values without Yaw Manoeuvre (i.e. with nominal Yaw Steering control of the satellite).

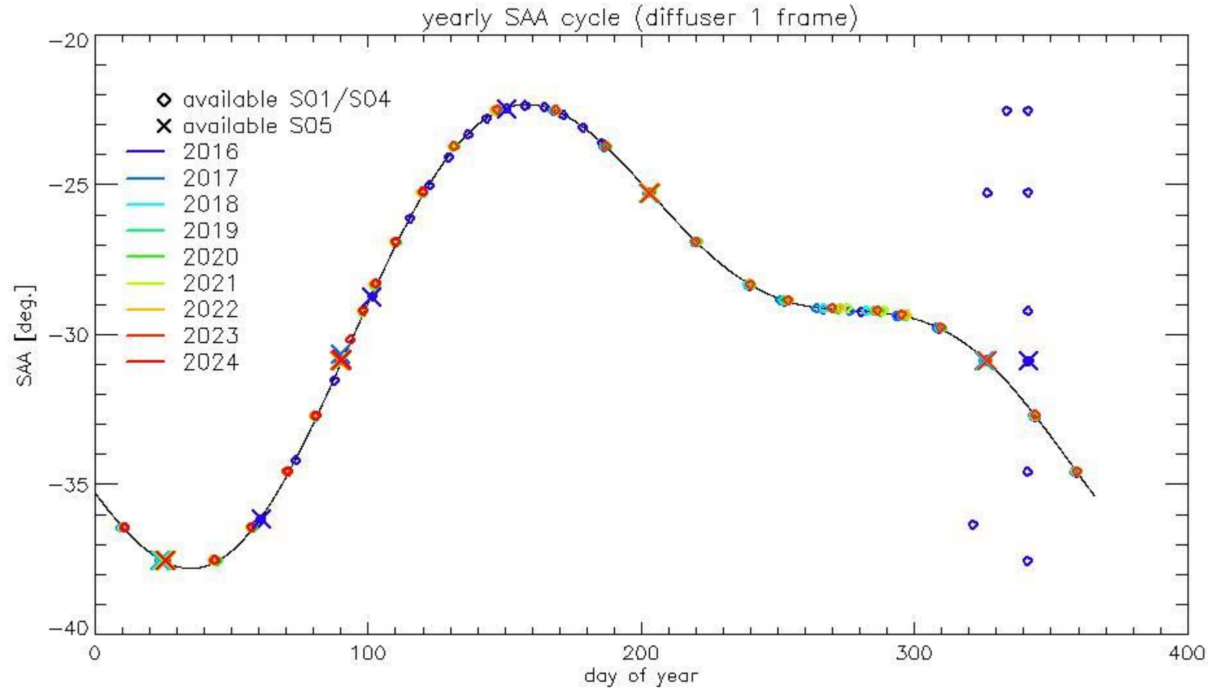

Figure 5: Sun azimuth angles during acquired OLCI-A Radiometric Calibrations (diffuser frame) on top of nominal yearly cycle (black curve). Diffuser 1 with diamonds, diffuser 2 with crosses. Different colours correspond to different years of acquisition (see the legend inside the figure).

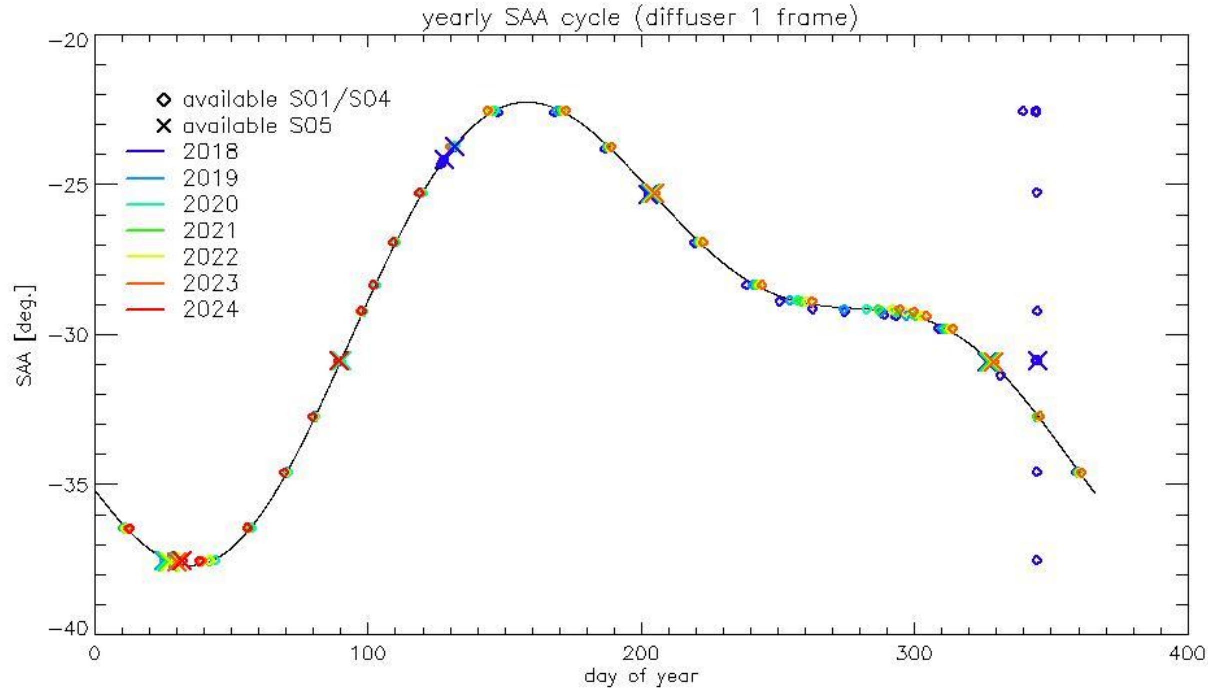

Figure 6: same as Figure 5 for OLCI-B.

Sun Zenith Angles as a function of Sun Azimuth Angles are presented in Figure 7 for OLCI-A and Figure 8 for OLCI-B.

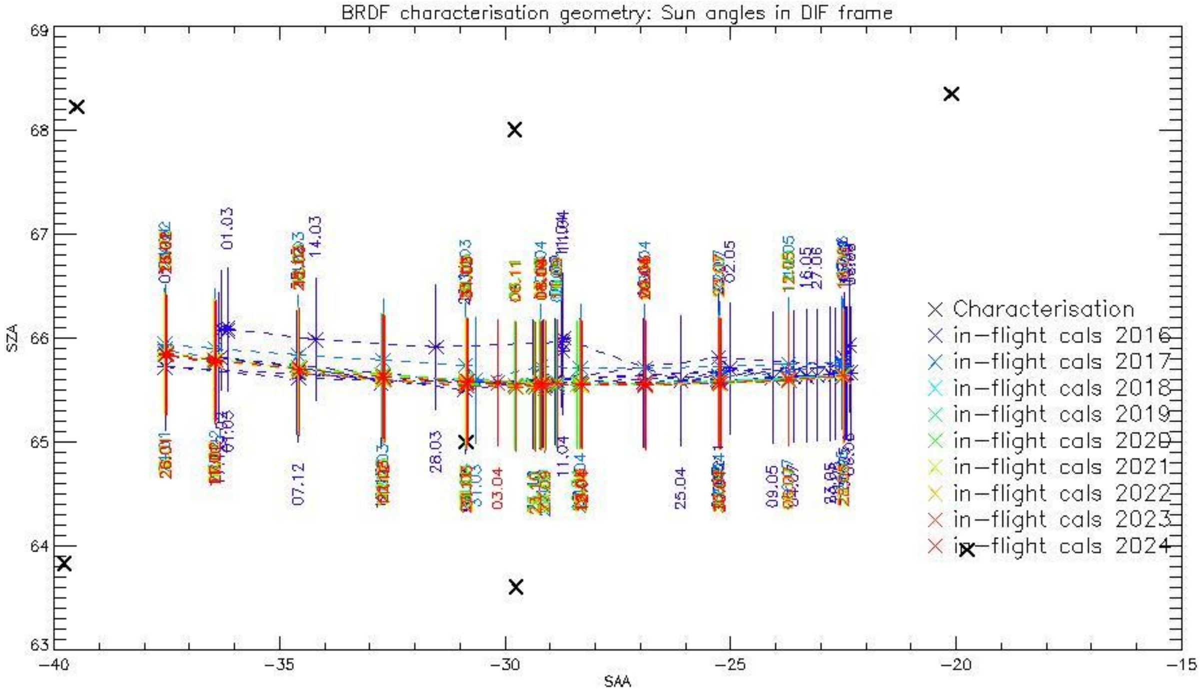

Figure 7: OLCI-A Sun geometry during radiometric Calibrations on top of characterization ones (diffuser frame)

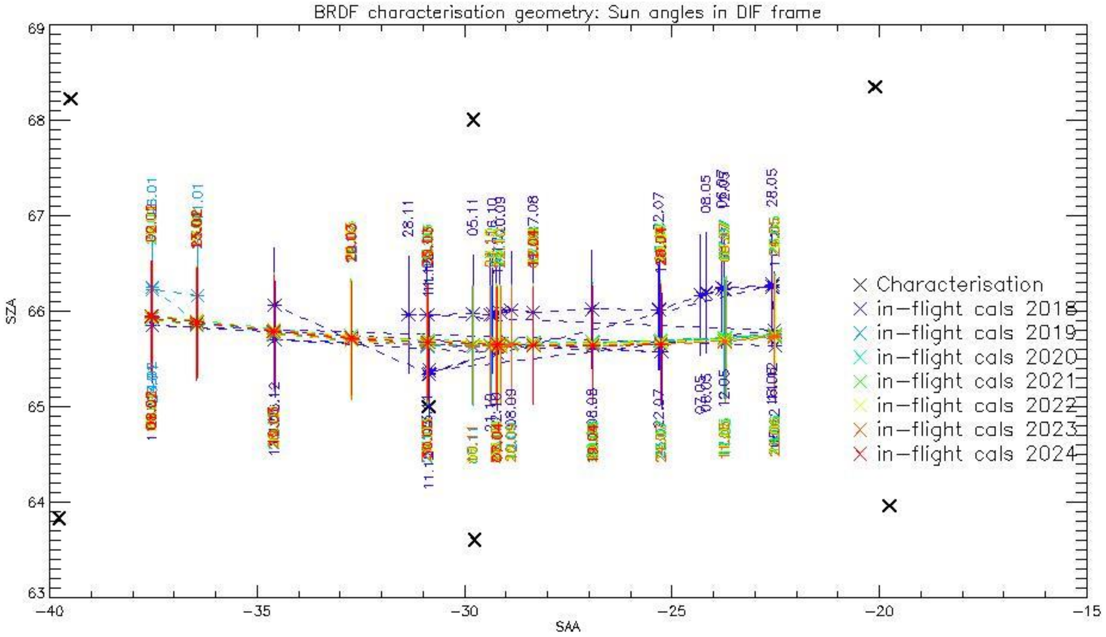

Figure 8: same as Figure 7 for OLCI-B

2.2.1 Dark Offsets [OLCI-L1B-CV-230]

Note about the High Energy Particles:

The filtering of High Energy Particle (HEP) events from radiometric calibration data has been implemented (for shutter frames only) in a post processor, allowing generating Dark Offset and Dark Current tables computed on filtered data. The post-processor starts from IPF intermediate data (corrected counts), applies the HEP detection and filtering and finally computes the Dark Offset and Dark Current tables the same way as IPF. An example of the impact of HEP filtering is given in Figure 9.

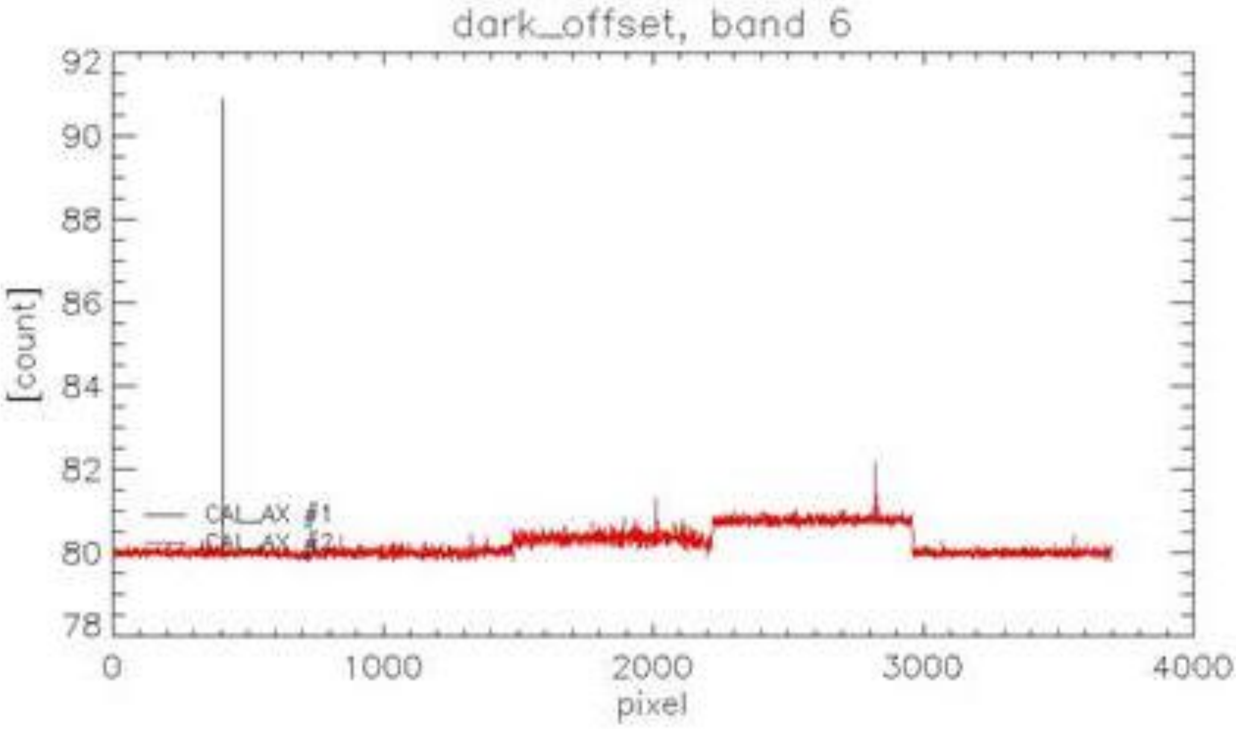

Figure 9: Dark Offset table for band Oa06 with (red) and without (black) HEP filtering (Radiometric Calibration of 22 July 2017). The strong HEP event near pixel 400 has been detected and removed by the HEP filtering.

All results presented below in this section have been obtained using the HEP filtered Dark Offset and Dark Current tables.

2.2.1.2 OLCI-A

Dark offsets

Dark offsets are continuously affected by the global offset induced by the Periodic Noise on the OCL (Offset Control Loop) convergence. Current reporting period calibrations are affected the same way as others. The amplitude of the shift varies with band and camera from virtually nothing (e.g. camera 2, band 0a1) to up to 5 counts (Oa21, camera 3). The Periodic Noise itself comes on top of the global shift with its known signature: high frequency oscillations with a rapid damp. This effect remains more or less stable with time in terms of amplitude, frequency and decay length, but its phase varies with time, introducing the global offset mentioned above.

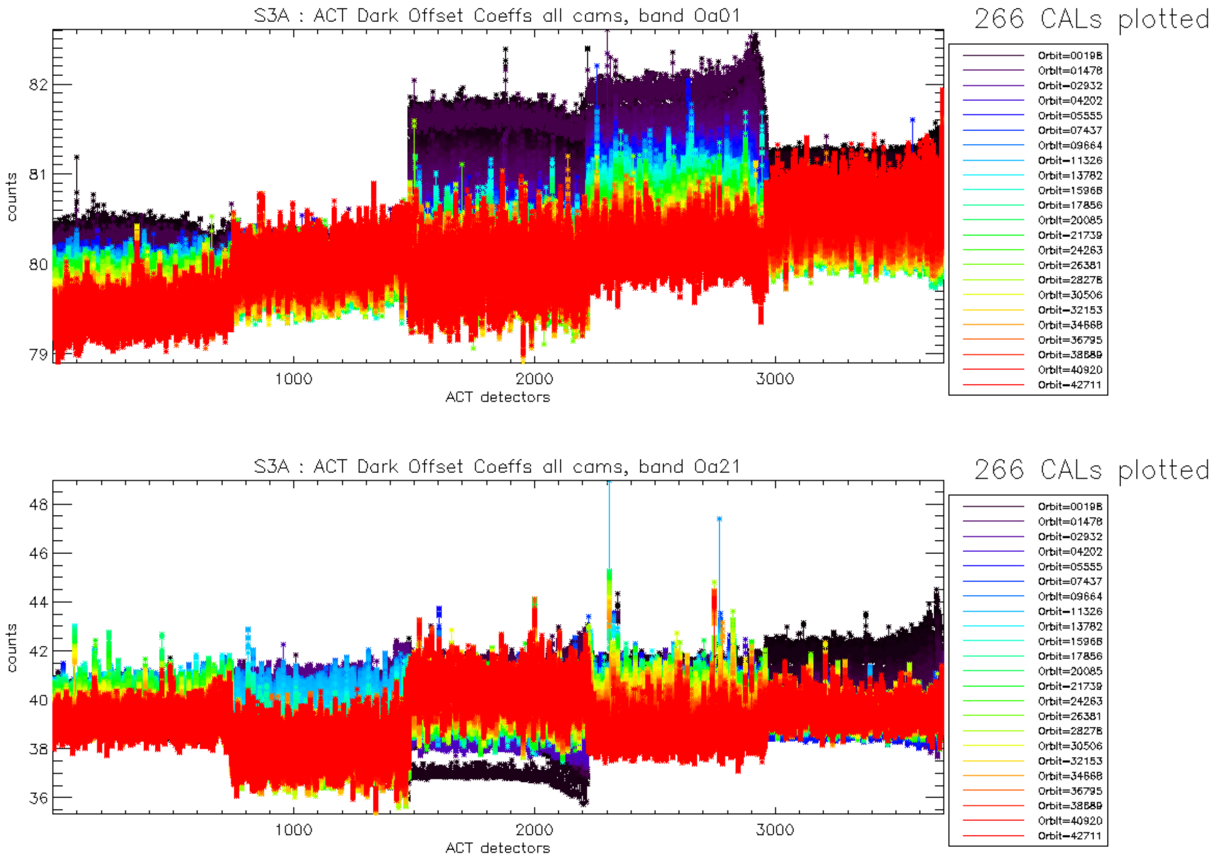

Figure 10: OLCI-A Dark Offset for band Oa1 (top) and Oa21 (bottom), all radiometric calibrations so far except the first one (orbit 183) for which the instrument was not thermally stable yet.

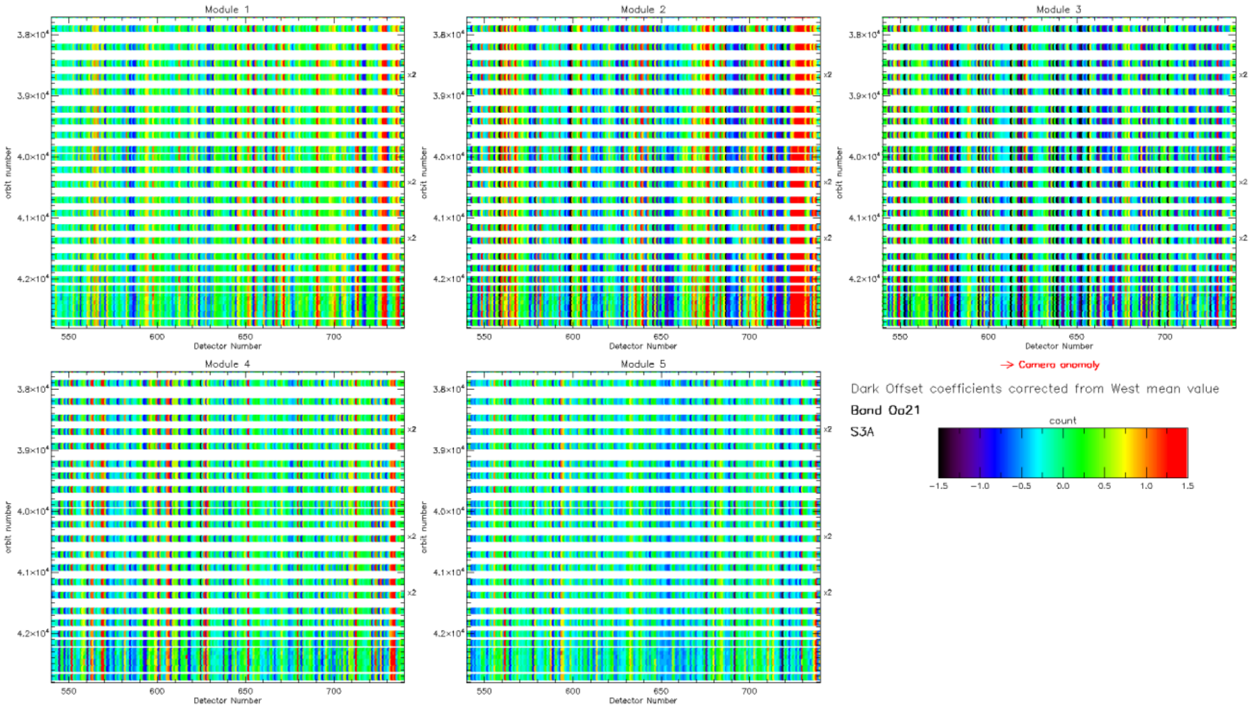

Figure 11: map of OLCI-A periodic noise for the 5 cameras, for band Oa21. X-axis is detector number (East part, from 540 to 740, where the periodic noise occurs), Y-axis is the orbit number. Y-axis range is focused on the most recent 5000 orbits. The counts have been corrected from the West detectors mean value (not affected by periodic noise) in order to remove mean level gaps and consequently to have a better visualisation of the long term evolution of the periodic noise structure. At the beginning of the mission the periodic noise for band Oa21 had strong amplitude in camera 2, 3 and 5 compared to camera 1 and 4. However PN evolved through the mission and these discrepancies between cameras have been reduced. At the time of this Cyclic Report Camera 2 still shows a slightly higher PN than other cameras.

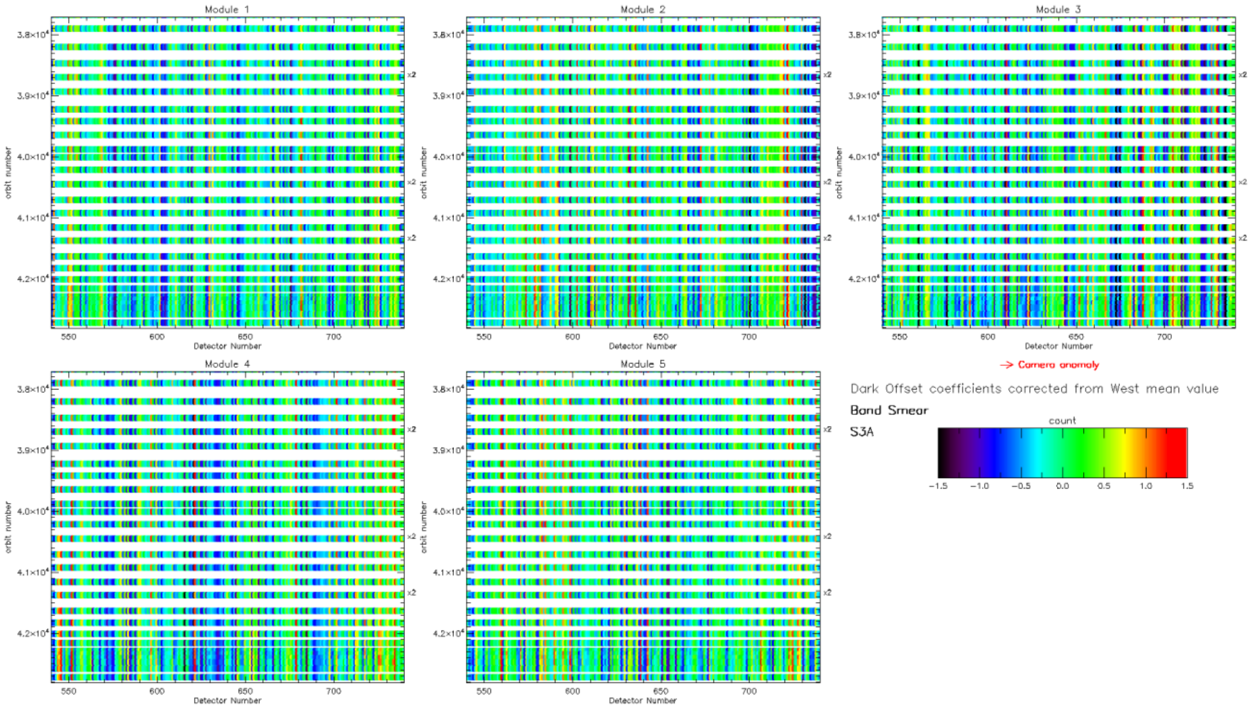

Figure 12: same as Figure 11 for smear band.

Figure 11 and Figure 12 show the so-called 'map of periodic noise' in the 5 cameras, for respectively band 21 and smear band. These maps have been computed from the dark offsets after removal of the mean level of the WEST detectors (not impacted by PN) in order to remove mean level gaps from one CAL to the other and consequently to highlight the shape of the PN. Maps are focused on the last 200 EAST detectors where PN occurs and on a time range covering only the last 5000 orbits in order to better visualize the CALs of the current reporting period.

Figure 11 and Figure 12 show that at this stage of the mission the PN is very stable in all cameras. There is no special behaviour noticed during the reporting period.

Dark Currents

Dark Currents (Figure 13) are not affected by the global offset of the Dark Offsets, thanks to the clamping to the average blind pixels value. However, the oscillations of Periodic Noise remain visible. There is no significant evolution of this parameter during the current reporting period except the small regular increase (almost linear), for all detectors, since the beginning of the mission (see Figure 14).

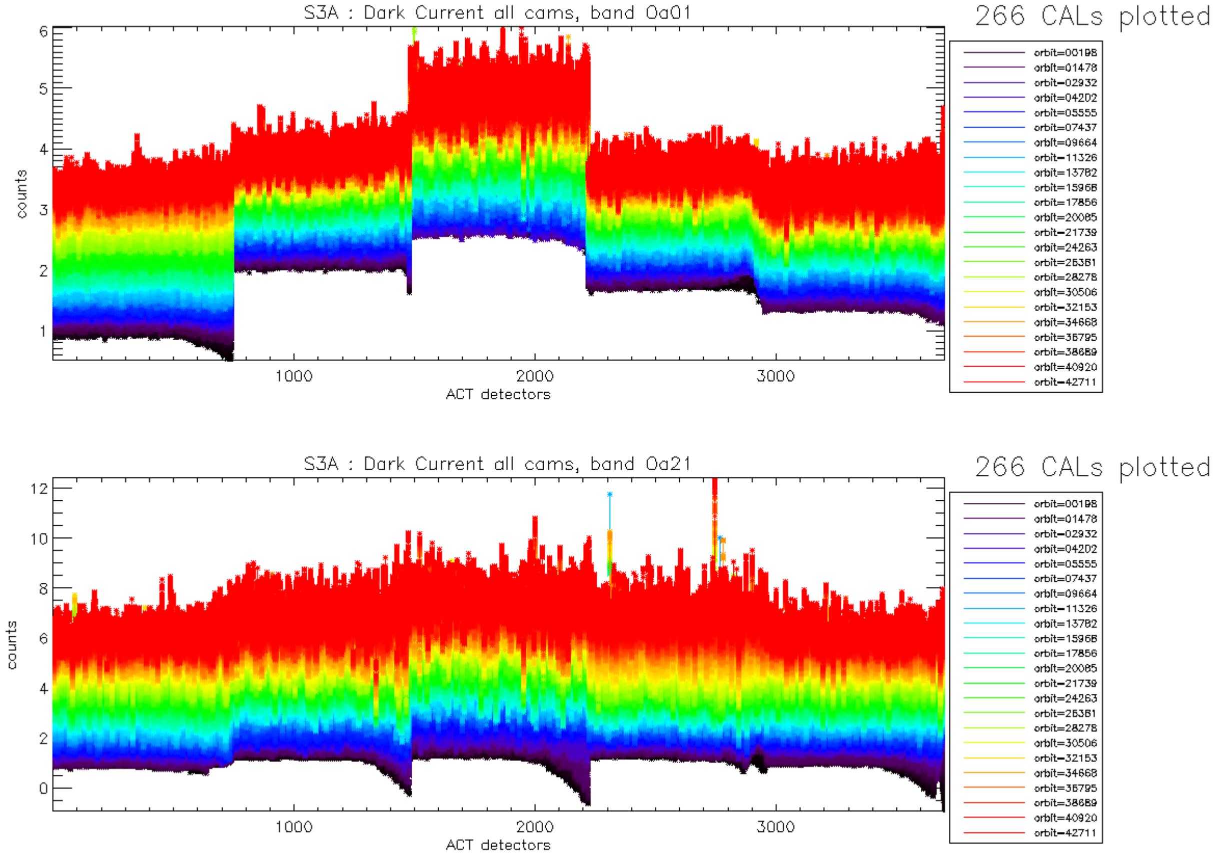

Figure 13: OLCI-A Dark Current for band Oa1 (top) and Oa21 (bottom), all radiometric calibrations so far except the first one (orbit 183) for which the instrument was not thermally stable yet.

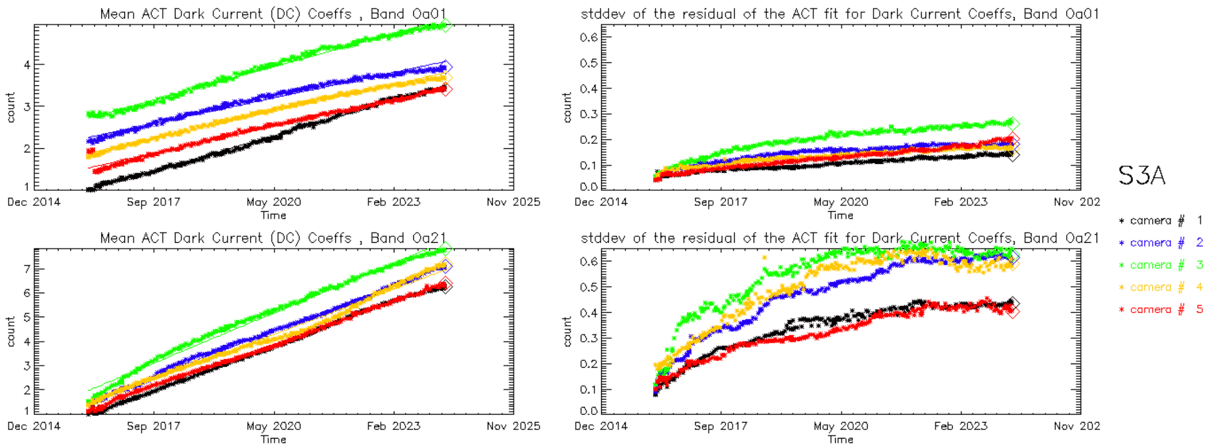

Figure 14: left column: ACT mean on 400 first detectors of OLCI-A Dark Current coefficients for spectral band Oa01 (top) and Oa21 (bottom). Right column: same as left column but for Standard deviation instead of mean. We see an increase of the DC level as a function of time especially for band Oa21.

A possible explanation of the regular increase of DC could be the increase of the number of hot pixels which is more important in Oa21 because this band is made of more CCD lines than band Oa01 and thus receives more cosmic rays impacts. It is known that cosmic rays degrade the structure of the CCD, generating more and more hot pixels at long term scales. Indeed, when computing the time slopes of the spatially averaged Dark Current as a function of band, i.e. the slopes of curves in left plots of Figure 14, one can see that Oa21 is by far the most affected, followed by the smear band (Figure 15, left); when plotting these slopes against total band width (in CCD rows, regardless of the number of micro-bands), the correlation between the slope values and the width becomes clear (Figure 15, right).

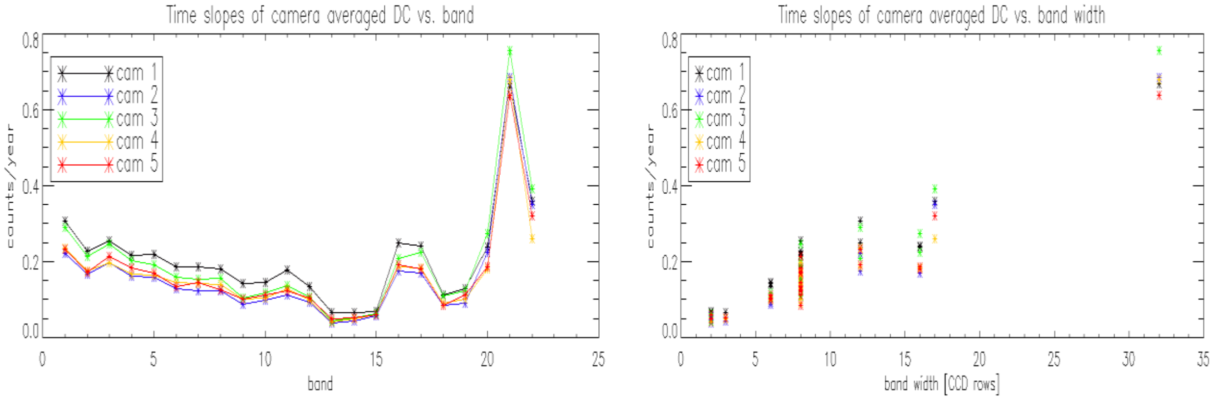

Figure 15: OLCI-A Dark current increase rates with time (in counts per year) vs. band (left) and vs. band width (right)

2.2.1.3 OLCI-B

Dark Offsets

Dark offsets for OLCI-B show a similar behaviour than for OLCI-A: mean level gaps between different orbits, induced by the presence of a pseudo periodic noise on the east edge of the cameras with a drifting phase.

Evolution of OLCI-B Dark Offset coefficients for band Oa01 and Oa21 are represented in Figure 16.

The periodic noise maps are shown for band Oa21 and smear band respectively in Figure 17 and Figure 18. As it happened for OLCI-A after a few thousands of orbits, the strong periodic noise phase and amplitude drift, present at the very beginning of the mission is now showing a clear stabilization.

Despite this overall stabilization, small evolutions are still noticeable in some bands/camera, like for example camera 1 in band Oa21 (upper left map in Figure 17) or in camera 1 band smear (upper left map in Figure 18).

Globally, OLCI-B PN is slightly less stabilized than OLCI-A PN.

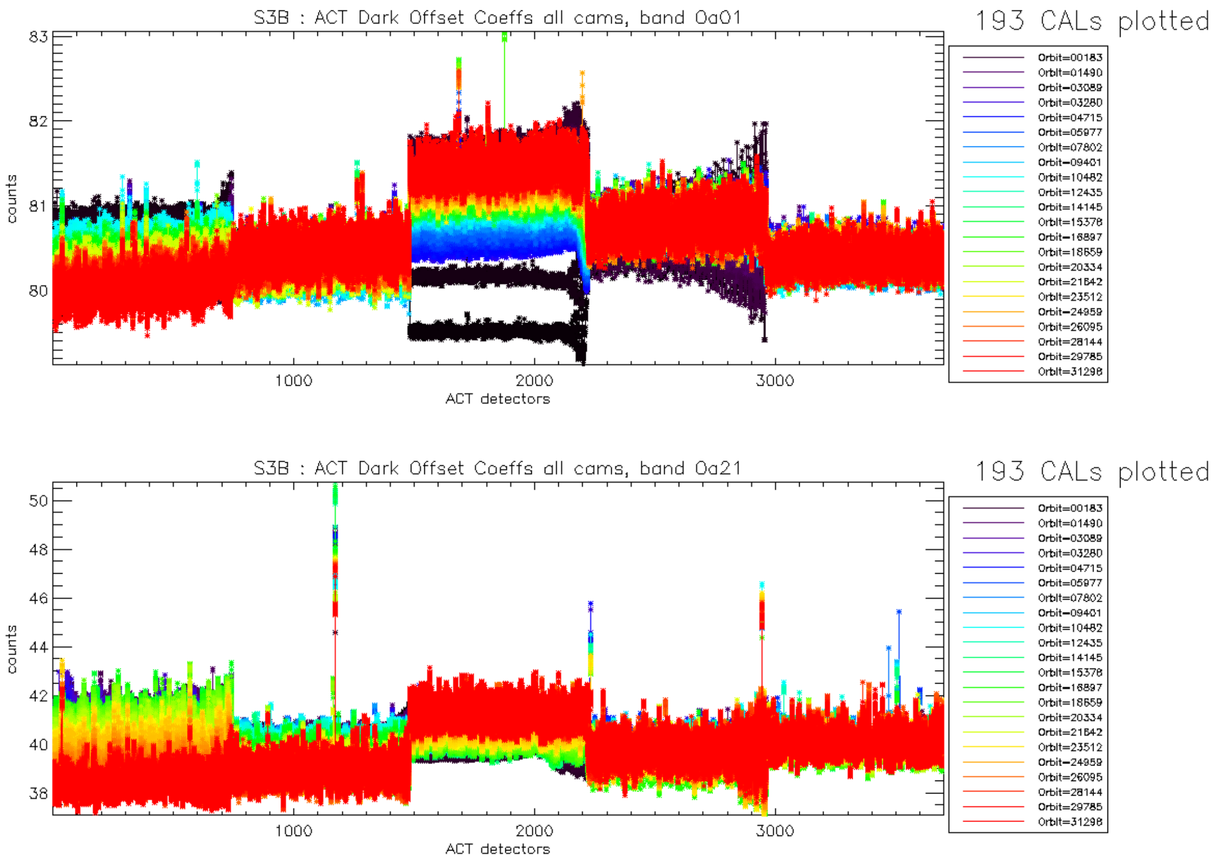

Figure 16: OLCI-B Dark Offset for band Oa1 (top) and Oa21 (bottom), all radiometric calibrations so far except the first one (orbit 167) for which the instrument was not thermally stable yet.

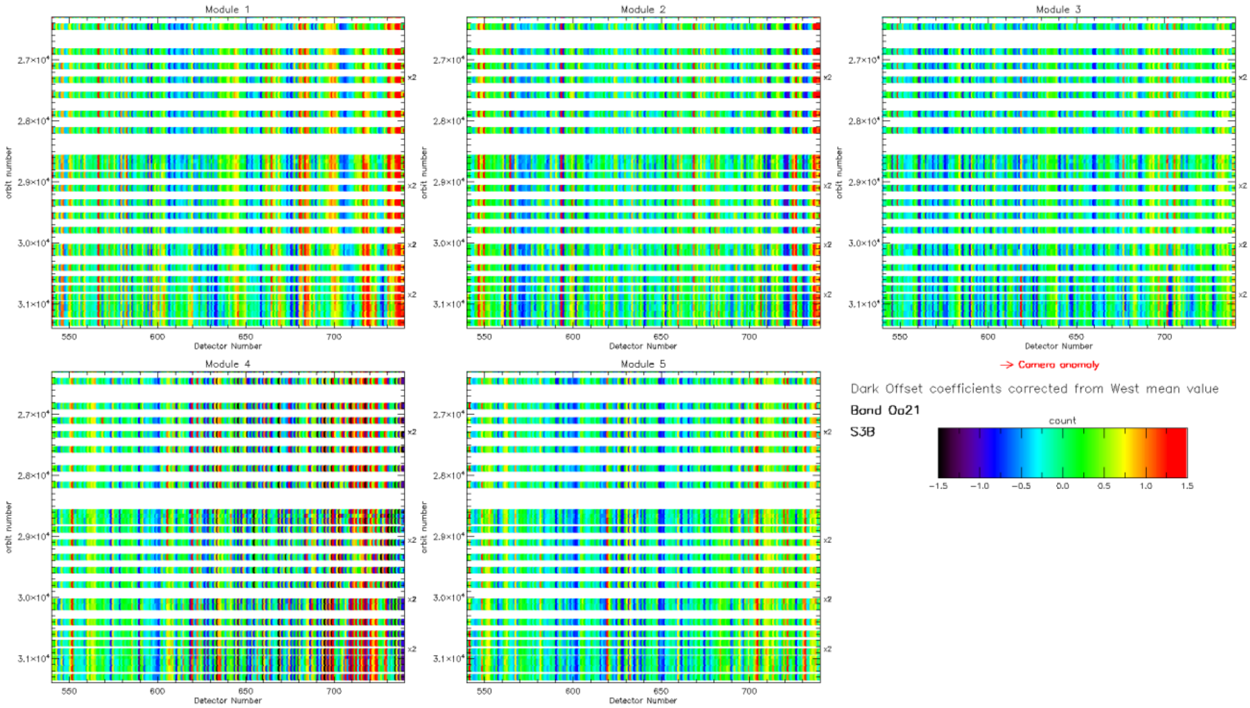

Figure 17: OLCI-B map of periodic noise for the 5 cameras, for band Oa21. X-axis is detector number (East part, from 540 to 740, where the periodic noise occurs), Y-axis is the orbit number. The counts have been corrected from the West detectors mean value (not affected by periodic noise) in order to remove mean level gaps and consequently to have a better visualization of the long term evolution of the periodic noise structure.

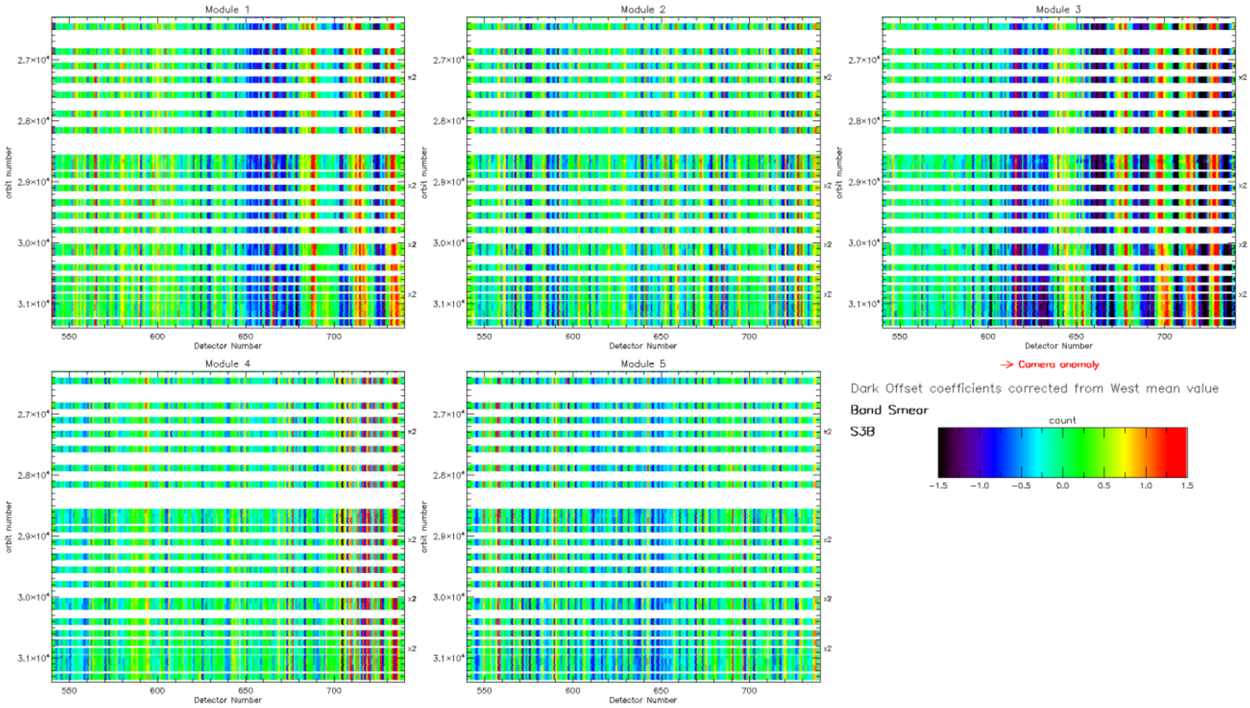

Figure 18: same as Figure 17 for smear band.

Dark Currents

As for OLCI-A there is no significant evolution of the Dark Current coefficients (Figure 19) during the current reporting period except the small regular increase (almost linear), for all detectors, since the beginning of the mission (see Figure 20) probably due to an increase of hot pixels (see Figure 21).

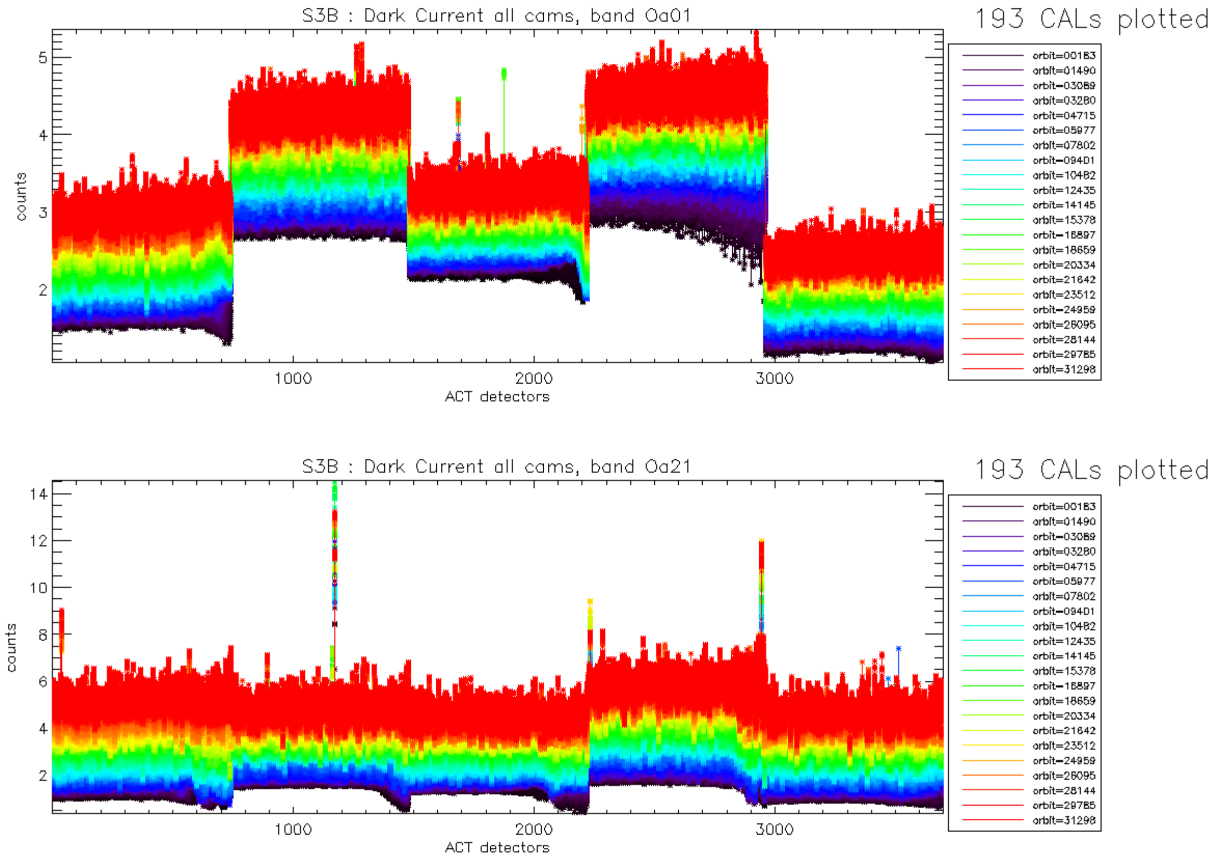

Figure 19: OLCI-B Dark Current for band Oa1 (top) and Oa21 (bottom), all radiometric calibrations so far except the first one (orbit 167) for which the instrument was not thermally stable yet.

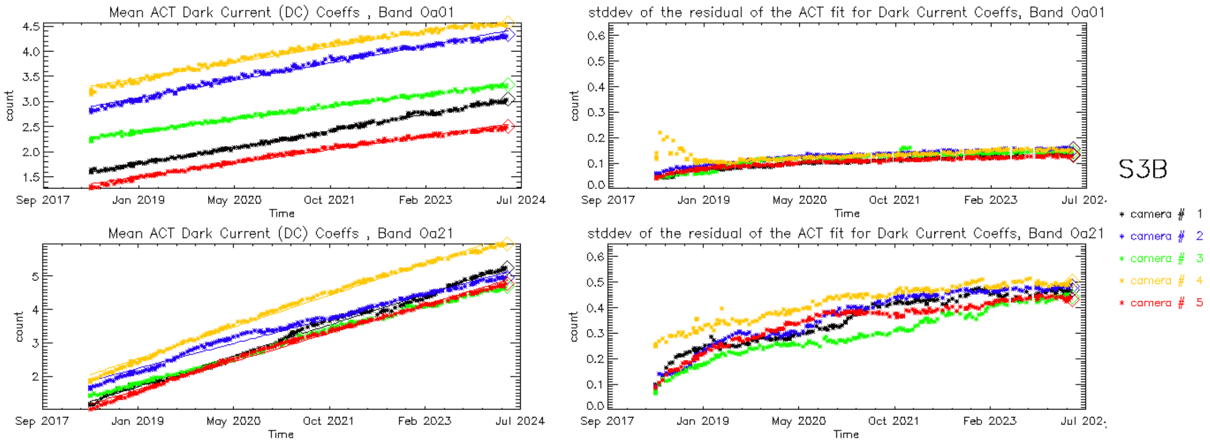

Figure 20: left column: ACT mean on 400 first detectors of OLCI-B Dark Current coefficients for spectral band Oa01 (top) and Oa21 (bottom). Right column: same as left column but for Standard deviation instead of mean. We see an increase of the DC level as a function of time especially for band Oa21.

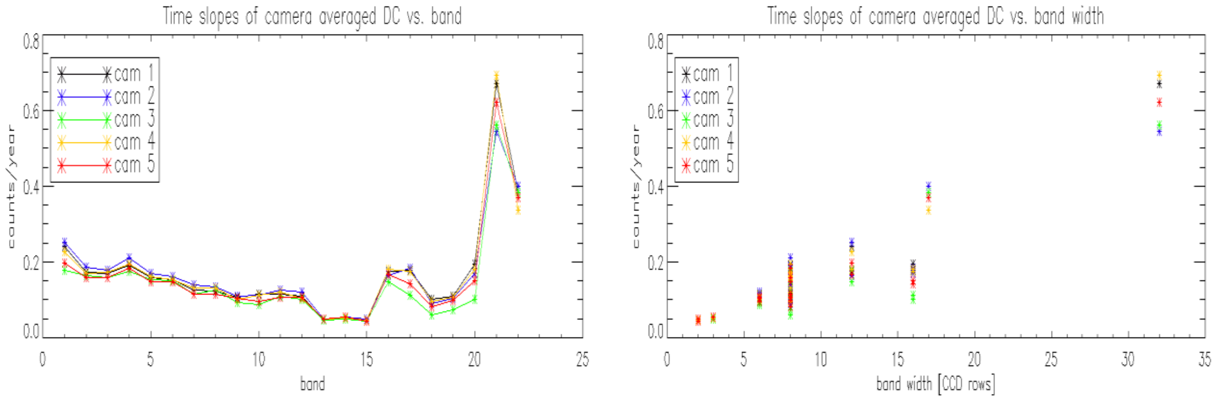

Figure 21: OLCI-B Dark Current increase rates with time (in counts per year) vs. band (left) and vs. band width (right)

2.2.3 Instrument response and degradation modelling [OLCI-L1B-CV-250]

2.2.3.1 Instrument response monitoring

2.2.3.1.1 OLCI-A

Figure 22 shows the gain coefficients of every pixel for two OLCI-A channels, Oa1 (400 nm) and Oa21 (1020 nm), highlighting the significant evolution of the instrument response since early mission.

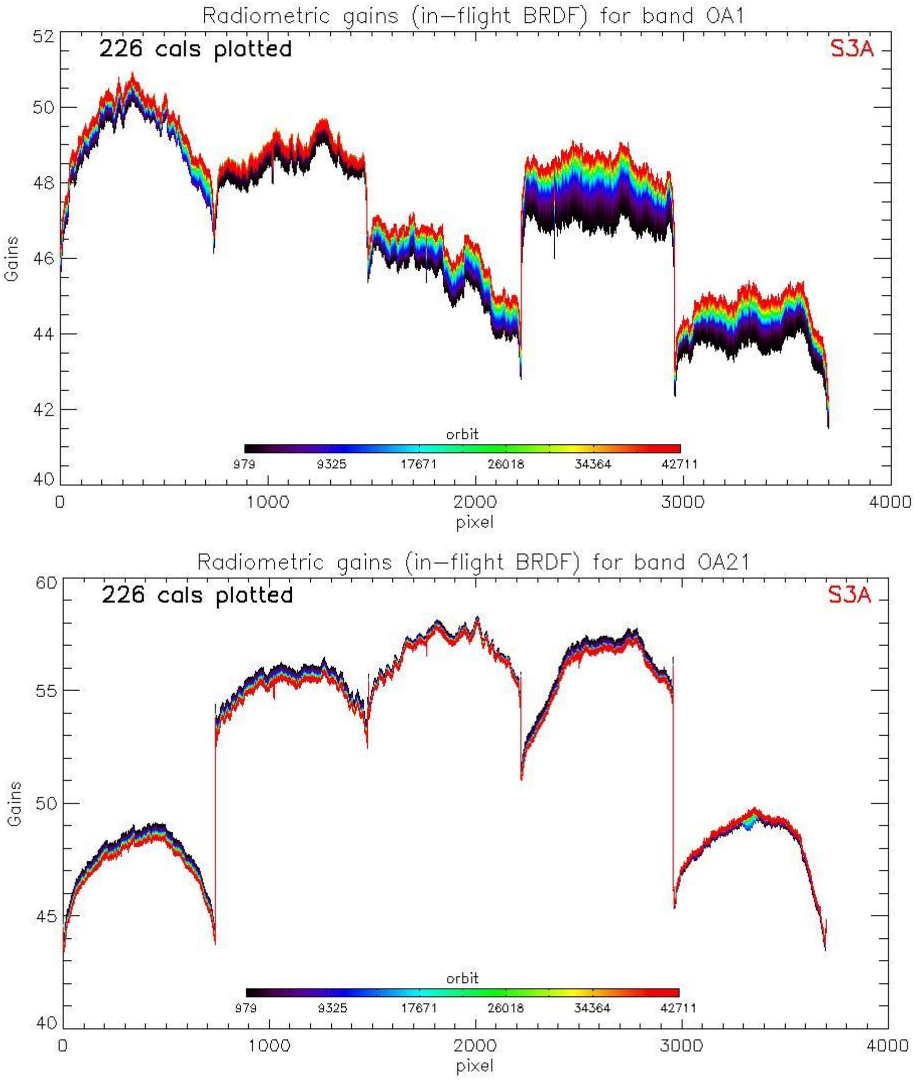

Figure 22: OLCI-A Gain Coefficients for band Oa1 (top) and Oa21 (bottom), derived using the in-flight BRDF model. The dataset is made of all diffuser 1 radiometric calibrations since orbit 979.

Figure 23 displays a summary of the time evolution of the cross-track average of the gains (in-flight BRDF, taking into account the diffuser ageing), for each module, relative to a given reference calibration (the 25/04/2016, change of OLCI channel settings). It shows that, if a significant evolution occurred during the early mission, the trends tend in general to stabilize, with some exceptions (e.g. band 1 of camera 1 and 4, bands 2 & 3 of camera 5).

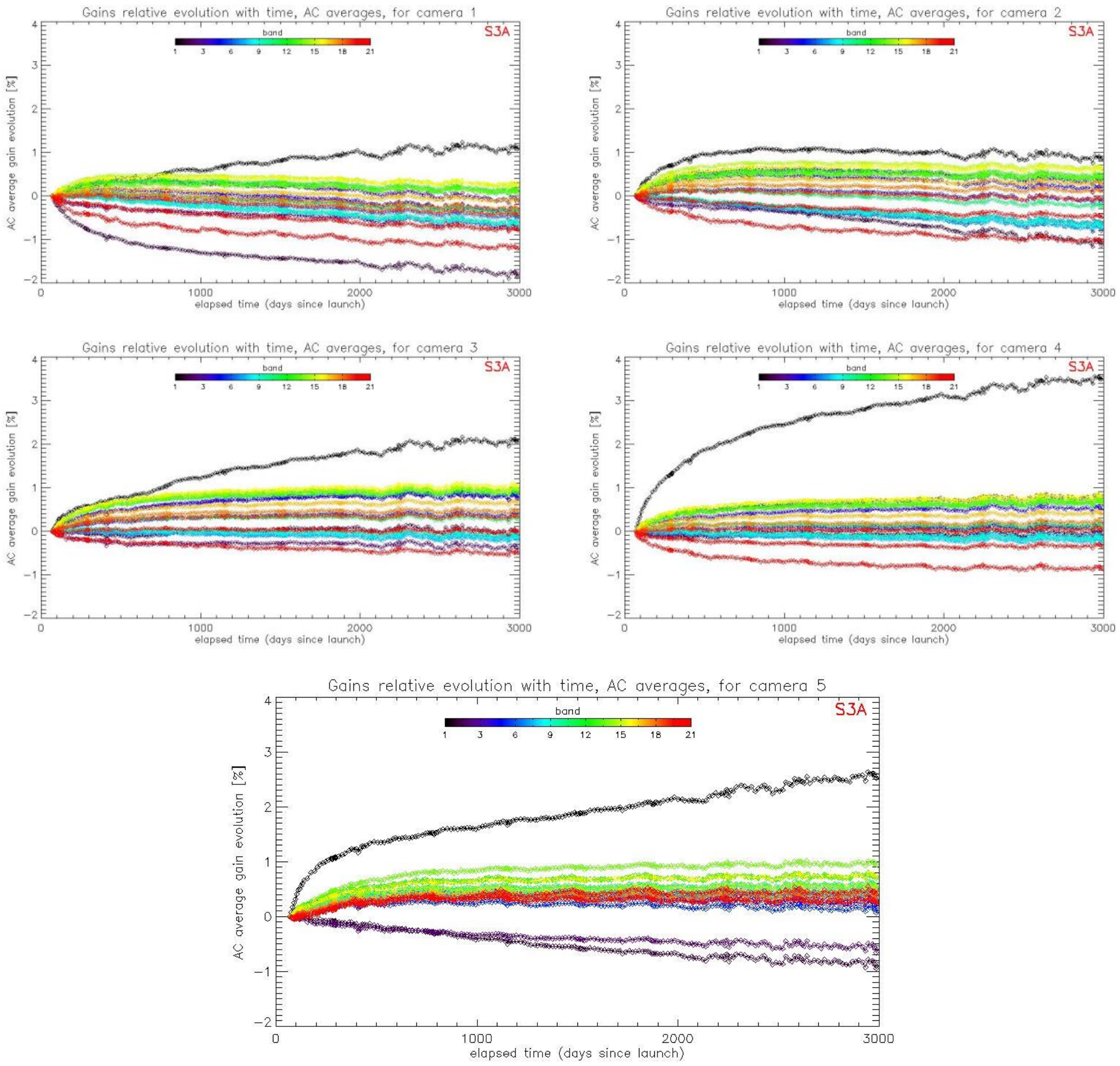

Gains relative evolution with time, AC averages, for camera 1

Gains relative evolution with time, AC averages, for camera 2

Gains relative evolution with time, AC averages, for camera 3

Gains relative evolution with time, AC averages, for camera 4

Gains relative evolution with time, AC averages, for camera 5

Figure 23: camera averaged gain relative evolution with respect to calibration of 25/04/2016 (change of OLCI channel settings), as a function of elapsed time since the beginning of the mission; one curve for each band (see colour code on plots), one plot for each module. The diffuser ageing is taken into account.

2.2.3.1.2 OLCI-B

Figure 24 shows the gain coefficients of every pixel for two OLCI-B channels, Oa1 (400 nm) and Oa21 (1020 nm), highlighting the significant evolution of the instrument response since early mission.

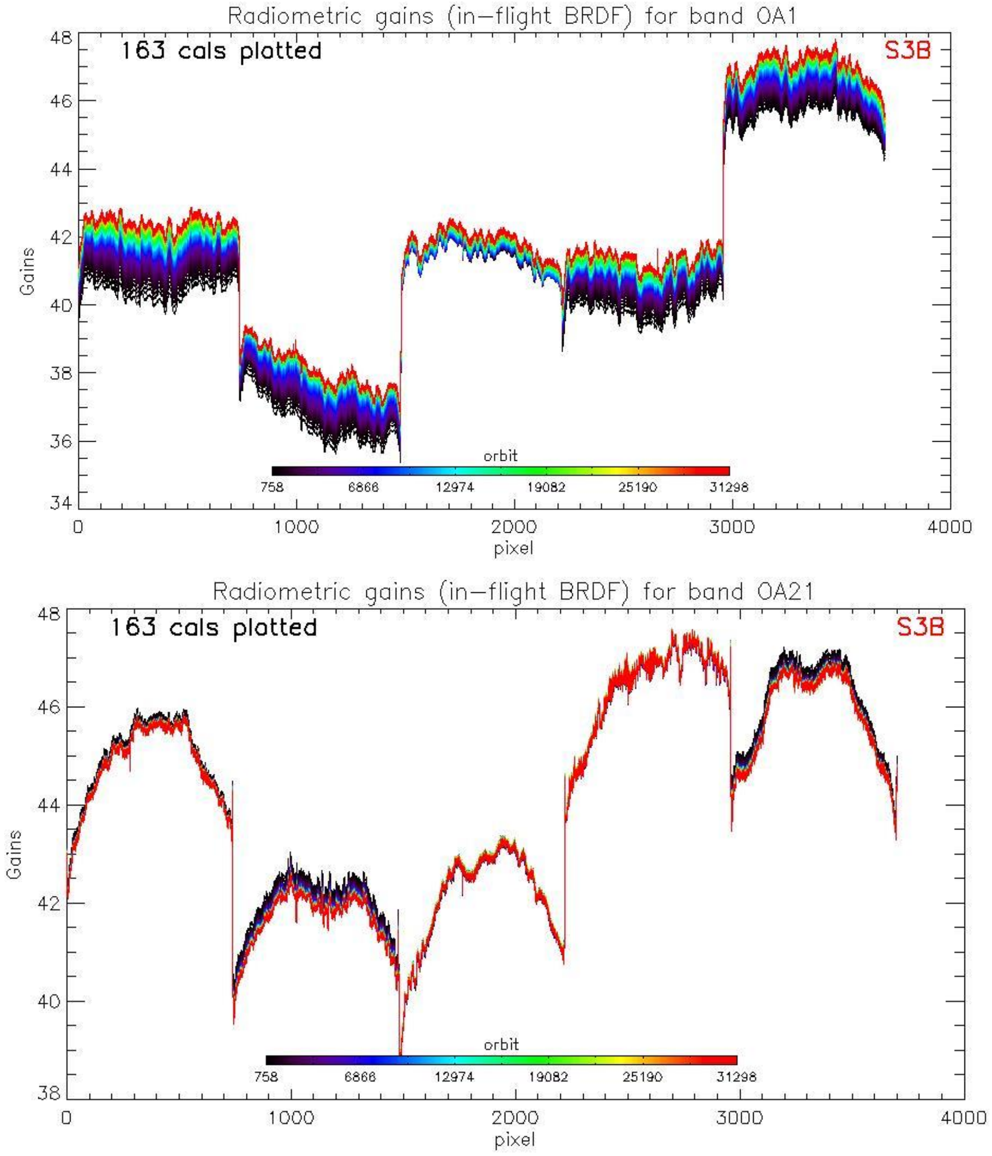

Figure 24: OLCI-B Gain Coefficients for band Oa1 (top) and Oa21 (bottom), derived using the in-flight BRDF model. The dataset is made of all diffuser 1 radiometric calibrations since orbit 758.

Figure 25 displays a summary of the time evolution of the cross-track average of the gains (in-flight BRDF, taking into account diffuser ageing), for each module, relative to a given reference calibration (first calibration after channel programming change: 18/06/2018). It shows that, if a significant evolution occurred during the early mission, the trends tend to stabilize. The large amount of points near elapsed time = 220 days is due to the yaw manoeuvre campaign. The slight discontinuity near “day 920 since launch” is due to the upgrade of the Ageing model.

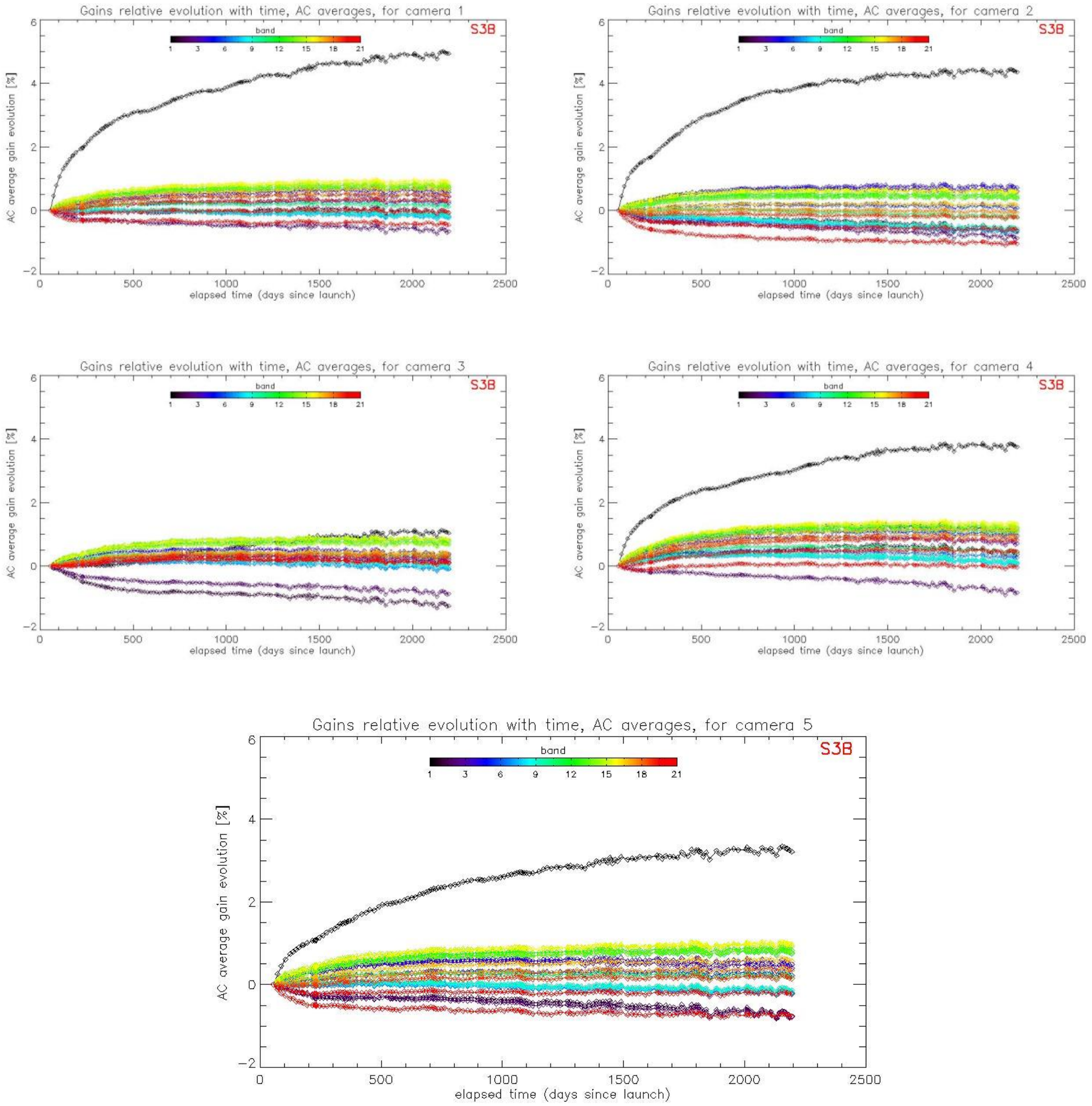

Figure 25: OLCI-B camera averaged gain relative evolution with respect to first calibration after channel programming change (18/06/2018), as a function of elapsed time since the beginning of the mission; one curve for each band (see colour code on plots), one plot for each module. The diffuser ageing is taken into account.

2.2.3.2 Instrument evolution modelling

2.2.3.2.1 OLCI-A

A new OLCI-A Radiometric Gain Model has been put in operations at PDGS the 27/02/2024 (Processing Baseline 3.27). This model has been derived on the basis of an extended (compared to the previous model) Radiometric Calibration dataset, going from 11/04/2016 to 26/12/2023. It includes the correction of the diffuser ageing for the six bluest bands (Oa1 to Oa6) for which it is clearly measurable. The model performance over the complete dataset (including the 11 calibrations in extrapolation over about 4 months) remains better than about 0.08% for all bands at the exception of a few spikes after orbit 30000 reaching up to 0.15% for Oa01. The previous model, trained on a Radiometric Dataset limited to 28/05/2023, shows a slightly more pronounced drift of the model with respect to most recent data (Figure 27), that motivated the change. Comparison of the two figures shows a slight improvement brought by the updated model over the most recent period over which the previous model was used in extrapolation, however the impact is low, showing that the models are now quite stable. Performance shown on Figure 26 adopts, as for OLCI-B, the multiple model approach, i.e. different models (two for OLCI-A since PB 3.23, three for OLCI-B since PB 1.57) are used to cover the whole mission (red dashed line on Figure 26), each model being fitted on a partial dataset (green dashed line on Figure 26) whose coverage is optimized to provide best performance.

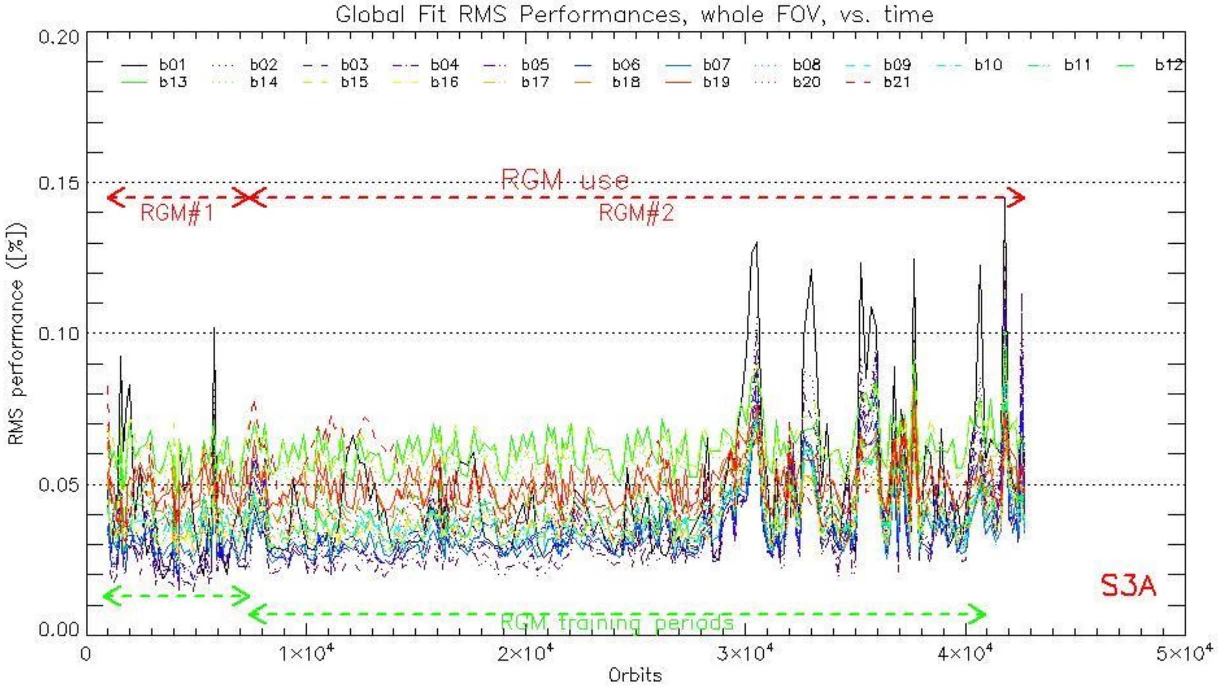

Figure 26: RMS performance of the OLCI-A Gain Model of the current processing baseline as a function of orbit.

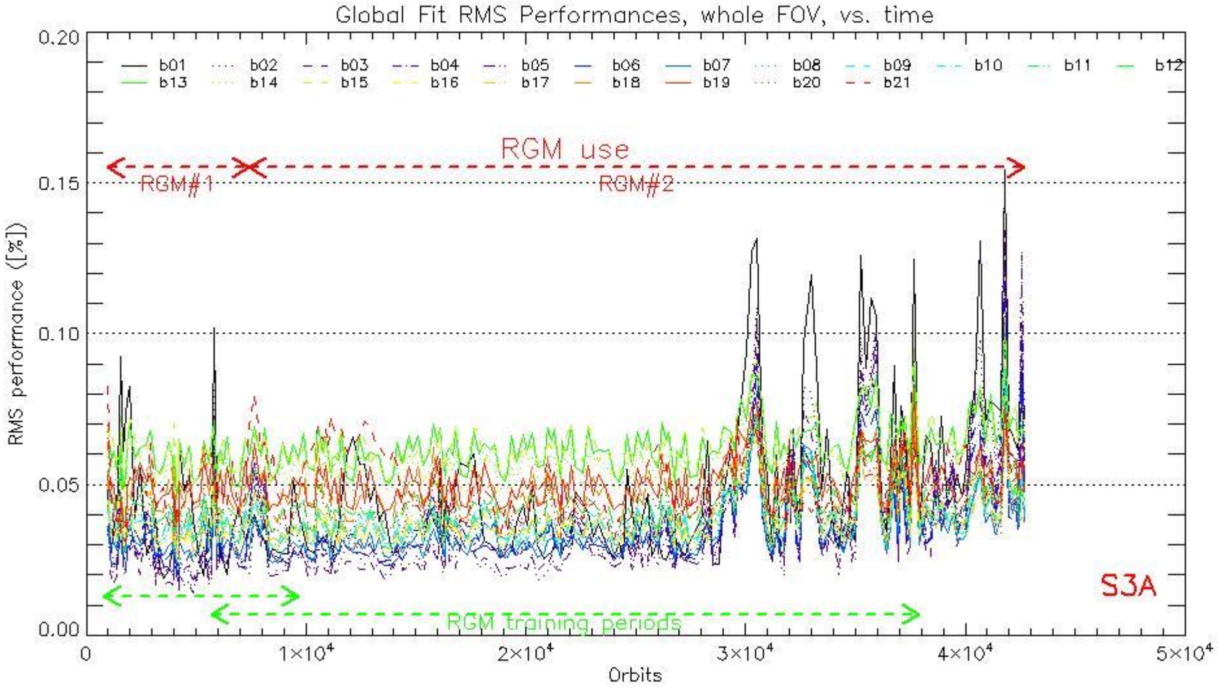

Figure 27: RMS performance of the OLCI-A Gain Model of the previous Processing Baseline as a function of orbit.

The overall instrument evolution since channel programming change (25/04/2016) is shown on Figure 28.

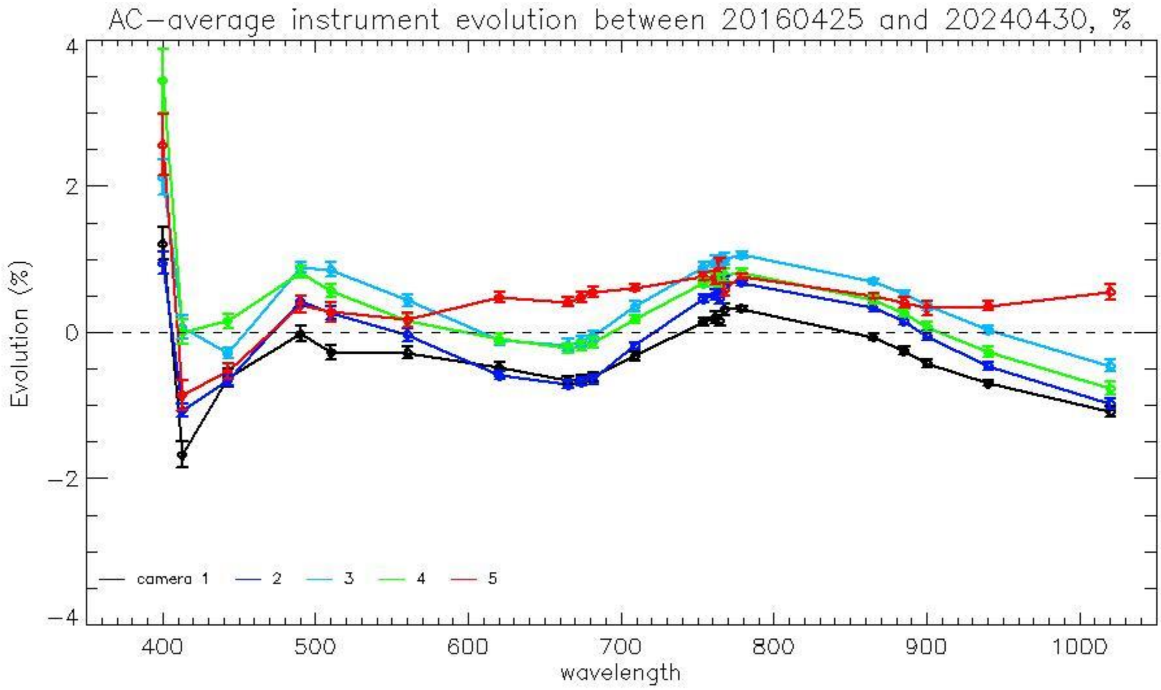

Figure 28: OLCI-A Camera-averaged instrument evolution since channel programming change (25/04/2016) and up to the most recent calibration (30/04/2024) versus wavelength.

The overall per camera performance, as a function of wavelength, and at each orbit is shown on Figure 29 as the average and standard deviation of the model over data ratio.

Finally, Figure 30 to Figure 32 show the detail of the model performance, with across-track plots of the model over data ratios at each orbit, one plot for each channel.

Comparisons of Figure 30 to Figure 32 with their counterparts in DQR of March 2024 shows the slight improvement brought by the new model whatever the level of detail.

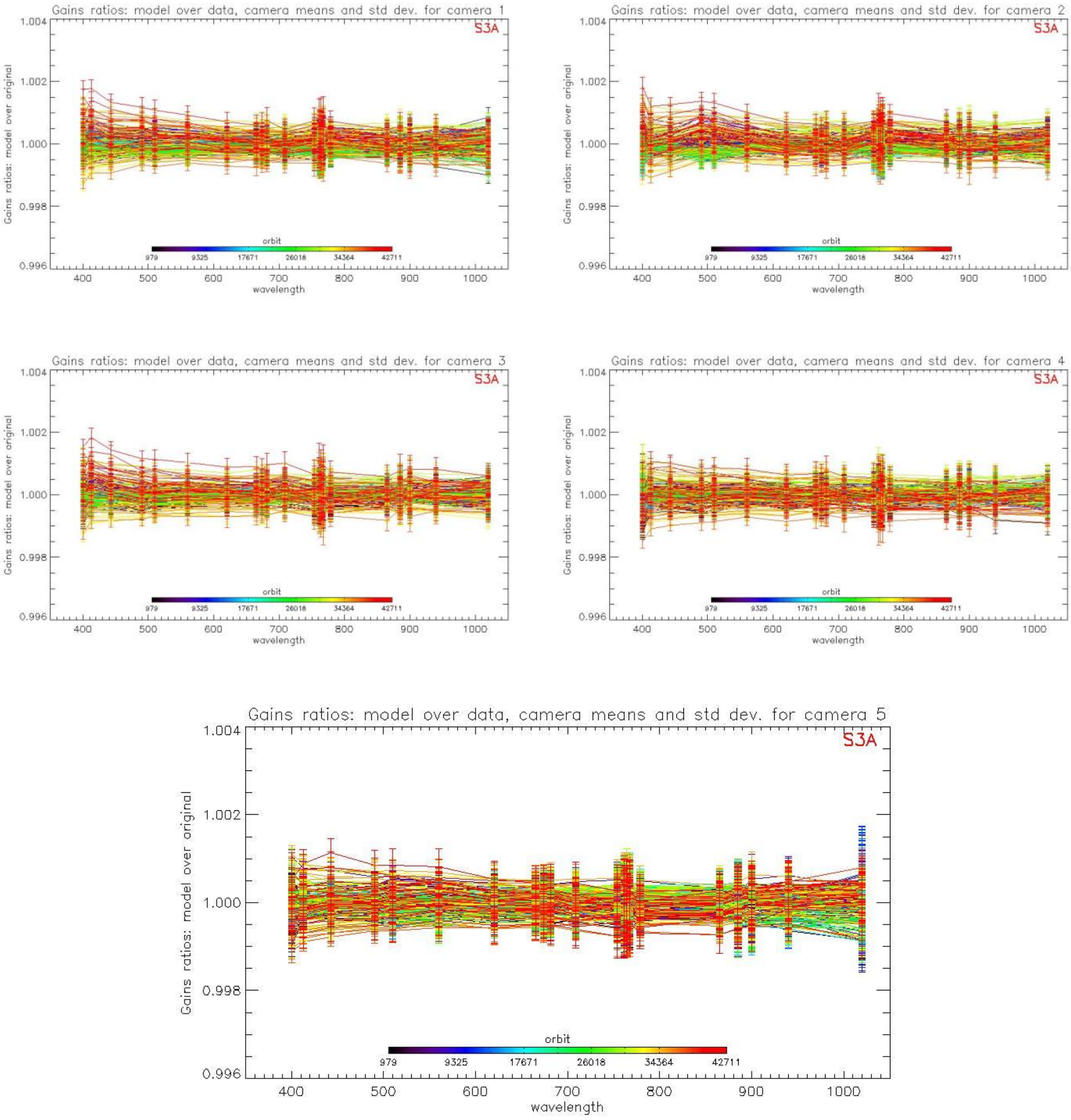

Figure 29: For the 5 cameras: OLCI-A Evolution model performance, as camera-average and standard deviation of ratio of Model over Data vs. wavelength, for each orbit of the test dataset, including 11 calibrations in extrapolation, with a colour code for each calibration from blue (oldest) to red (most recent).

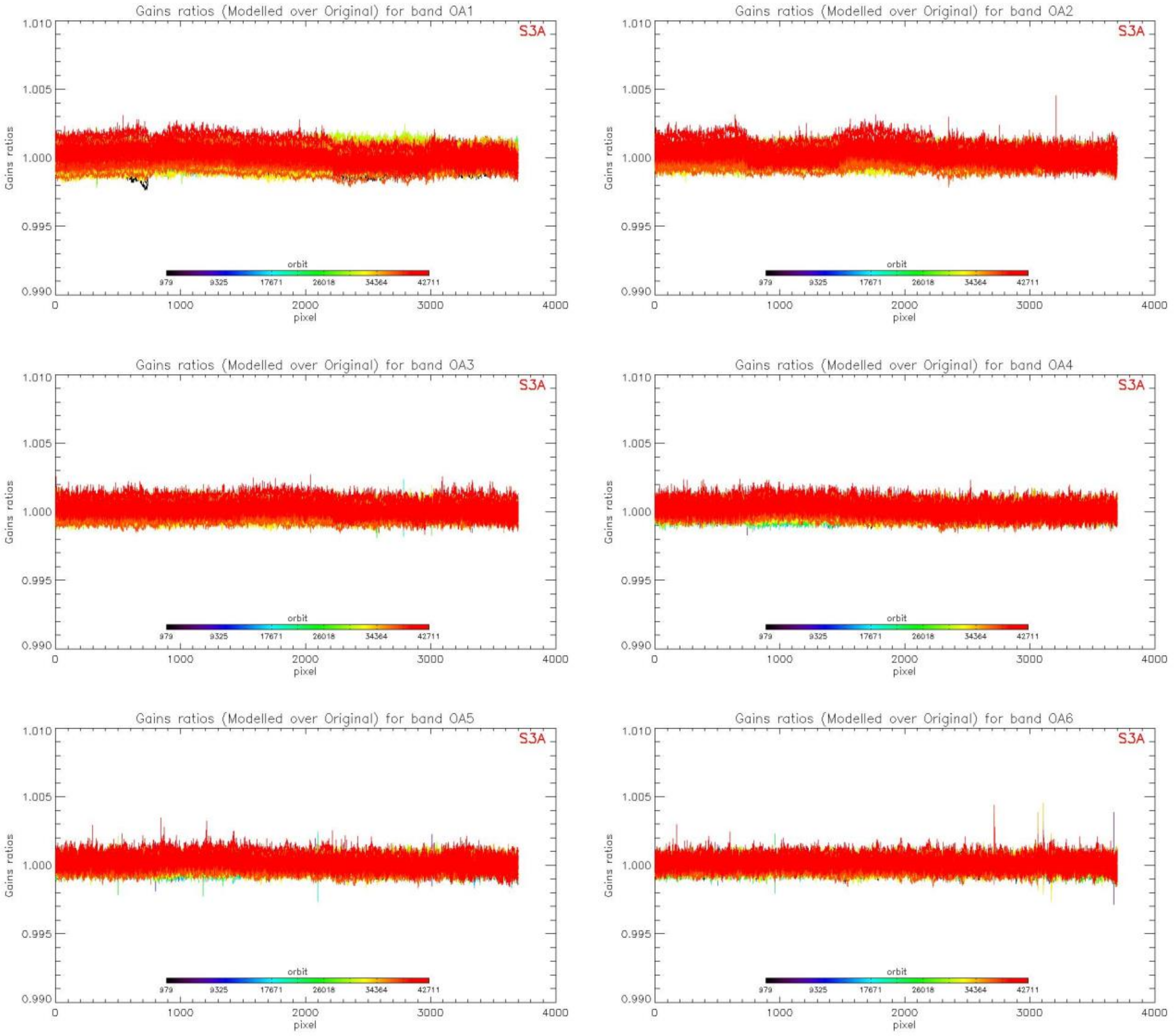

Figure 30: OLCI-A evolution model performance, as ratio of Model over Data vs. pixels, all cameras side by side, over the whole current calibration dataset (since instrument programming update), including 11 calibrations in extrapolation, channels Oa1 to Oa6.

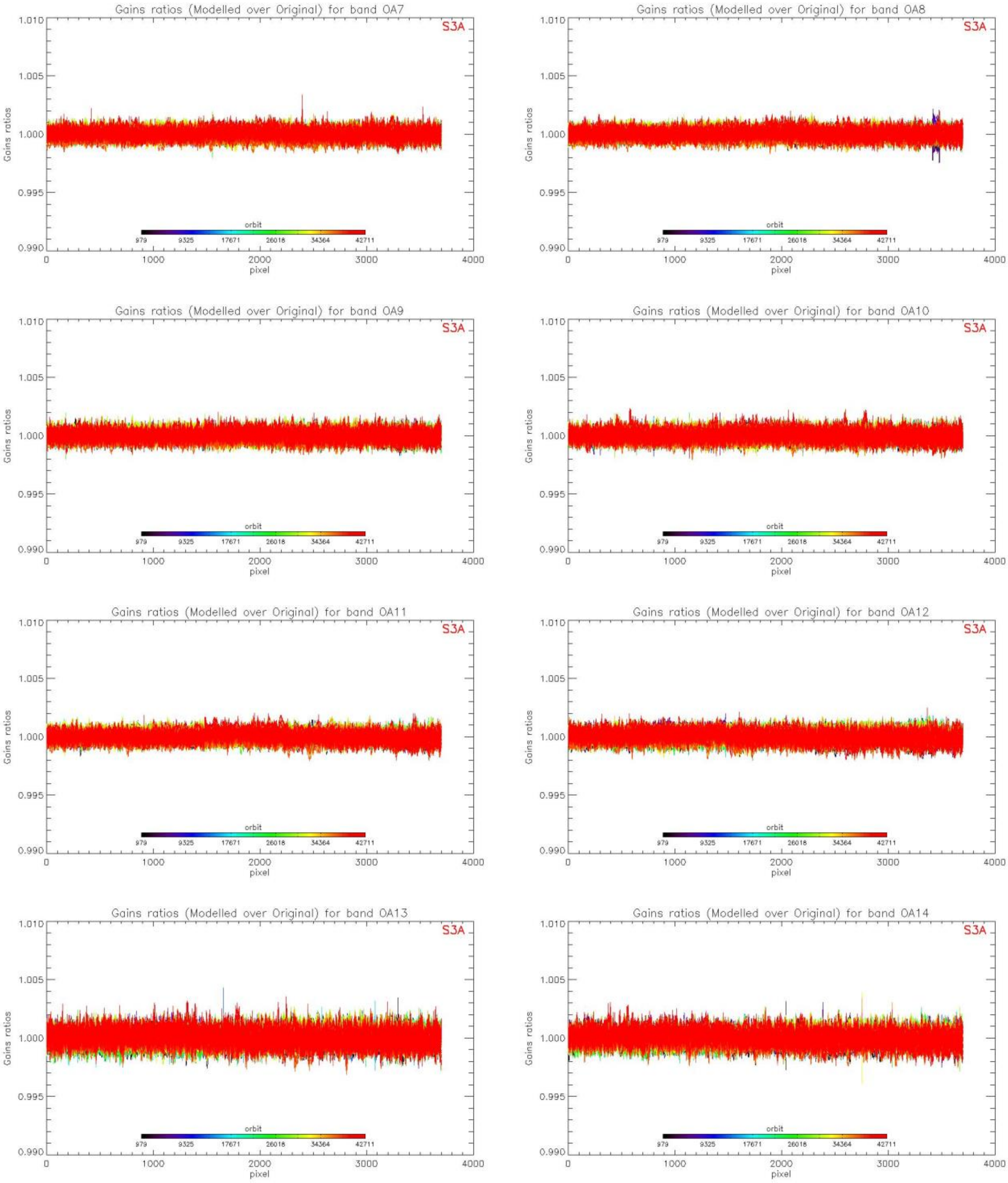

Figure 31: same as Figure 30 for channels Oa7 to Oa14.

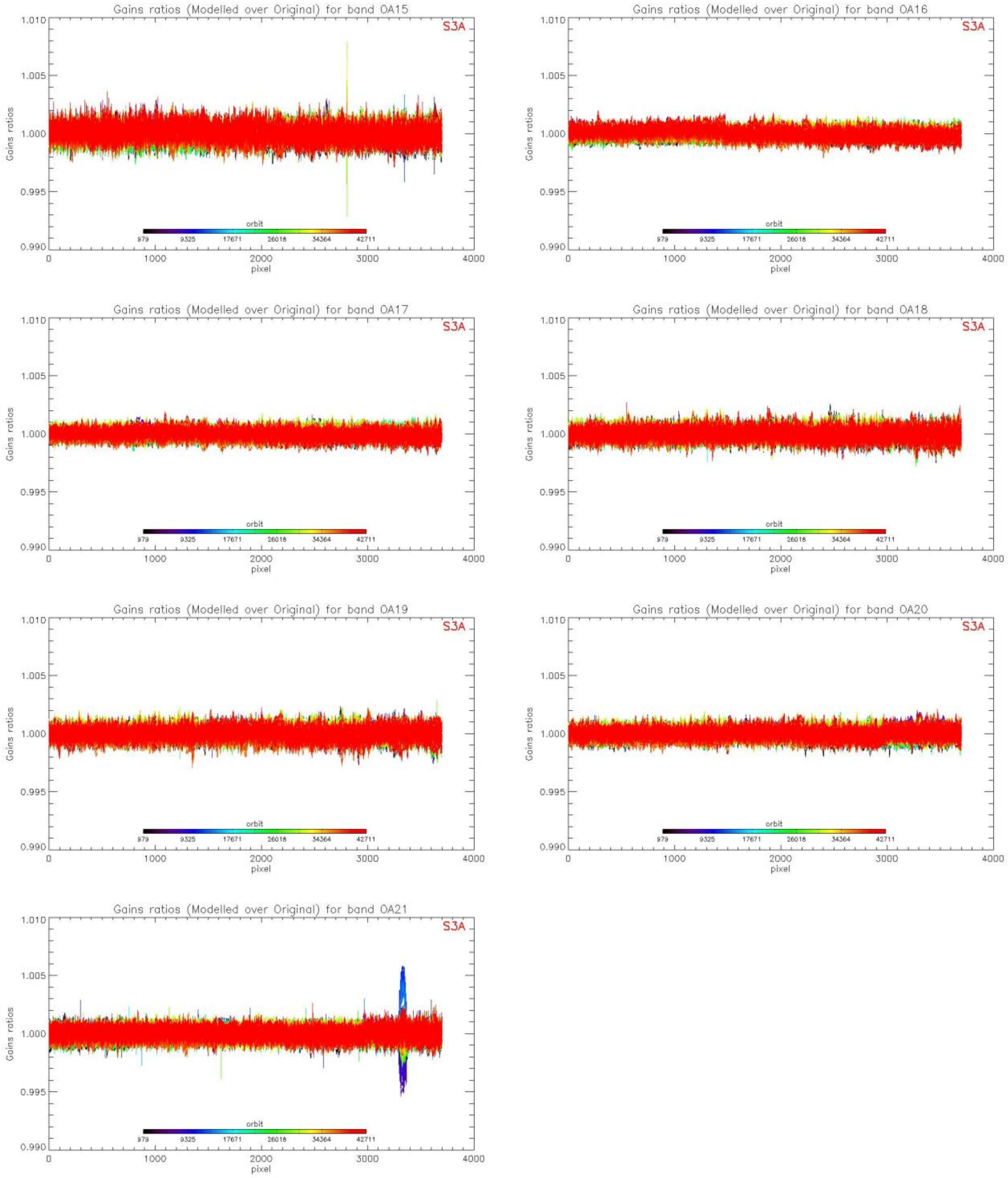

Figure 32: same as Figure 30 for channels Oa15 to Oa21.

2.2.3.2.2 OLCI-B

A new OLCI-B Radiometric Gain Model has been put in operations at PDGS on 28/02/2024 (Processing Baseline 3.27). This model has been derived on the basis of an extended Radiometric Calibration dataset (from 08/05/2018 to 28/12/2023). It includes the correction of the diffuser ageing for the five bluest bands (Oa1 to Oa5) for which it is clearly measurable. The model performance over the complete dataset (including 11 calibrations in extrapolation over about 4 months) is illustrated in Figure 33. It remains better than about 0.12% when averaged over the whole field of view for all bands at the exception of a few spikes after orbit 25000 reaching up to 0.20% for Oa02. The previous model, trained on a Radiometric Dataset limited to 24/05/2023, shows a significant drift of the model with respect to most recent data (Figure 34). Comparison of the two figures shows the slight improvement brought by the updated Model over all the mission.

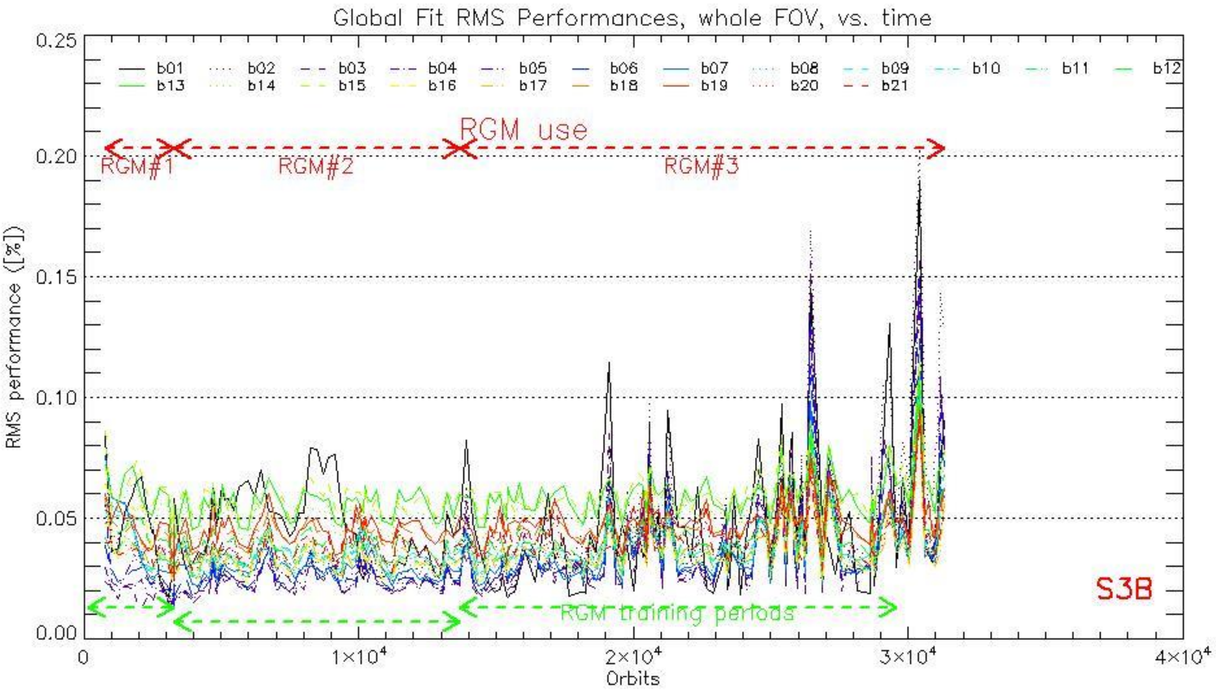

Figure 33: RMS performance of the OLCI-B Gain Model of the current processing baseline as a function of orbit.

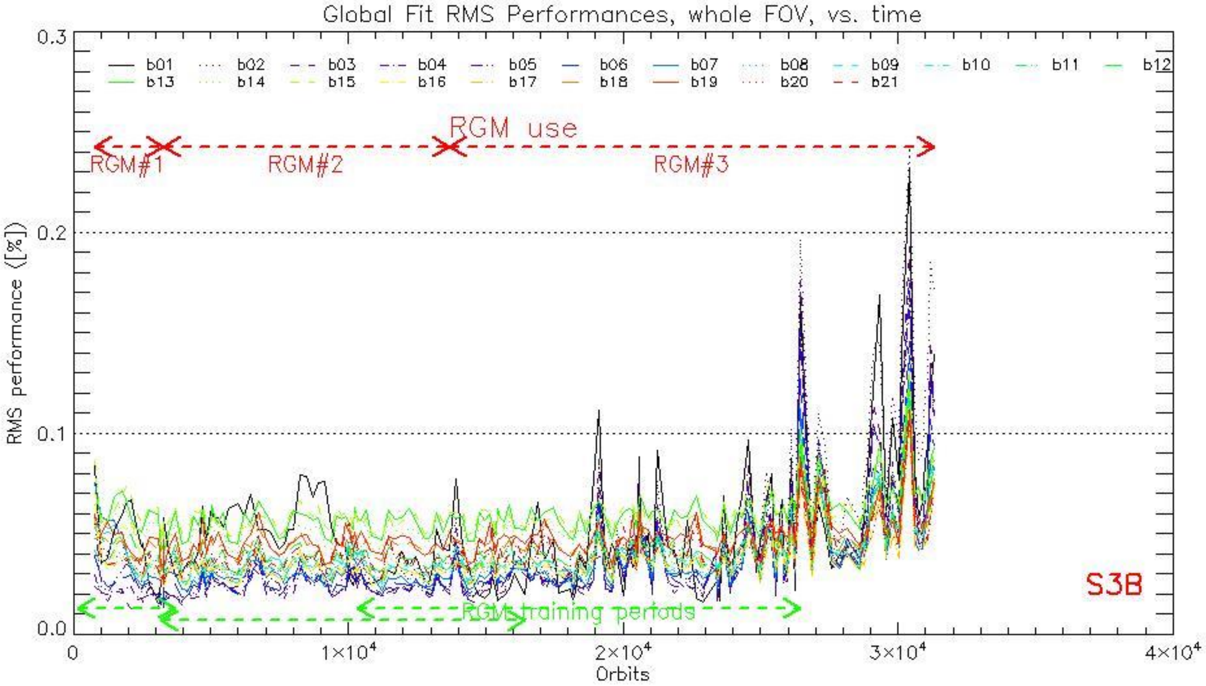

Figure 34: RMS performance of the OLCI-B Gain Model of the previous processing baseline as a function of orbit (please note the different vertical scale with respect to Figure 33).

The overall instrument evolution since channel programming change (18/06/2018) is shown on Figure 35.

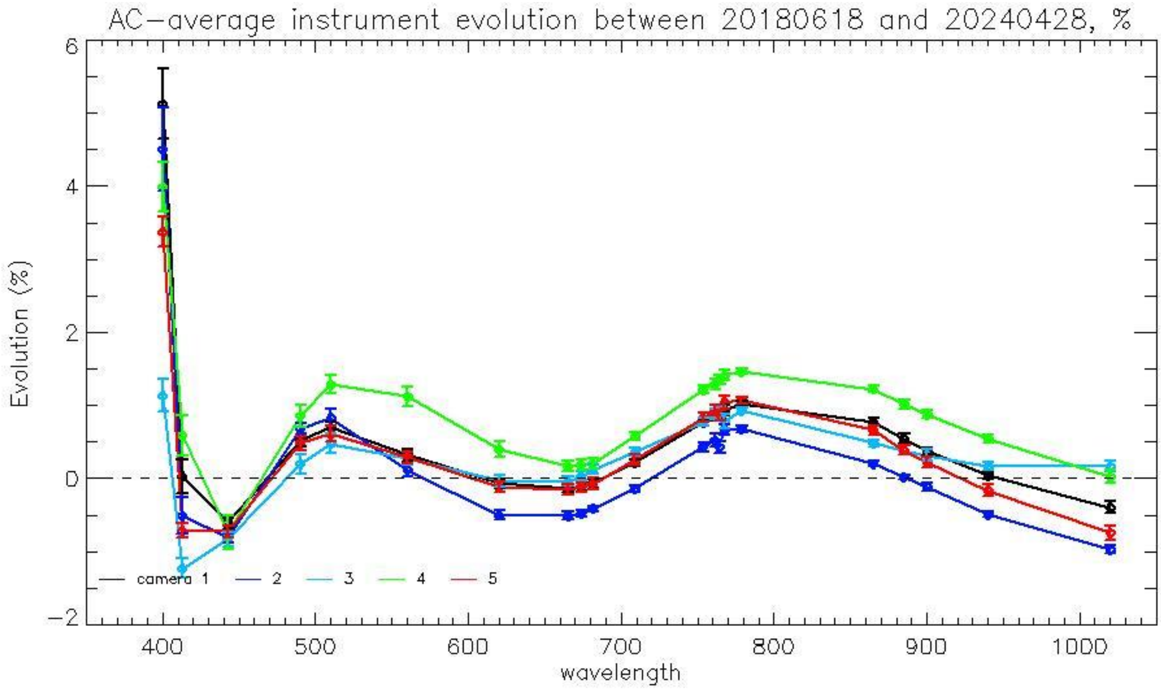

Figure 35: OLCI-B Camera-averaged instrument evolution since channel programming change (18/06/2018) and up to most recent calibration (28/04/2024) versus wavelength.

The overall per camera performance, as a function of wavelength, and at each orbit is shown on Figure 36 as the average and standard deviation of the model over data ratio.

Finally, Figure 37 to Figure 39 show the detail of the model performance, with across-track plots of the model over data ratios at each orbit, one plot for each channel.

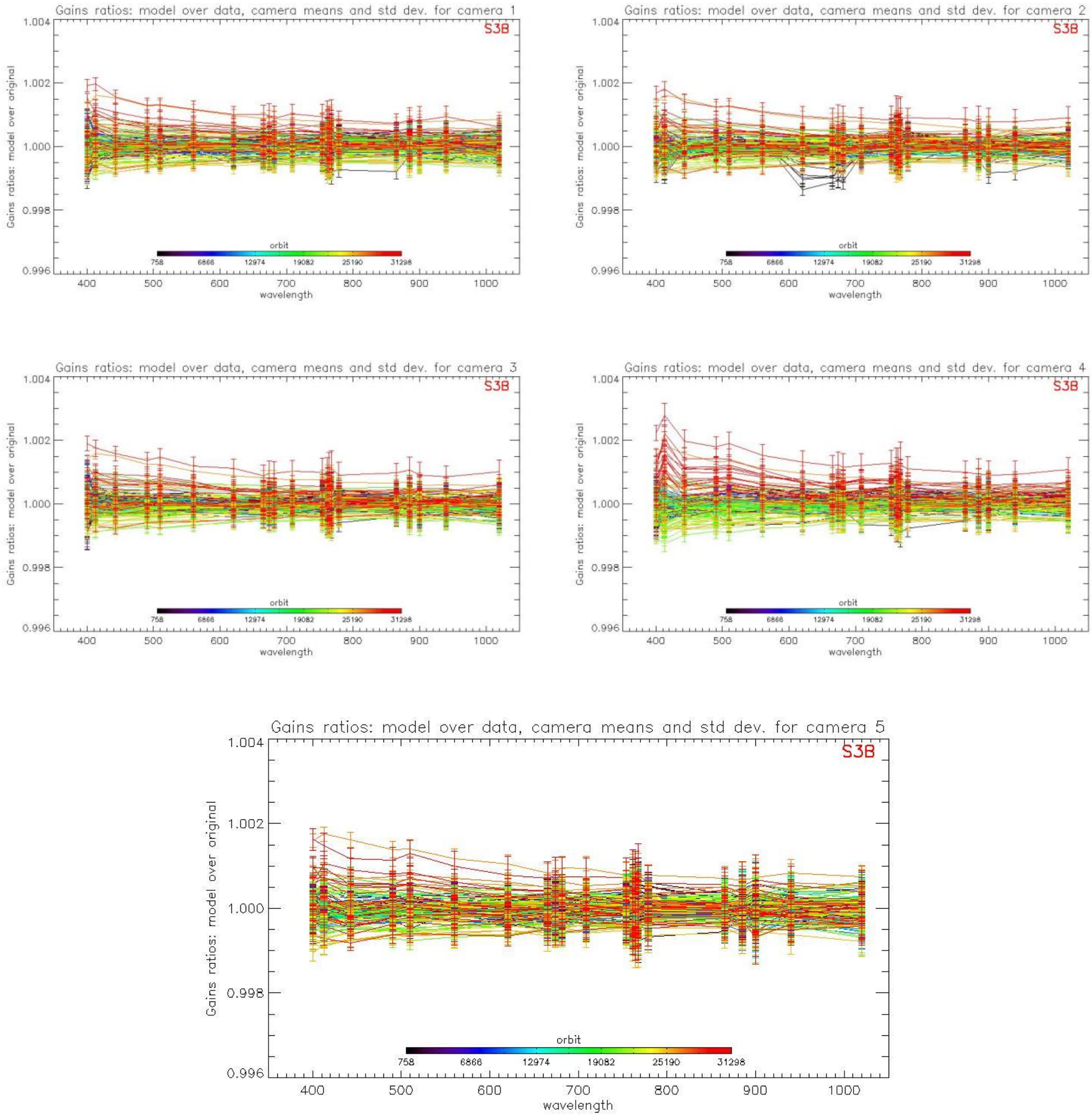

Figure 36: For the 5 cameras: OLCI-B Evolution model performance, as camera-average and standard deviation of ratio of Model over Data vs. wavelength, for each orbit of the test dataset, including 11 calibrations in extrapolation, with a colour code for each calibration from blue (oldest) to red (most recent).

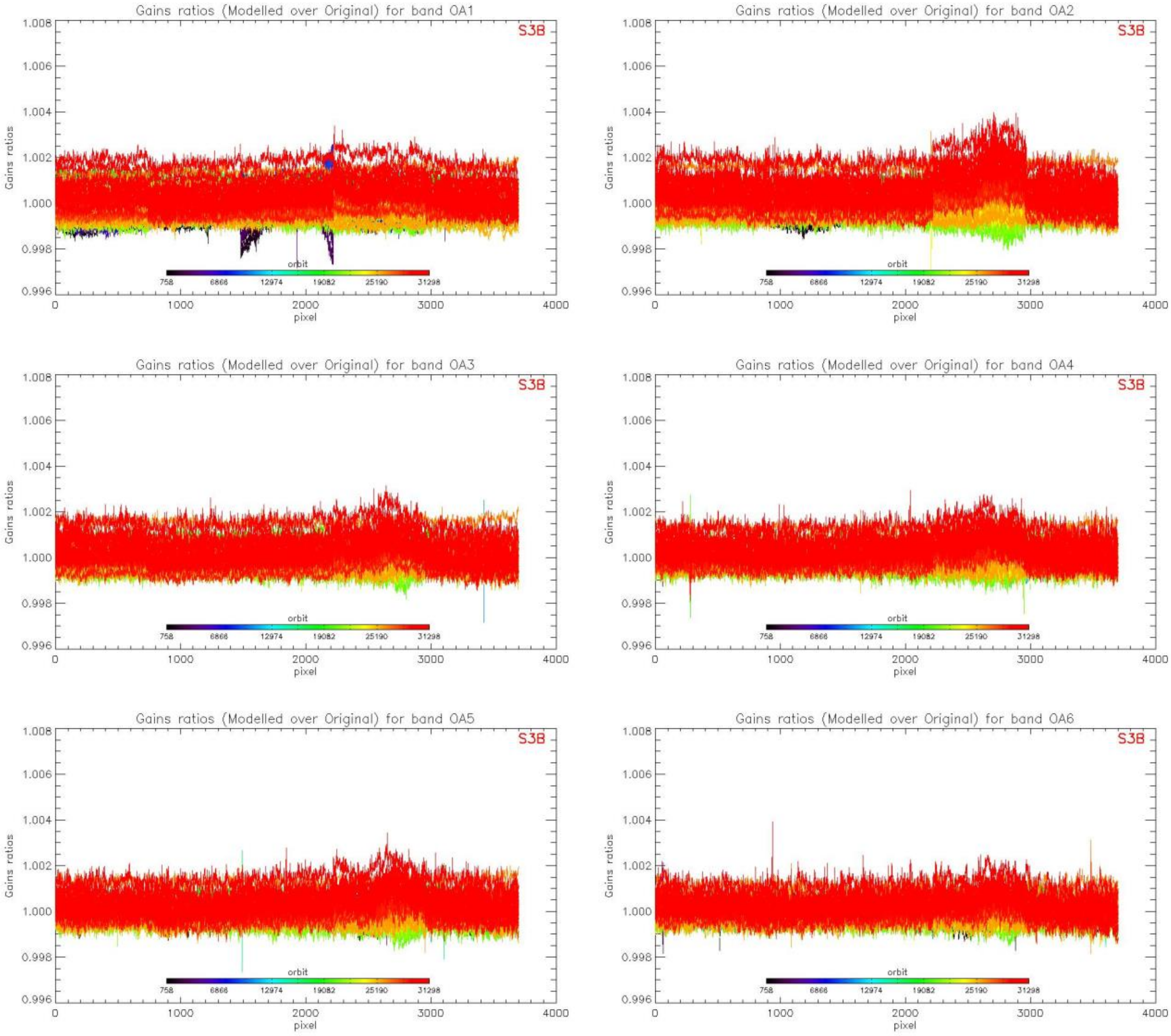

Figure 37: OLCI-B evolution model performance, as ratio of Model over Data vs. pixels, all cameras side by side, over the whole current calibration dataset (since instrument programming update), including 11 calibrations in extrapolation, channels Oa1 to Oa6.

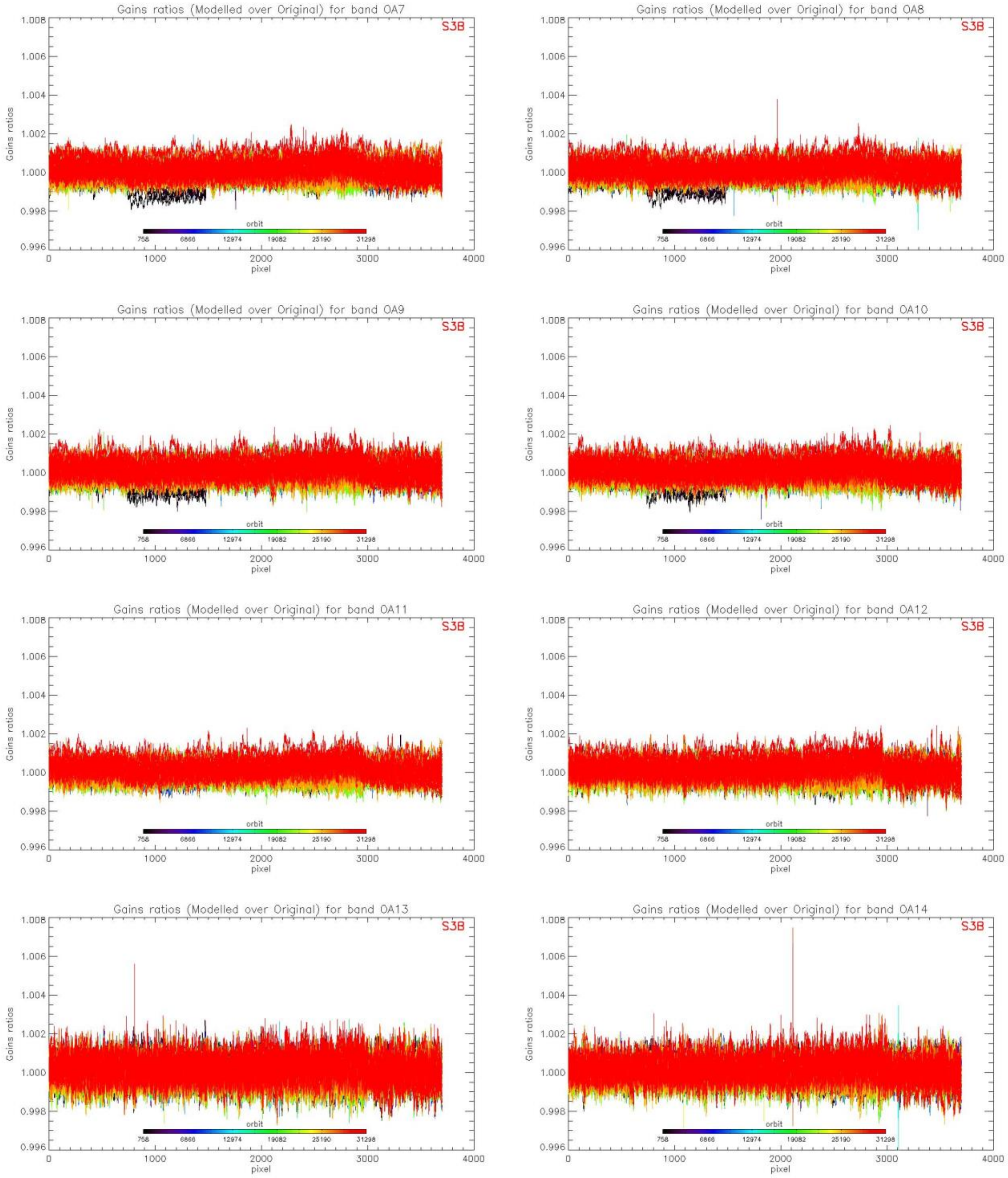

Figure 38: same as Figure 37 for channels Oa7 to Oa14.

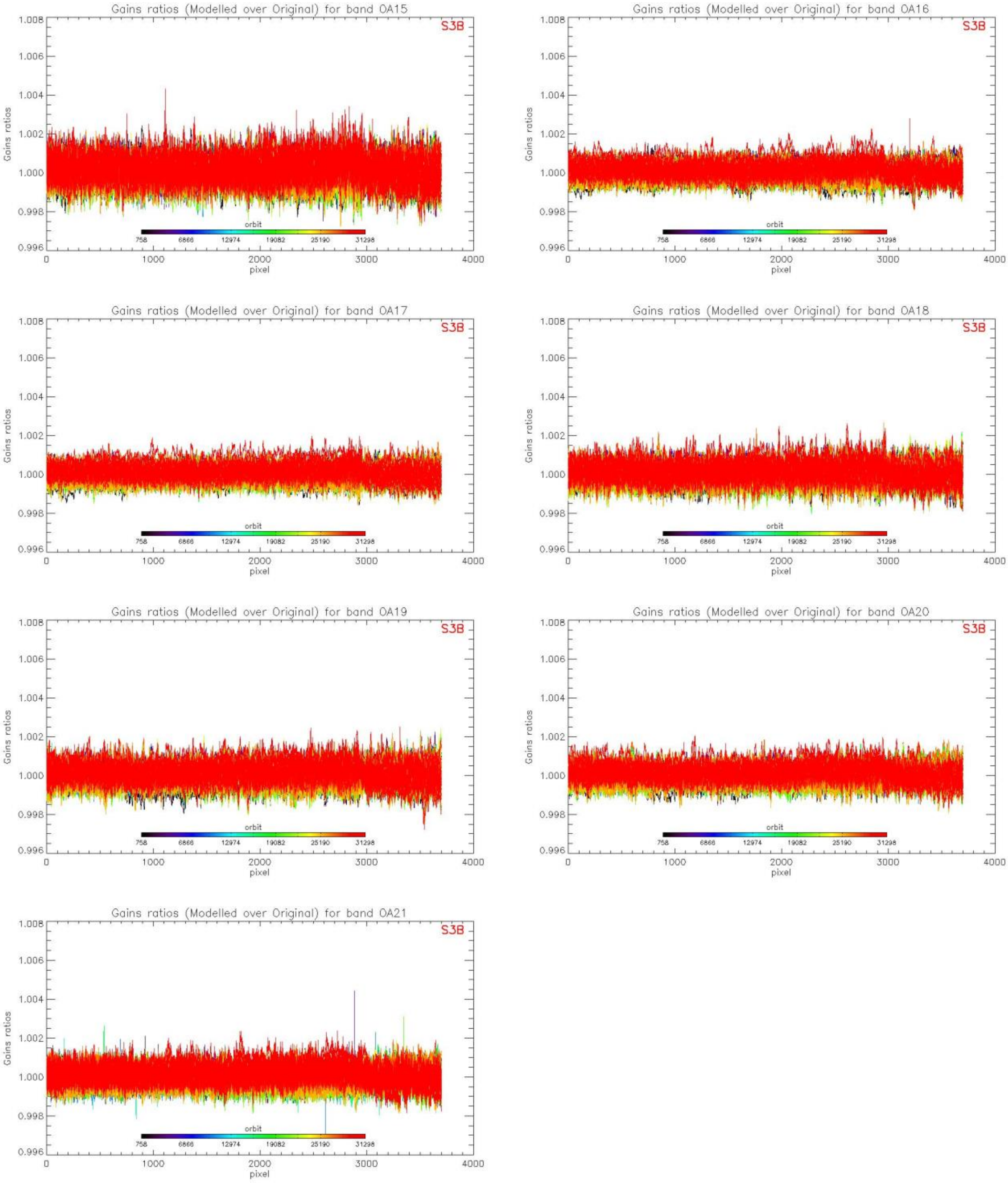

Figure 39: same as for channels Oa15 to Oa21.

2.2.4 Ageing of nominal diffuser [OLCI-L1B-CV-240]

2.2.4.1 OLCI-A

There has been no calibration sequence S05 (reference diffuser) for OLCI-A during the current reporting period.

Consequently, the last results, presented in February DQR, are considered valid.

2.2.4.2 OLCI-B

There has been no calibration sequence S05 (reference diffuser) for OLCI-B during the current reporting period.

Consequently, the last results, presented in March DQR, are considered valid.

2.2.5 Updating of calibration ADF [OLCI-L1B-CV-260]

2.2.5.1 OLCI-A

No new CAL_AX ADF has been delivered to PDGS during the report period for OLCI-A.

2.2.5.2 OLCI-B

No new CAL_AX ADF has been delivered PDGS during the report period for OLCI-B.

2.3 Spectral Calibration [OLCI-L1B-CV-400]

2.3.1 OLCI-A

There has been no S02+S03 nor S09 Spectral Calibration for OLCI-A in the reporting period.

Consequently, the last spectral calibration results, presented in March 2024 DQR, remain valid.

2.3.2 OLCI-B

There has been no S02+S03 nor S09 Spectral Calibration for OLCI-B in the reporting period.

Consequently, the last spectral calibration results, presented in March 2024 DQR, remain valid.

2.4 Signal to Noise assessment [OLCI-L1B-CV-620]

2.4.1 SNR from Radiometric calibration data

2.4.1.1 OLCI-A

SNR computed for all calibration data (S01, S04 and S05 sequences) as a function of band number is presented in Figure 40.

SNR computed for all calibration data as a function of orbit number for band Oa01 (the less stable band) is presented in Figure 41.

There is no significant evolution of this parameter during the current reporting period and the ESA requirement is fulfilled for all bands.

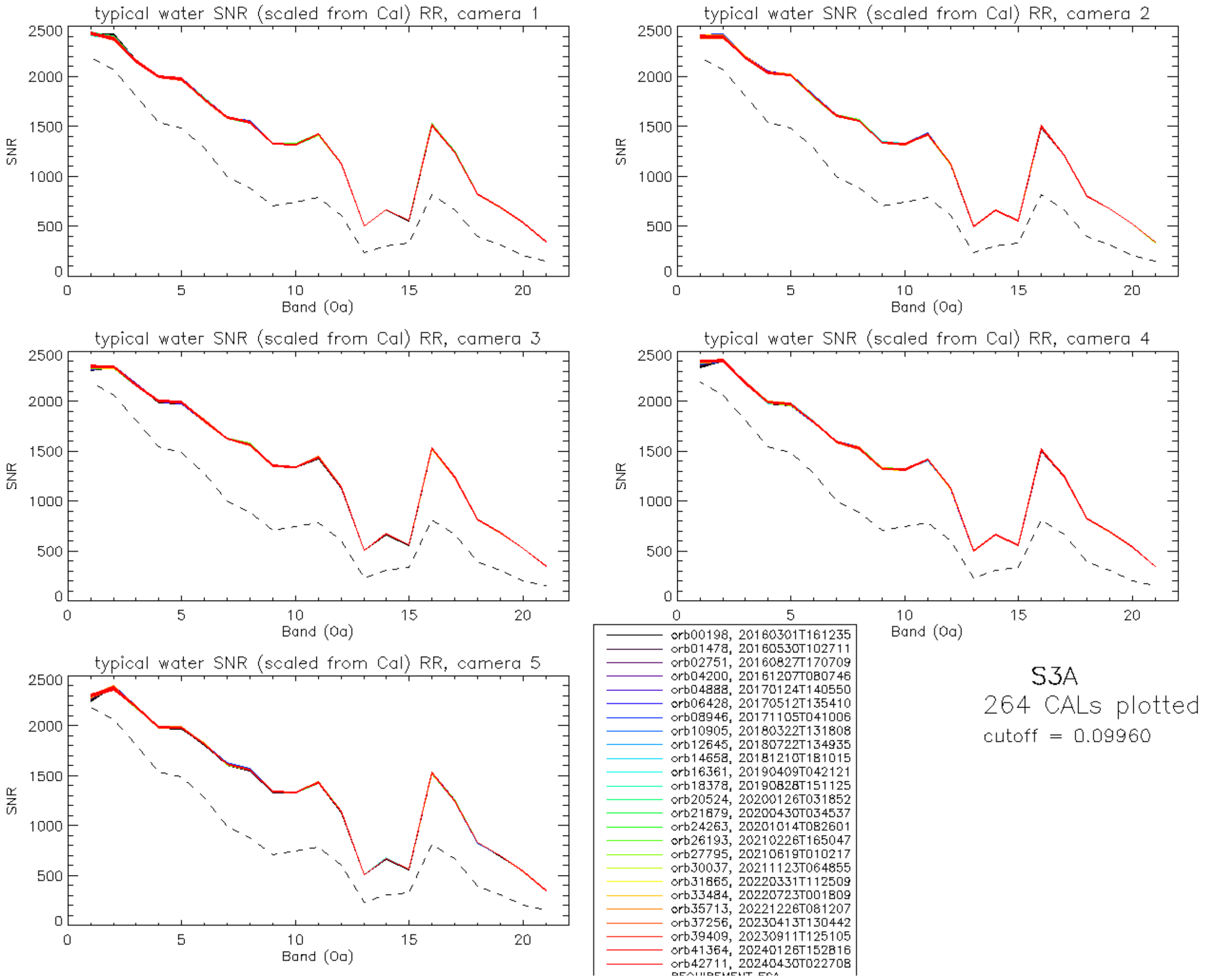

Figure 40: OLCI-A Signal to Noise ratio as a function of the spectral band for the 5 cameras. These results have been computed from radiometric calibration data. All calibrations except first one (orbit 183) are presents with the colours corresponding to the orbit number (see legend). The SNR is very stable with time: the curves for all orbits are almost superimposed. The dashed curve is the ESA requirement.

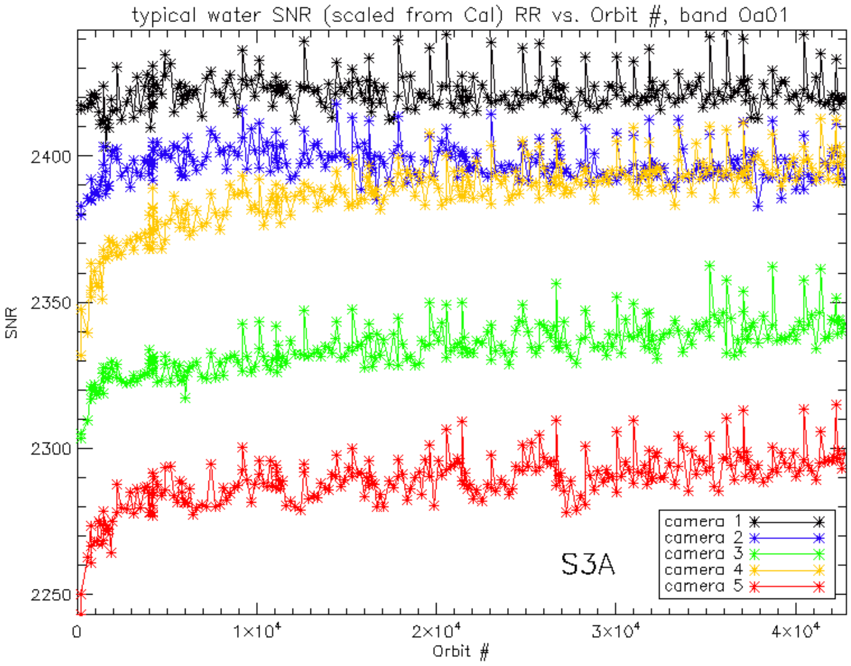

Figure 41: long-term stability of the SNR estimates from Calibration data, example of channel Oa1.

The mission averaged SNR figures are provided in Table 1 below, together with their radiance reference level. According to the OLCI SNR requirements, these figures are valid at these radiance levels and at Reduced Resolution (RR, 1.2 km). They can be scaled to other radiance levels assuming shot noise (CCD sensor noise) is the dominating term, i.e. radiometric noise can be considered Gaussian with its standard deviation varying as the square root of the signal; in other words: $SNR(L) = SNR(L_{ref}) \cdot \sqrt{\frac{L}{L_{ref}}}$. Following the same assumption, values at Full Resolution (300m) can be derived from RR ones as 4 times smaller.

Table 1: OLCI-A SNR figures as derived from Radiometric Calibration data. Figures are given for each camera (time average and standard deviation), and for the whole instrument. The requirement and its reference radiance level are recalled (in mW.sr^{-1}.m^{-2}.nm^{-1}).

	L_{ref}	SNR	C1		C2		C3		C4		C5		All	
nm	LU	RQT	avg	*std*	avg	*std*	avg	*std*	avg	*std*	avg	*std*	avg	*std*
400.000	63.0	2188	2422	6.2	2397	6.3	2334	8.7	2386	12.1	2288	9.4	2366	7.1
412.000	74.1	2061	2385	9.8	2401	8.0	2339	5.1	2400	5.2	2378	9.6	2381	6.1
442.000	65.6	1811	2156	6.2	2195	6.2	2163	5.0	2185	4.3	2192	5.9	2178	4.3
490.000	51.2	1541	1999	4.8	2036	4.8	1998	4.3	1984	4.4	1988	4.3	2001	3.1
510.000	44.4	1488	1978	5.4	2014	4.8	1986	4.5	1967	4.3	1984	4.1	1986	3.3
560.000	31.5	1280	1774	4.7	1802	4.0	1803	4.7	1794	3.8	1819	3.3	1799	2.9
620.000	21.1	997	1590	4.1	1608	4.2	1624	3.2	1593	3.2	1616	3.3	1606	2.5
665.000	16.4	883	1545	4.2	1556	4.4	1566	3.9	1533	3.5	1561	3.5	1552	2.9
674.000	15.7	707	1327	3.4	1336	3.7	1350	2.8	1323	3.2	1343	3.2	1336	2.4
681.000	15.1	745	1319	3.6	1325	3.4	1338	2.7	1314	2.5	1334	3.2	1326	2.1
709.000	12.7	785	1420	4.1	1420	3.9	1435	3.4	1414	3.4	1431	3.0	1424	2.6
754.000	10.3	605	1127	3.0	1121	2.7	1136	3.1	1125	2.5	1140	2.6	1130	2.1
761.000	6.1	232	502	1.1	499	1.1	505	1.1	501	1.0	508	1.3	503	0.8
764.000	7.1	305	662	1.5	658	1.5	668	2.0	662	1.5	670	1.9	664	1.2
768.000	7.6	330	558	1.4	555	1.2	563	1.3	557	1.3	564	1.2	559	0.9
779.000	9.2	812	1516	4.5	1499	4.3	1527	5.0	1512	4.7	1527	4.6	1516	3.9
865.000	6.2	666	1243	3.5	1213	3.4	1240	3.7	1247	3.5	1250	2.7	1239	2.6
885.000	6.0	395	823	1.7	801	1.6	814	2.0	824	1.5	831	1.6	819	1.0
900.000	4.7	308	690	1.6	673	1.2	684	1.6	693	1.6	698	1.4	688	1.0
940.000	2.4	203	534	1.2	522	1.1	525	1.0	539	1.1	542	1.3	532	0.7
1020.000	3.9	152	344	0.9	337	0.8	348	0.7	345	0.8	351	0.8	345	0.5

2.4.1.2 OLCI-B

SNR computed for all OLCI-B calibration data (S01, S04 (but not the dark-only S04) and S05 sequences) as a function of band number is presented in Figure 42.

SNR computed for all OLCI-B calibration data as a function of orbit number for band Oa01 (the less stable band) is presented in Figure 43.

As for OLCI-A the SNR is very stable in time. There is no significant evolution of this parameter during the current reporting and the ESA requirement is fulfilled for all bands.

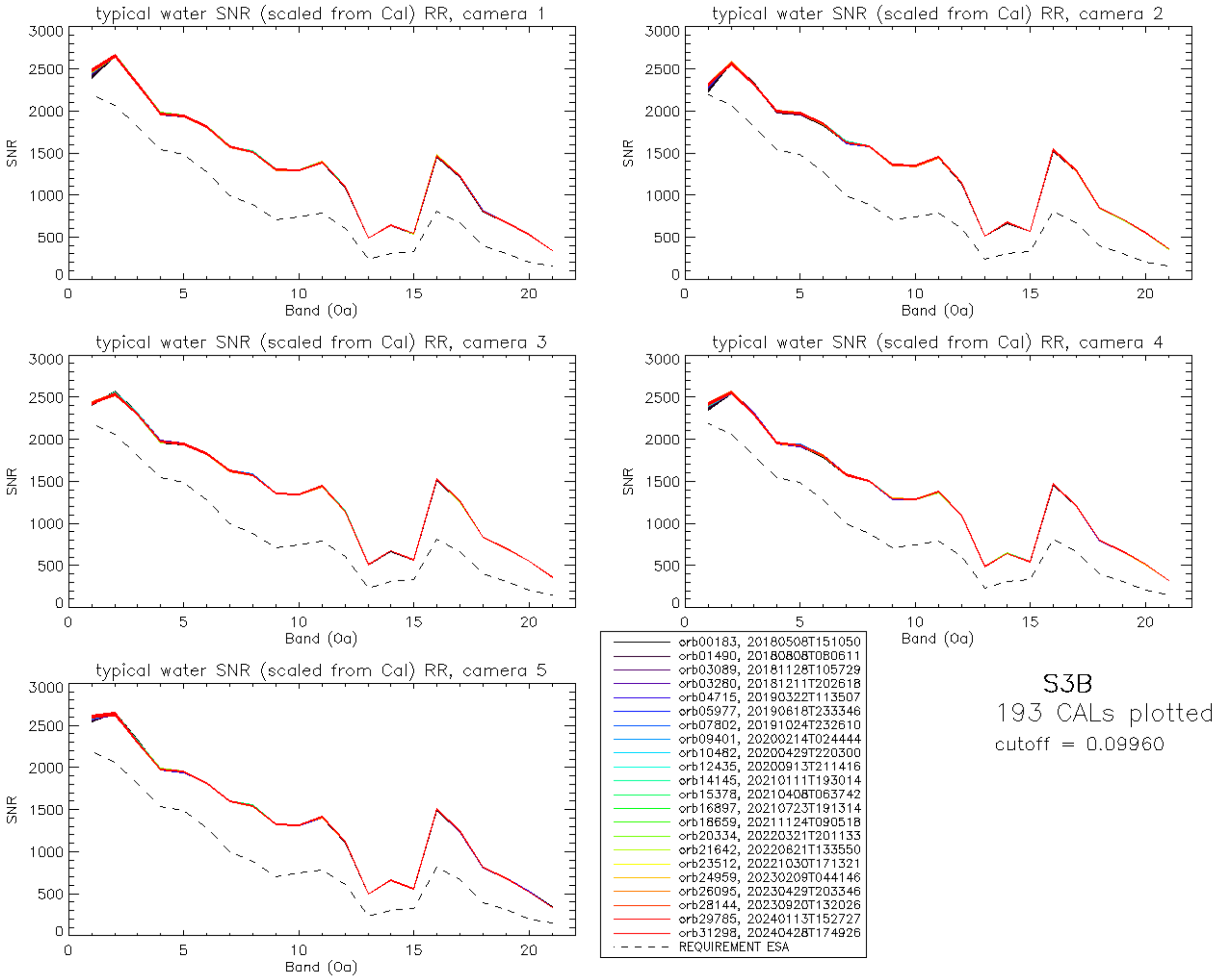

Figure 42: OLCI-B Signal to Noise ratio as a function of the spectral band for the 5 cameras. These results have been computed from radiometric calibration data. All calibrations except first one (orbit 167) are presents with the colours corresponding to the orbit number (see legend). The SNR is very stable with time: the curves for all orbits are almost superimposed. The dashed curve is the ESA requirement.

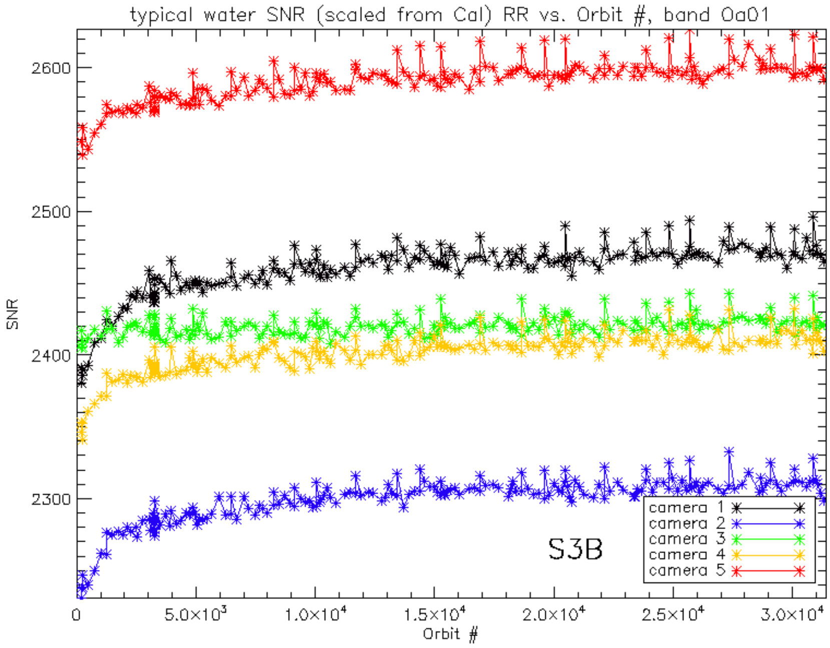

Figure 43: long-term stability of the OLCI-B SNR estimates from Calibration data, example of channel Oa1.

Table 2: OLCI-B SNR figures as derived from Radiometric Calibration data. Figures are given for each camera (time average and standard deviation), and for the whole instrument. The requirement and its reference radiance level are recalled (in mW.sr^{-1}.m^{-2}.nm^{-1}).

	L_{ref}	SNR	C1		C2		C3		C4		C5		All	
nm	LU	RQT	avg	*std*	avg	*std*	avg	*std*	avg	*std*	avg	*std*	avg	*std*
400.000	63.0	2188	2460	18.4	2299	16.3	2420	6.9	2401	13.9	2590	14.3	2434	13.0
412.000	74.1	2061	2654	7.3	2568	7.1	2541	9.1	2549	6.7	2635	8.3	2589	6.2
442.000	65.6	1811	2322	7.0	2315	6.4	2297	7.3	2300	7.3	2307	6.8	2308	6.0
490.000	51.2	1541	1966	4.9	1990	5.6	1971	5.0	1953	4.6	1979	4.5	1972	3.8
510.000	44.4	1488	1939	4.8	1969	6.0	1942	5.0	1925	4.9	1951	4.7	1945	4.0
560.000	31.5	1280	1813	4.6	1848	4.8	1829	4.6	1805	4.5	1817	3.8	1822	3.4
620.000	21.1	997	1572	4.2	1626	4.5	1624	3.9	1577	3.6	1600	3.6	1600	3.0
665.000	16.4	883	1513	4.0	1578	3.8	1573	3.8	1501	3.1	1546	3.5	1542	2.7
674.000	15.7	707	1300	3.8	1358	3.6	1353	3.1	1292	2.6	1327	2.9	1326	2.3
681.000	15.1	745	1293	3.5	1347	3.3	1343	3.0	1285	2.8	1316	2.8	1317	2.2
709.000	12.7	785	1390	3.9	1447	3.9	1443	4.1	1373	2.8	1412	3.5	1413	2.9
754.000	10.3	605	1096	3.4	1143	3.5	1142	3.2	1090	2.7	1116	3.1	1117	2.7
761.000	6.1	232	488	1.1	509	1.2	509	1.4	486	1.2	498	1.3	498	0.9
764.000	7.1	305	643	1.6	673	2.0	672	1.8	642	1.8	658	1.8	658	1.5
768.000	7.6	330	542	1.4	568	1.4	564	1.3	541	1.3	555	1.5	554	1.0
779.000	9.2	812	1467	4.0	1536	4.6	1527	5.0	1468	4.0	1507	4.0	1501	3.6
865.000	6.2	666	1221	3.4	1288	3.8	1259	3.5	1206	3.5	1238	2.8	1242	2.7
885.000	6.0	395	808	2.1	848	1.9	834	1.9	799	1.8	815	2.1	821	1.4
900.000	4.7	308	679	1.5	714	1.9	704	1.7	670	1.5	683	1.5	690	1.1
940.000	2.4	203	527	1.3	549	1.6	551	1.2	510	1.1	522	1.3	532	0.9
1020.000	3.9	152	336	0.8	358	1.1	358	0.8	318	0.7	338	0.9	342	0.6

2.5 Geometric Calibration/Validation

2.5.1 OLCI-A

OLCI-A georeferencing performance is compliant since the introduction of MPC Geometric Calibration, put in production on the 14th of March 2018. It has however significantly improved after its last full revision of GCMs (Geometric Calibration Models, or platform to instrument alignment quaternions) and IPPVMs (Instrument Pixels Pointing Vectors) both derived using the GeoCal Tool and put in production on 30/07/2019.

The following figures (Figure 44 to Figure 49) show time series of the overall RMS performance (requirement criterion) and of the across-track and along-track biases for each camera. New plots (Figure 50 and Figure 51) introduce monitoring of the performance homogeneity within the field of view: georeferencing errors in each direction at camera transitions (difference between last pixel of camera N and first pixel of camera N+1) and within a given camera (maximum bias minus minimum inside each camera). The performance improvement since the 30/07/2019 is significant on most figures: the global RMS value decreases form around 0.35 to about 0.2 (Figure 44), the across-track biases decrease significantly for all cameras (Figure 45 to Figure 49), the along-track bias reduces for at least camera 3 (Figure 47) and the field of view homogeneity improves drastically (Figure 50 and Figure 51, but also reduction of the dispersion – distance between the ± 1 sigma lines – in Figure 45 to Figure 49).

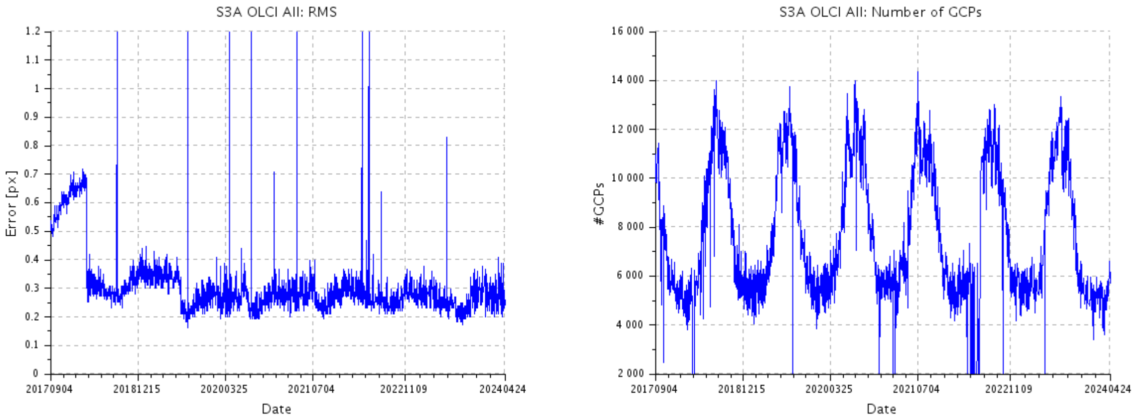

Figure 44: overall OLCI-A georeferencing RMS performance time series (left) and number of validated control points corresponding to the performance time series (right) over the whole monitoring period

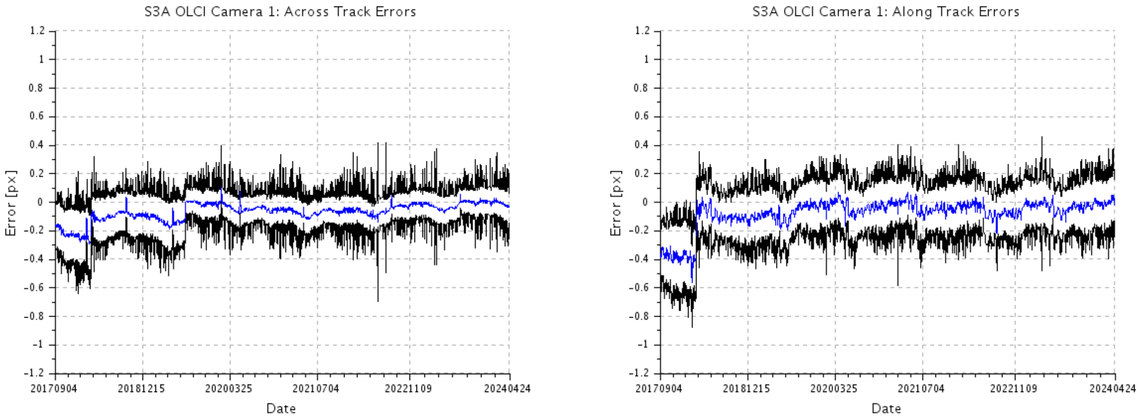

Figure 45: across-track (left) and along-track (right) OLCI-A georeferencing biases time series for Camera 1. Blue line is the average, black lines are average plus and minus 1 sigma.

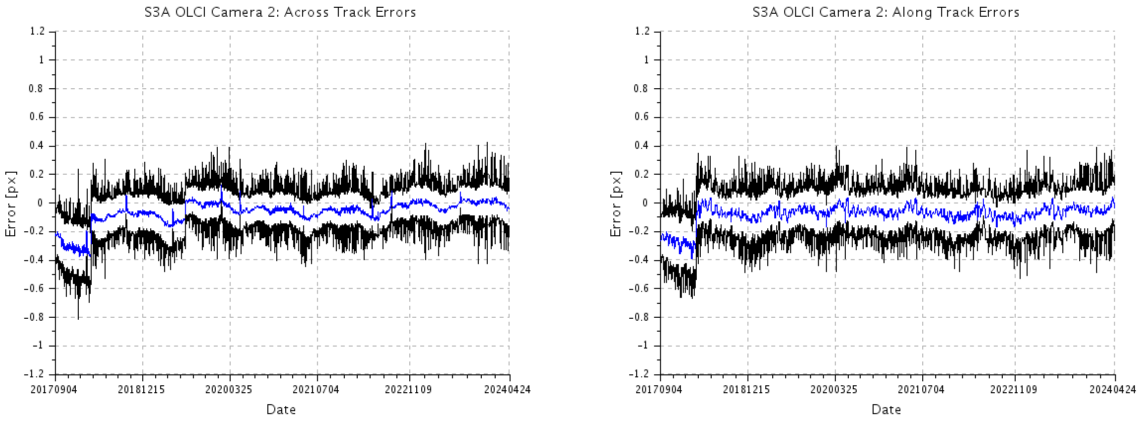

Figure 46: same as Figure 45 for Camera 2.

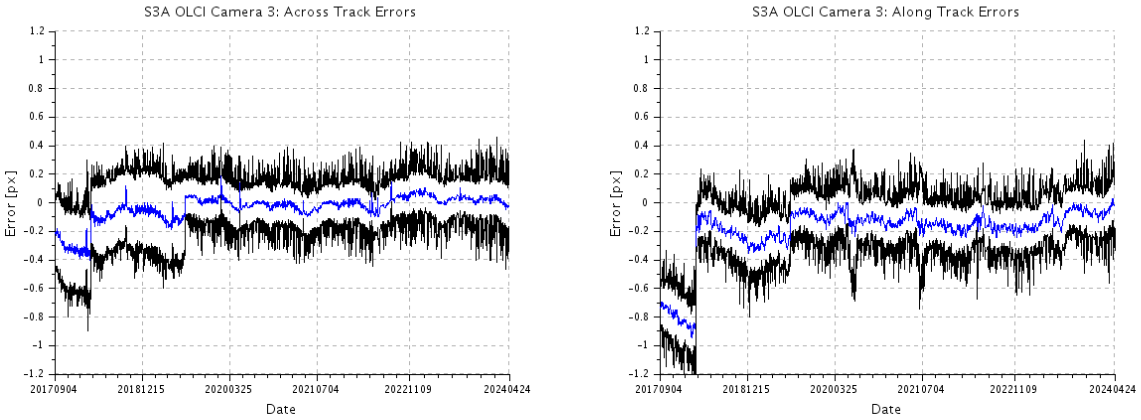

Figure 47: same as Figure 45 for Camera 3.

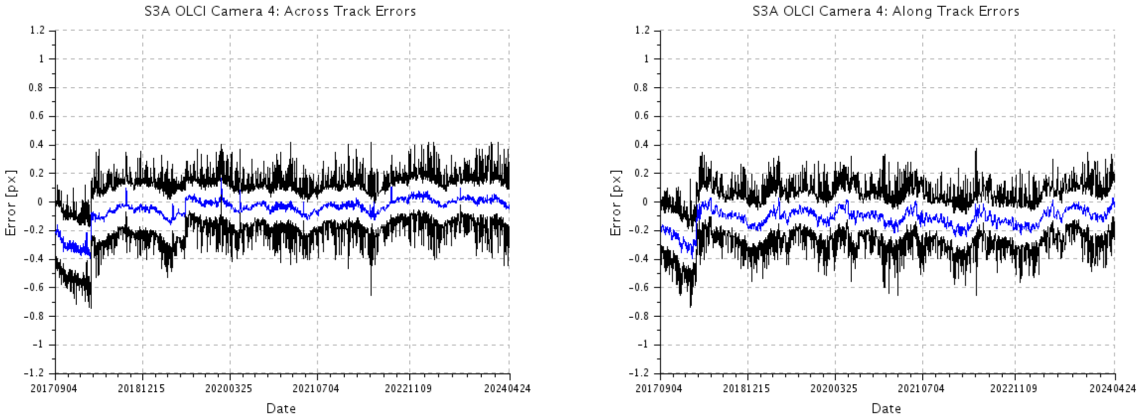

Figure 48: same as Figure 45 for Camera 4.

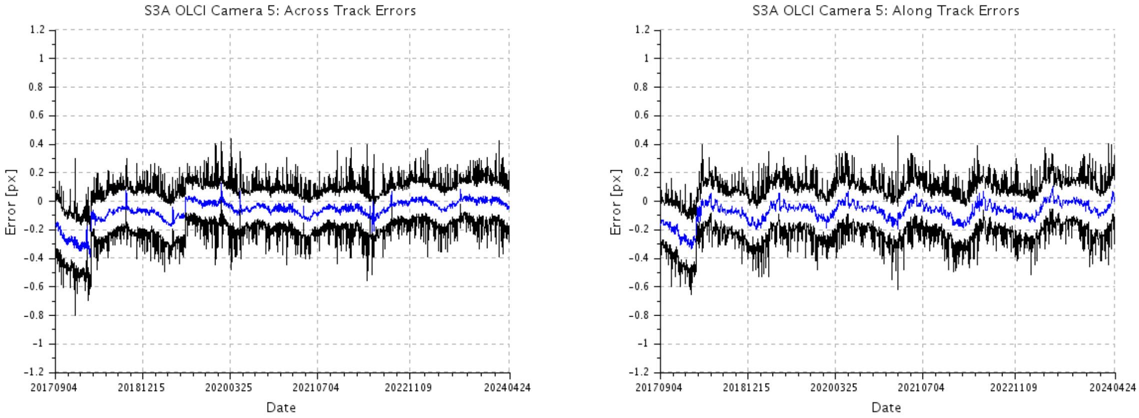

Figure 49: same as Figure 45 for Camera 5.

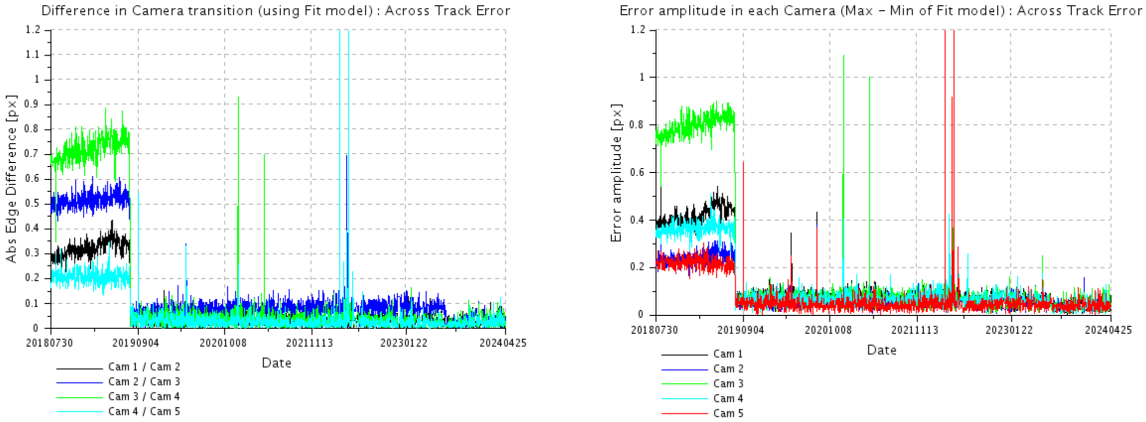

Figure 50: OLCI-A spatial across-track misregistration at each camera transition (left) and maximum amplitude of the across-track error within each camera (left).

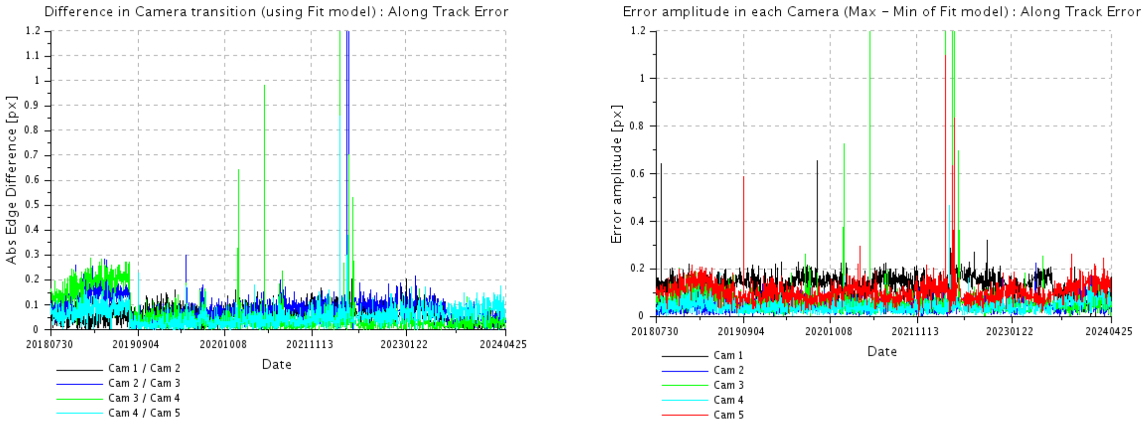

Figure 51: OLCI-A spatial along-track misregistration at each camera transition (left) and maximum amplitude of the along-track error within each camera (left).

2.5.2 OLCI-B

Georeferencing performance of OLCI-B improved significantly with the fourth geometric calibration introduced the 30/07/2019. However, the instrument pointing is still evolving, in particular for camera 2 (Figure 58) and a new geometric calibration has been done and introduced in the processing chain on the 16th of April 2020. Its impact is significant on the along-track biases of all cameras (Figure 53 to Figure 57), but also on the continuity at camera interfaces (Figure 58, left) and on intra-camera homogeneity (Figure 58, right). Since then, further adjustments to the geometric calibration have been introduced, mainly to correct the along-track drifts. The most recent was put in production on 29/07/2021 and its effect can be seen e.g. on left graphs of Figure 54, Figure 55 and Figure 57 (across-track biases of cameras 2, 3 & 5).

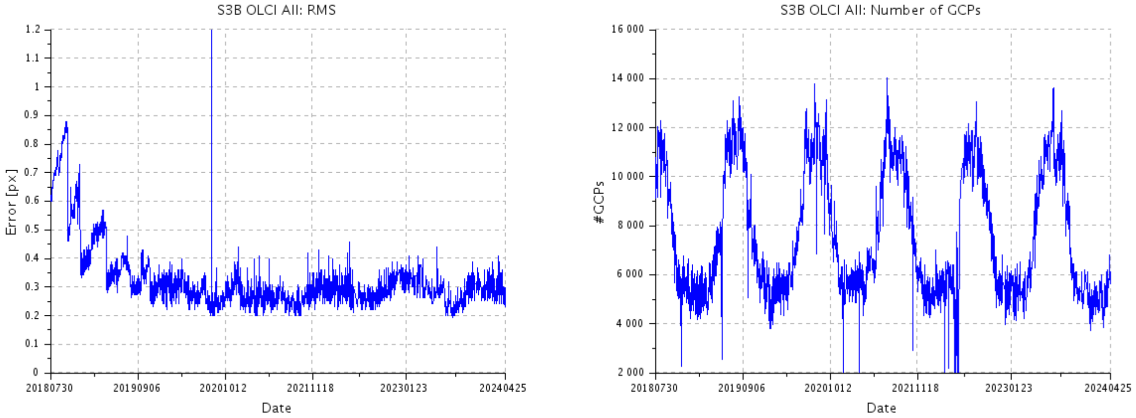

Figure 52: overall OLCI-B georeferencing RMS performance time series over the whole monitoring period (left) and corresponding number of validated control points (right)

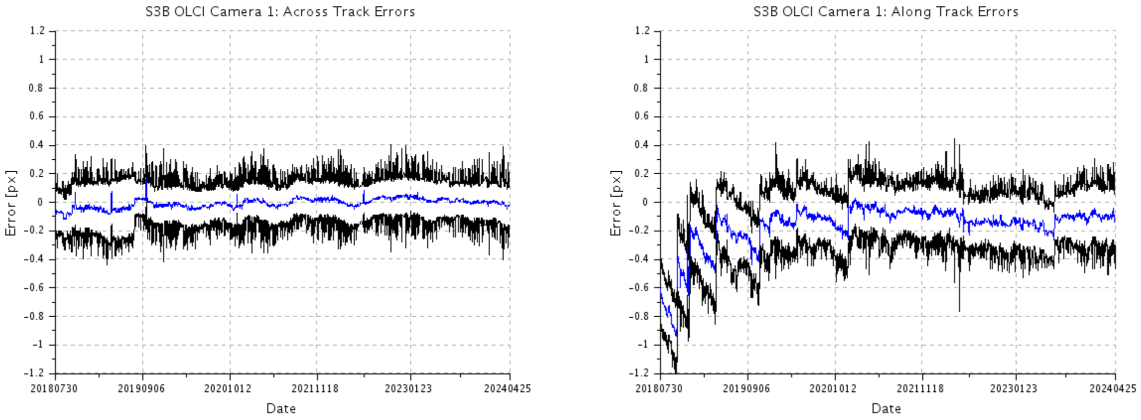

Figure 53: across-track (left) and along-track (right) OLCI-B georeferencing biases time series for Camera 1.

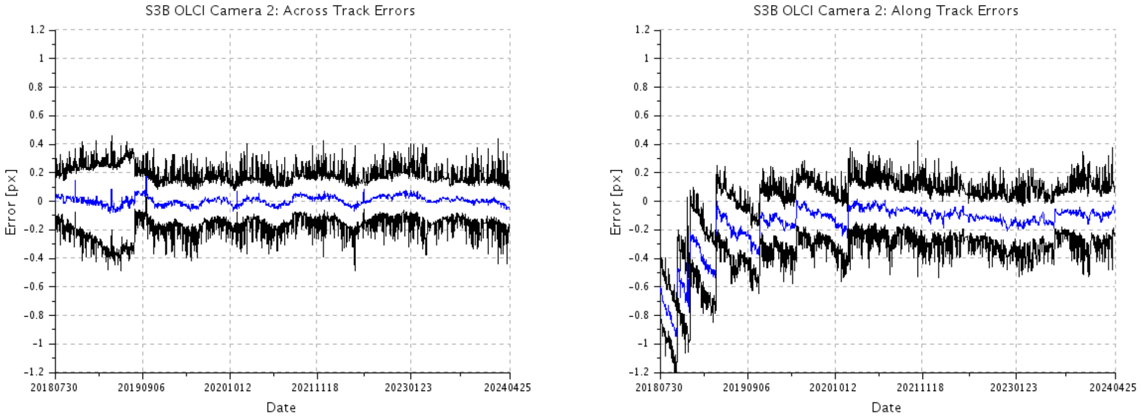

Figure 54: same as Figure 53 for Camera 2.

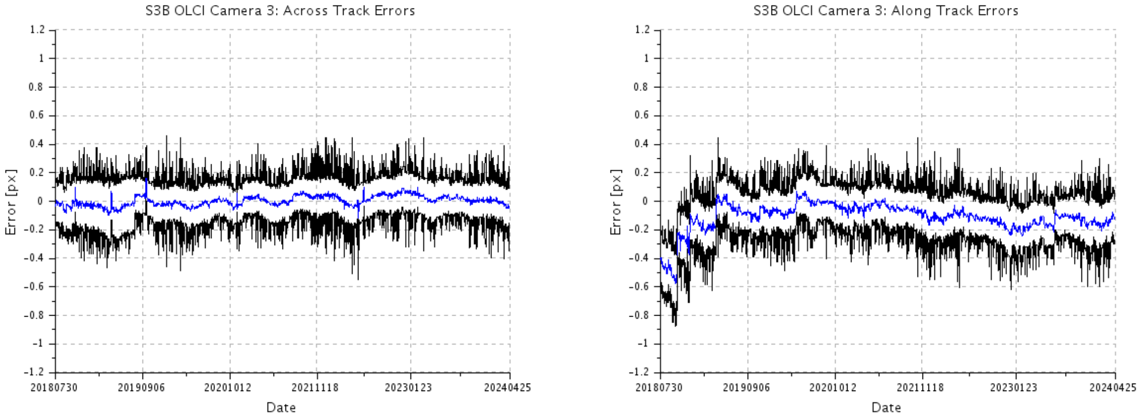

Figure 55: same as Figure 53 for Camera 3.

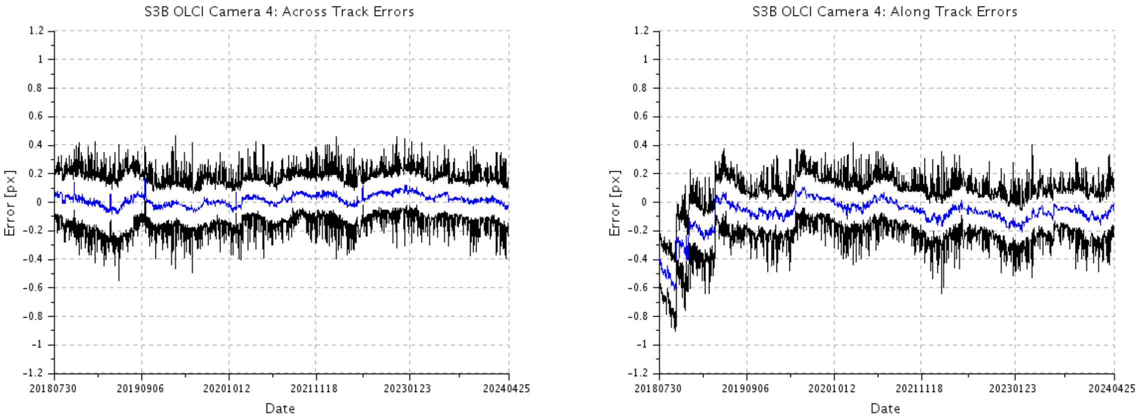

Figure 56: same as Figure 53 for Camera 4.

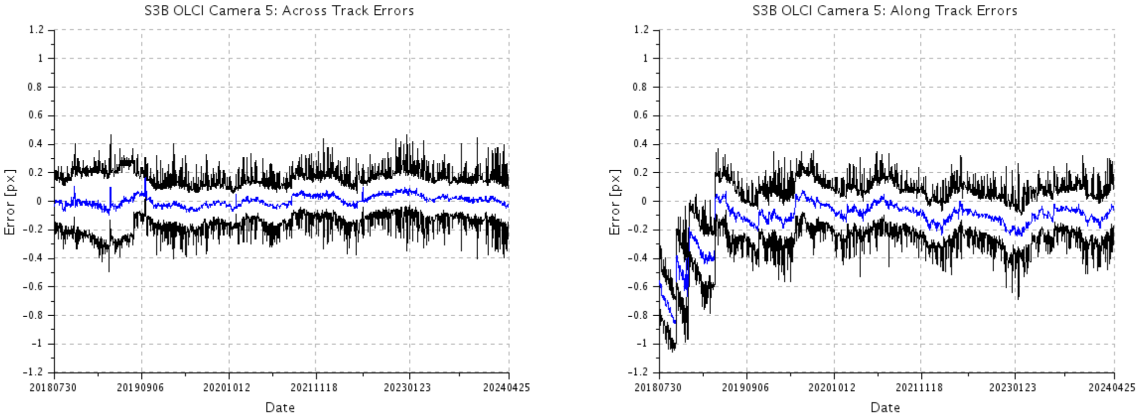

Figure 57: same as Figure 53 for Camera 5.

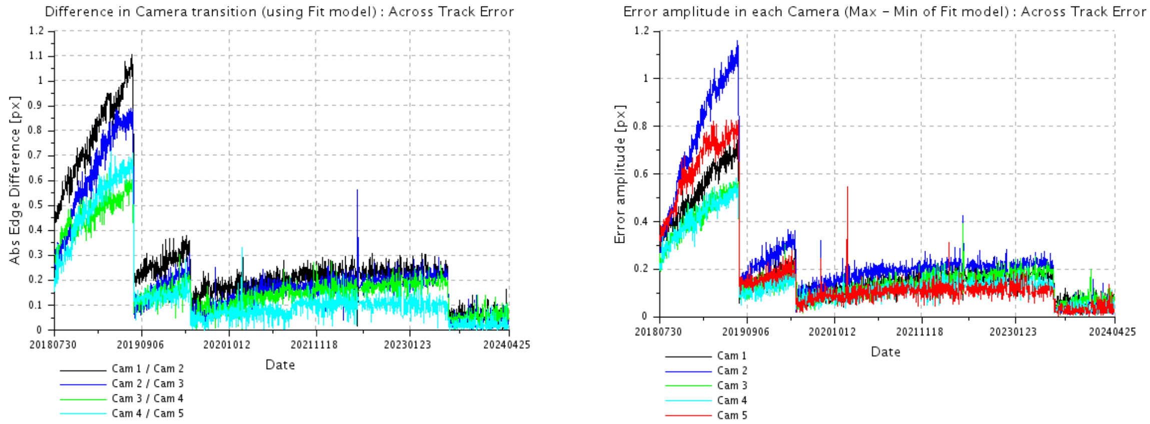

Figure 58: OLCI-B spatial across-track misregistration at each camera transition (left) and maximum amplitude of the across-track error within each camera (left).

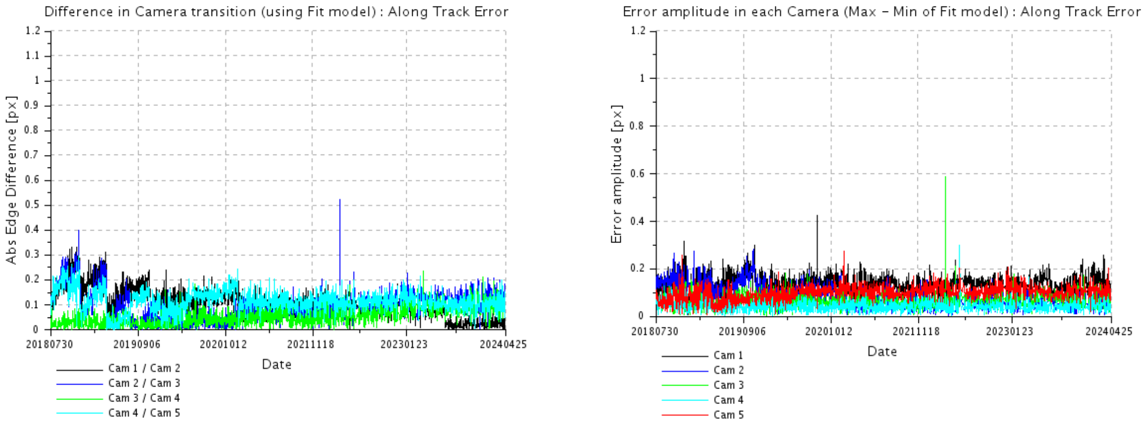

Figure 59: OLCI-B spatial along-track misregistration at each camera transition (left) and maximum amplitude of the along-track error within each camera (left).

3 OLCI Level 1 Product validation

3.1 [OLCI-L1B-CV-300], [OLCI-L1B-CV-310] – Radiometric Validation

3.1.1 S3ETRAC Service

Activities done

The S3ETRAC service extracts OLCI L1 RR and SLSTR L1 RBT data and computes associated statistics over 49 sites corresponding to different surface types (desert, snow, ocean maximizing Rayleigh signal, ocean maximizing sunglint scattering and deep convective clouds). The S3ETRAC products are used for the assessment and monitoring of the L1 radiometry (optical channels) by the ESLs.

All details about the S3ETRAC/OLCI and S3ETRAC/SLSTR statistics are provided on the S3ETRAC website https://s3etrac.acri-st.fr/statistics.

- Number of OLCI products processed by the S3ETRAC service
- Statistics per type of target (DESERT, SNOW, RAYLEIGH, SUNGLINT and DCC)
- Statistics per sites
- Statistics on the number of records

For illustration, we provide below statistics on the number of S3ETRAC/OLCI records generated per type of targets (DESERT, SNOW, RAYLEIGH, SUNGLINT and DCC) for both OLCI-A (Figure 60) and OLCI-B (Figure 61).

Figure 60: summary of S3ETRAC products generation for OLCI-A (number of OLCI-A L1 products Ingested, blue – number of S3ETRAC extracted products generated, green – number of S3ETRAC runs without generation of output product (data not meeting selection requirements), yellow – number of runs ending in error, red, one plot per site type).

Figure 61: summary of S3ETRAC products generation for OLCI-B (number of OLCI-B L1 products Ingested, blue – number of S3ETRAC extracted products generated, green – number of S3ETRAC runs without generation of output product (data not meeting selection requirements), yellow – number of runs ending in error, red, one plot per site type).

3.1.2 Radiometric validation with DIMITRI

OLCI-A and OLCI-B L1B radiometry verification has been processed as follow:

- The verification is performed over Desert-sites **until end-April 2024.**
- The verification is performed over Ocean-sites **until end-April 2024.**
- All results from OLCI-A and OLCI-B over Rayleigh, Glint and PICS are consistent with the previous reporting period over the used CalVal sites.
- Good stability of both sensors OLCI-A and OLCI-B could be observed, nevertheless the time-series average shows higher reflectance from OLCI-A.
- Bands with high gaseous absorption are excluded.

3.1.2.1 Verification and Validation over PICS

1. The ingestion of all the available L1B-LN1-NT products from OLCI-A and OLCI-B over the 6 desert CalVal-sites (Algeria3 & 5, Libya 1 & 4 and Mauritania 1 & 2) has been performed **until end-April 2024**.
2. The results are consistent over all the six used PICS sites (Figure 62 and Figure 63). Both sensors show a good stability over the analysed period.
3. The temporal average over the period **January**-**April 2024** of the elementary ratios (observed reflectance to the simulated one) for **OLCI-A** shows gain values between 2-4% over all the VNIR bands (Figure 64). Unlikely, the temporal average over the same period of the elementary ratios for **OLCI-B** shows gain values within 2% (mission requirements) over the VNIR spectral range (Figure 64). The spectral bands with significant absorption from water vapor and O_2 (Oa11, Oa13, Oa14, Oa15 and Oa20) are excluded.

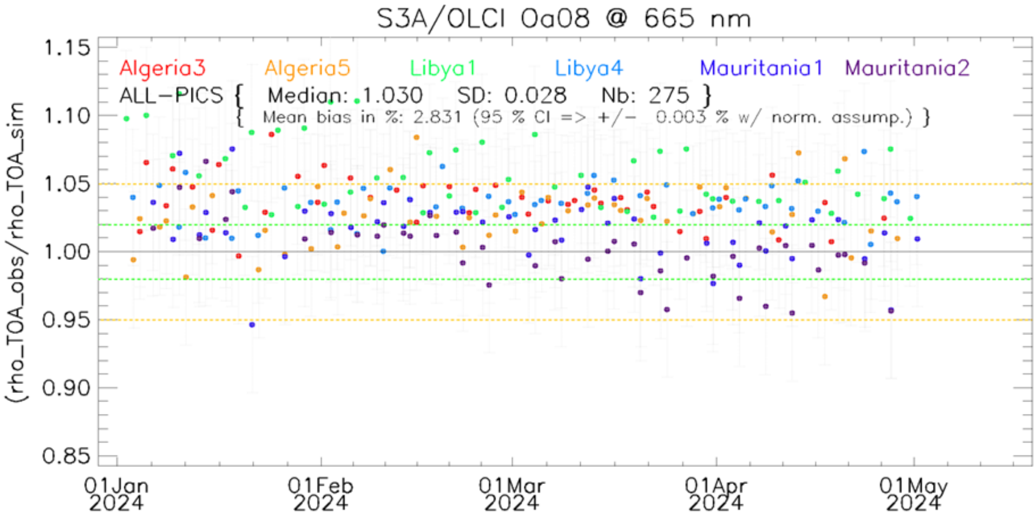

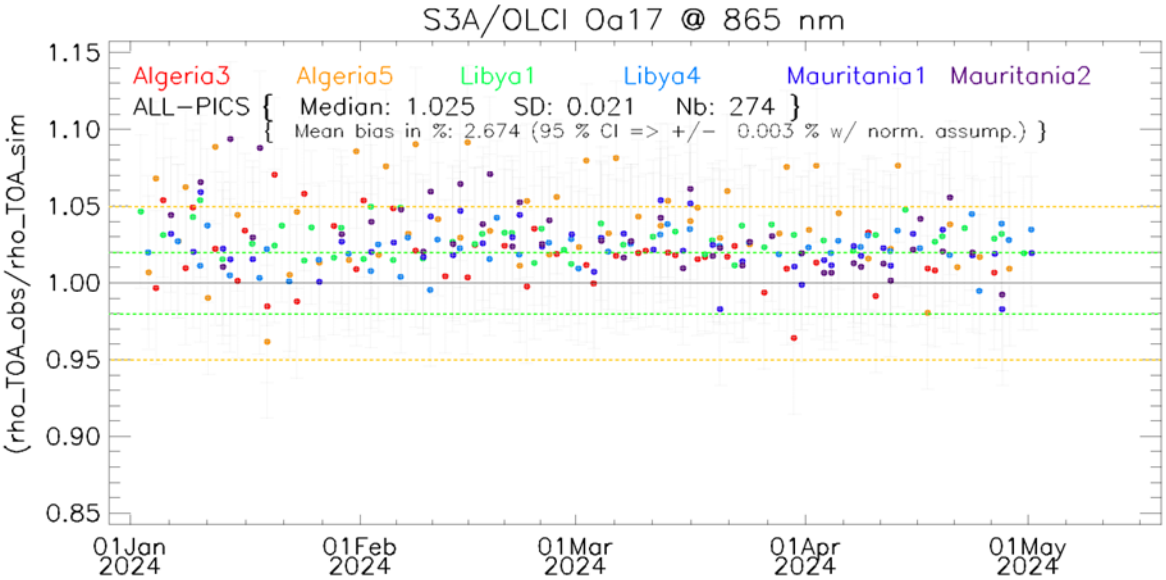

Figure 62: Time-series of the elementary ratios (observed/simulated) signal from OLCI-A for (top to bottom) bands Oa03 and Oa17 respectively over January-April 2024 from the six PICS Cal/Val sites. Dashed-green and orange lines indicate the 2% and 5% respectively. Desert methodology uncertainty is 5%.

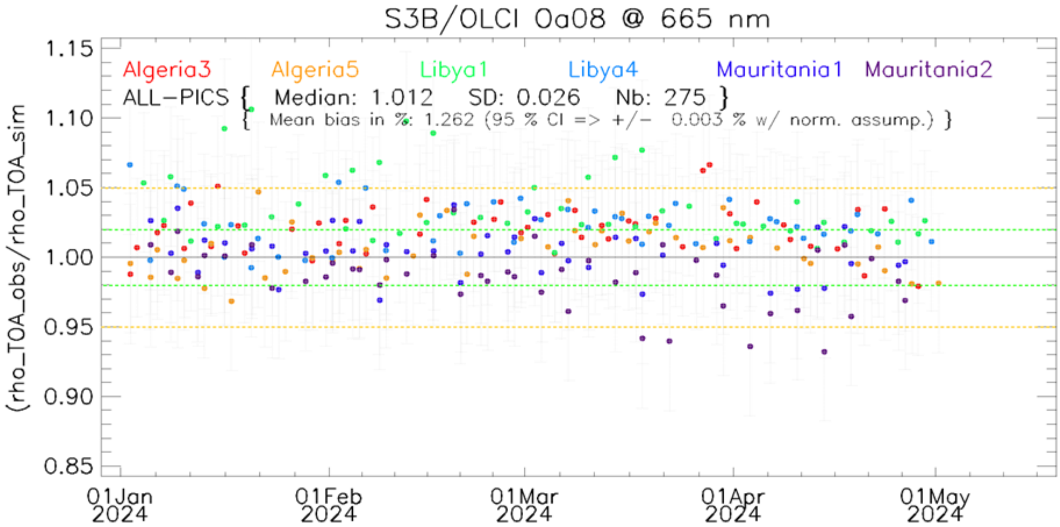

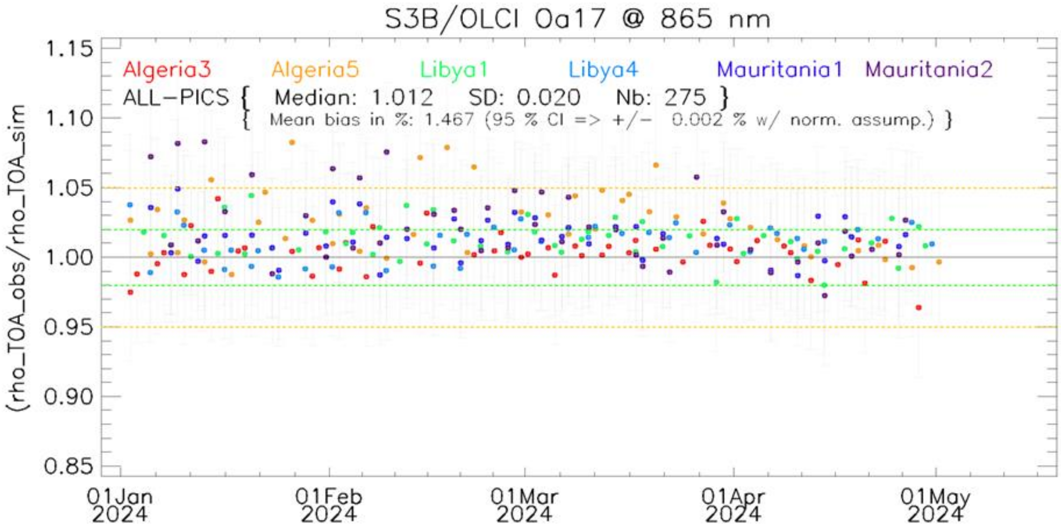

Figure 63: Time-series of the elementary ratios (observed/simulated) signal from OLCI-B for (top to bottom) bands Oa08 and Oa17 respectively over January-April 2024 from the six PICS Cal/Val sites. Dashed-green and orange lines indicate the 2% and 5% respectively. Desert methodology uncertainty is 5%.

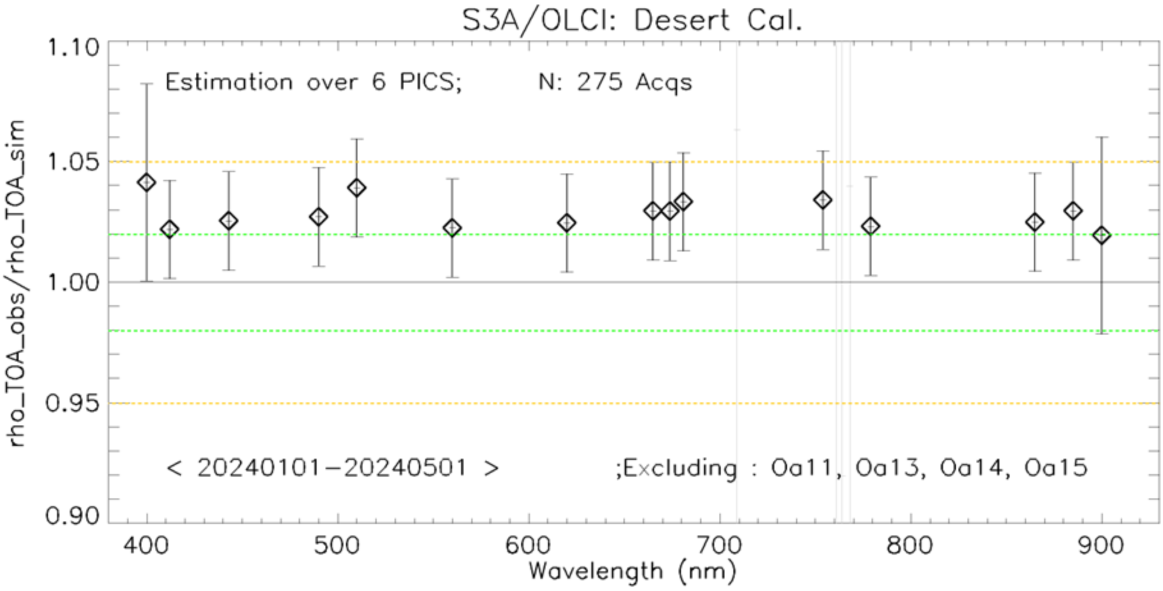

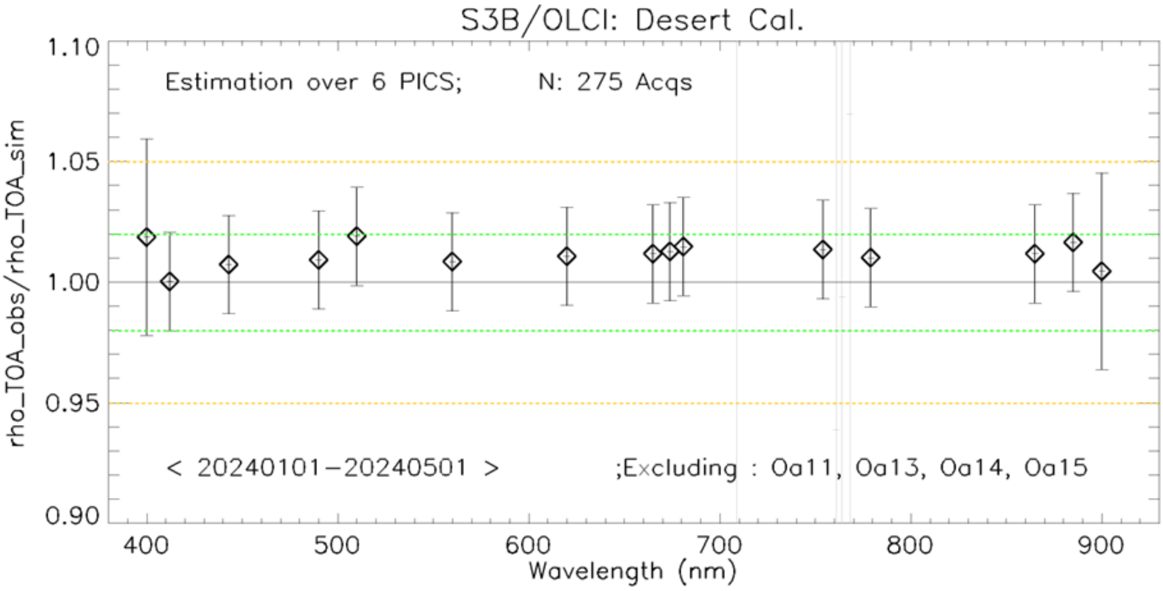

Figure 64: The estimated gain values for OLCI-A and OLCI-B over the 6 PICS sites identified by CEOS over the period January-April 2024 as a function of wavelength. Dashed-green and orange lines indicate the 2% and 5% respectively. Error bars indicate the desert methodology uncertainty.

3.1.2.2 Validation over Rayleigh

Rayleigh method has been performed from the available mini-files over the period **January 2023 - End April 2024** for OLCI-A and OLCI-B. The results were produced with the configuration (ROI-AVERAGE). The gain coefficients of OLCI-A are consistent with the previous results. Bands Oa01-Oa05 display biases values between 3%-5% while bands Oa06-Oa09 exhibit biases about 2%, just within the mission requirement (Figure 65). The gain coefficients of OLCI-B are lower than OLCI-A ones, where bands Oa01-Oa05 display biases values about 2-5%, when bands Oa6-Oa9 exhibit biases around the 2% mission requirement (Figure 65).

3.1.2.3 Validation over Glint and synthesis

Glint calibration method has been performed over the period **January 2023- End April 2024**for OLCI-A and OLCI-B. The outcome of this analysis shows a good consistency with the desert and Rayleigh outputs over the NIR spectral range Oa06-Oa09 for both sensors. Glint results from OLCI-A show that the NIR bands are within 3% (slightly above the 2% mission requirements), except Oa21 which shows higher biases of about 7% and 5% for both sensors respectively (see Figure 65). Again, the glint gain from OLCI-B looks slightly lower than OLCI-A one with most bands within the 2% mission requirement if ignoring the Rayleigh results in the blue-green region and Oa21.

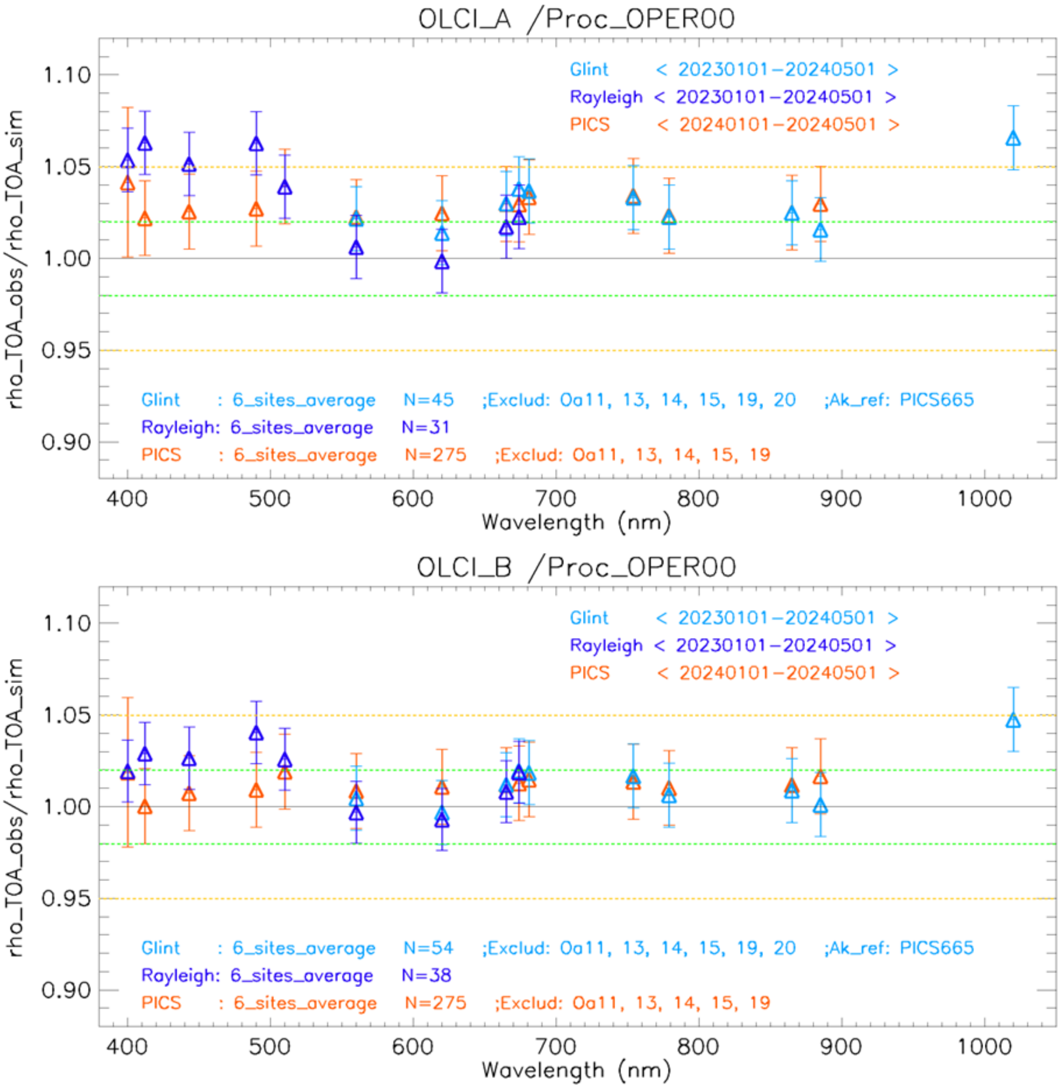

Figure 65: The estimated gain values for OLCI-A and OLCI-B from Glint, Rayleigh and PICS methods over the period January 2023 – end April 2024 and over January- April 2024 (over PICS), as a function of wavelength. We use the gain value of Oa8 from PICS-Desert method as reference gain for Glint method. Dashed-green and orange lines indicate the 2% and 5% respectively. Error bars indicate the method uncertainties.

3.1.2.4 Cross-mission Intercomparison over PICS:

X-mission Intercomparison between MERIS, MSI-A, MSI-B, OLCI-A, OLCI-B, SLSTR-A and SLSTR-B has been performed over the 6 PICS-test-sites.

Figure 66 shows the estimated gain over different time-series for different sensors over PICS. The spectral bands with significant absorption from water vapor and O2 are excluded. OLCI-A seems to have higher gain wrt the other sensors (except SLSTR-A/B), and of about 1-3% higher gain wrt to OLCI-B over VNIR spectral range.

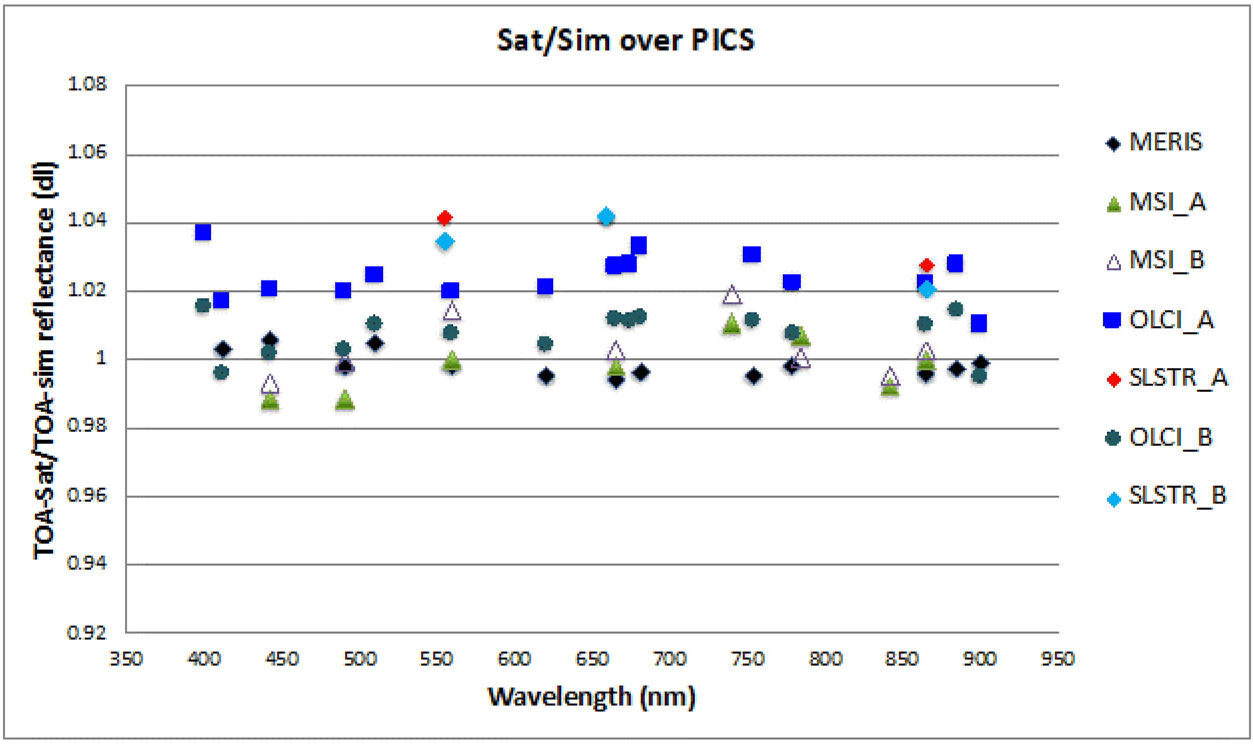

Figure 66: Ratio of observed TOA reflectance to simulated one for (black) MERIS, (pale-green) S2A/MSI, (white) S2B/MSI, (blue) S3A/OLCI, (green) S3B/OLCI, (red) S3A/SLSTR-NADIR, and (cyan) S3B/SLSTR-NADIR averaged over the six PICS test sites over different periods as a function of wavelength.

3.1.3 Radiometric validation with OSCAR

3.1.3.1 OSCAR Rayleigh results

The OSCAR Rayleigh have been applied to the S3A and S3B S3ETRAC data from the 6 oceanic calibration sites (Table 3) using a new chlorophyll climatology which has been derived from the CMEMS OLCI monthly CHL products from considering the years 2017, 2018 and 2019.

Table 3: S3ETRAC Rayleigh Calibration sites

Site Name	Ocean	North Latitude	South Latitude	East Longitude	West Longitude
PacSE	South-East of Pacific	-20.7	-44.9	-89	-130.2
PacNW	North-West of Pacific	22.7	10	165.6	139.5
PacN	North of Pacific	23.5	15	200.6	179.4
AtlN	North of Atlantic	27	17	-44.2	-62.5
AtlS	South of Atlantic	-9.9	-19.9	-11	-32.3
IndS	South of Indian	-21.2	-29.9	100.1	89.5

In Figure 67 the average OSCAR OLCI-A and OLCI-B Rayleigh results are given for April 2024. In Figure 68 and Table 4, the same results are given for all acquisitions of 2024. In the lower wavelengths, OLCI-A remains brighter with respect to OLCI-B.

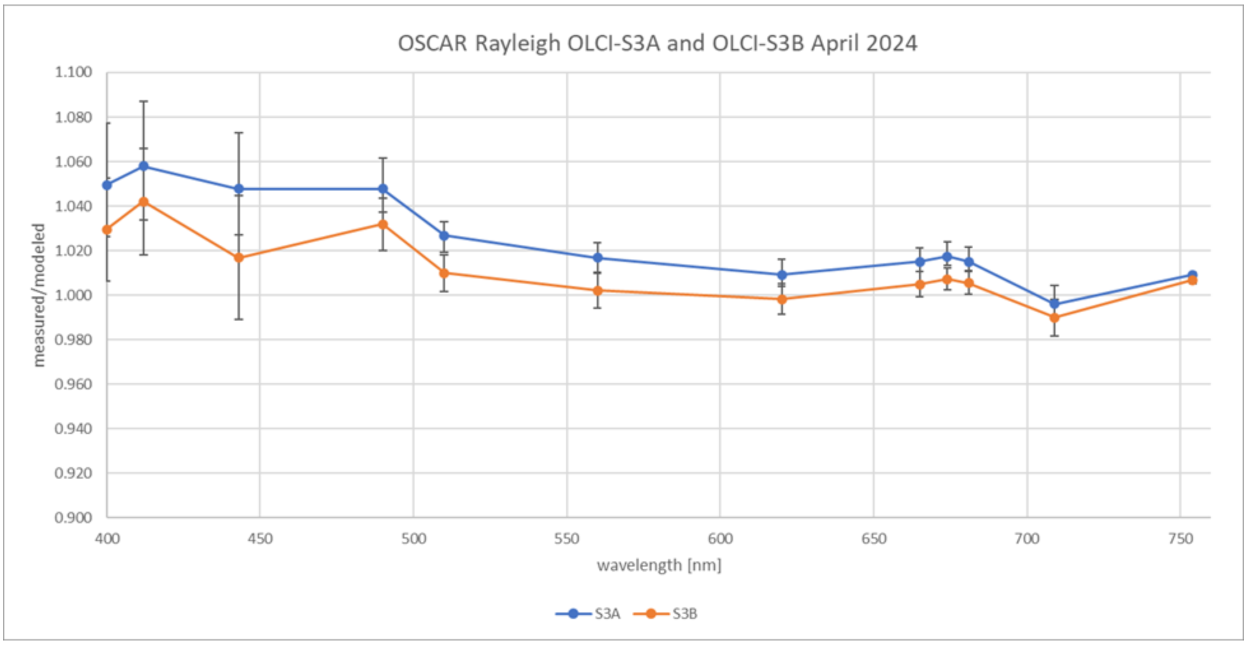

Figure 67: OSCAR Rayleigh S3A and S3B Calibration results as a function of wavelength for April 2024. The results are obtained with a new climatology derived from CMEMS OLCI monthly CHL products.

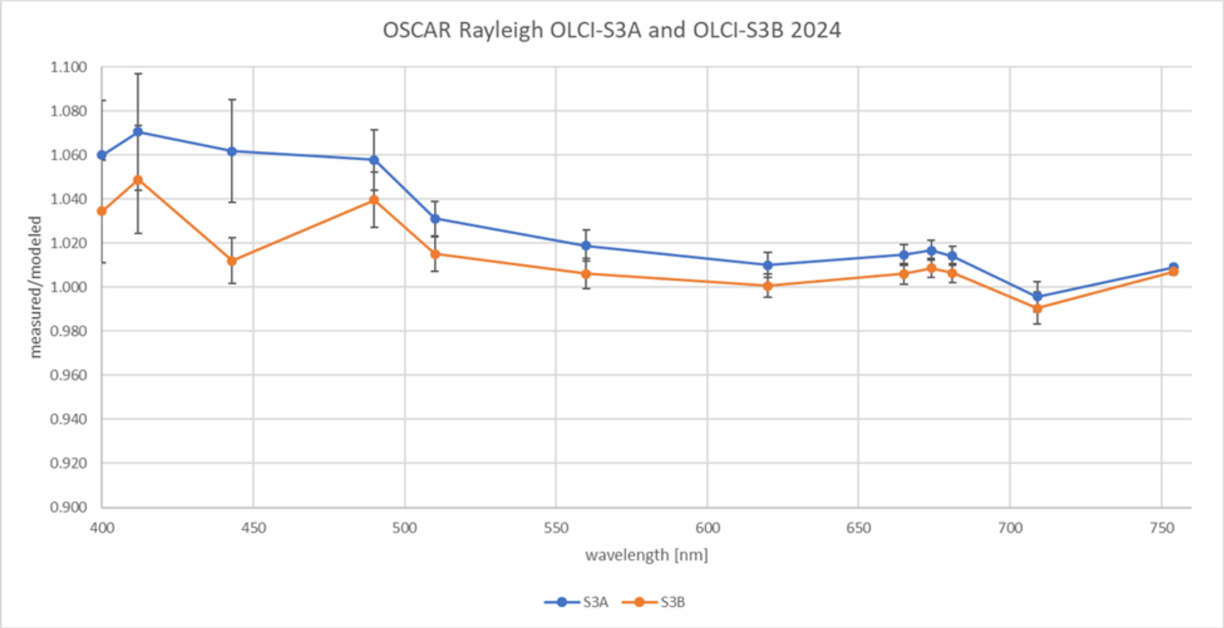

Figure 68: OSCAR Rayleigh OLCI-A and OLCI-B Calibration results as a function of wavelength for all acquisitions of 2024. The results are obtained with a new climatology derived from CMEMS OLCI monthly CHL products.

Table 4. OSCAR Rayleigh calibration results for S3A and S3B (average and standard deviation over all 2024 acquisitions) over all scenes currently (re)processed with the new climatology and observed difference (in %) between OLCIA and OLCIB

OLCI band	Wavelength (nm)	Oscar Rayleigh OLCIA avg	Oscar Rayleigh OLCIA stdev	Oscar Rayleigh OLCIB avg	Oscar Rayleigh OLCIB stdev	% difference OLCIA and OLCIB
Oa01	400	1.060	0.025	1.035	0.023	2.39%
Oa02	412	1.070	0.026	1.049	0.024	2.02%
Oa03	443	1.062	0.023	1.012	0.010	4.69%
Oa04	490	1.058	0.014	1.040	0.013	1.71%
Oa05	510	1.031	0.008	1.015	0.008	1.55%
Oa06	560	1.019	0.007	1.006	0.007	1.25%
Oa07	620	1.010	0.006	1.001	0.005	0.93%
Oa08	665	1.015	0.005	1.006	0.005	0.85%
Oa09	674	1.017	0.004	1.009	0.004	0.78%
Oa10	681	1.014	0.004	1.007	0.004	0.75%
Oa11	709	0.996	0.007	0.990	0.007	0.52%
Oa12	754	1.009	0.001	1.007	0.001	0.18%

3.1.3.2 OSCAR Glitter results

The OSCAR Glitter have been applied to all S3ETRAC glitter data for April 2024. Both OLCI-A and OLCI-B data was processed. The plots in Figure 69 are the glitter results for OLCI-A and OLCI-B for the period of April 2024 and on Figure 70 for all results of 2024 (also provided in Table 5). The values are in absolute terms, since all bands are referenced to the Rayleigh result of band Oa8. The glitter method is a relative inter-band calibration method, since the Oa8 band is used to estimate windspeed. By multiplying all band results with the Rayleigh calibration factor for the same period, the results are referenced to the results of this method.

For all results of 2024, the difference between OLCI-A and OLCI-B (Table 5, in %) is below 1% for all bands, except for bands Oa04, Oa05 and Oa06. It also indicates a brighter OLCI-A compared to OLCI-B.

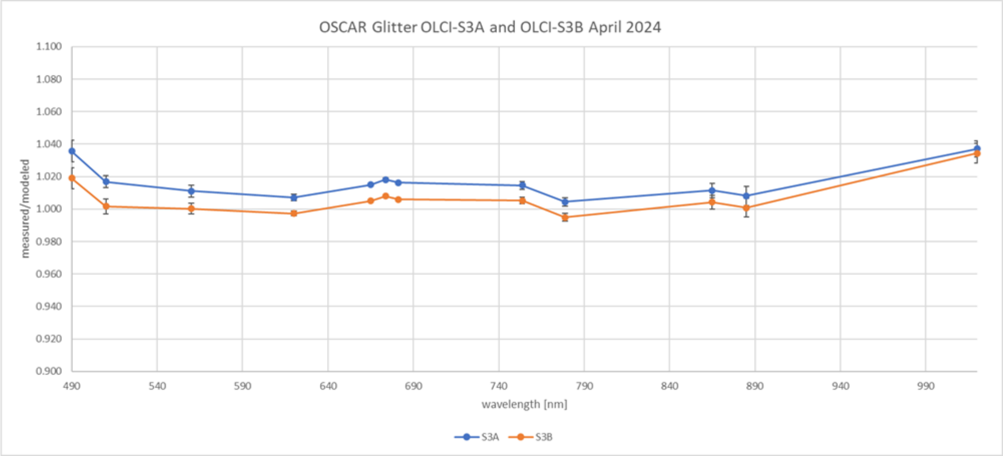

Figure 69: OSCAR Glitter OLCI-A & OLCI-B Calibration results as a function of wavelength for April 2023. The results are obtained with a new climatology derived from CMEMS OLCI monthly CHL products.

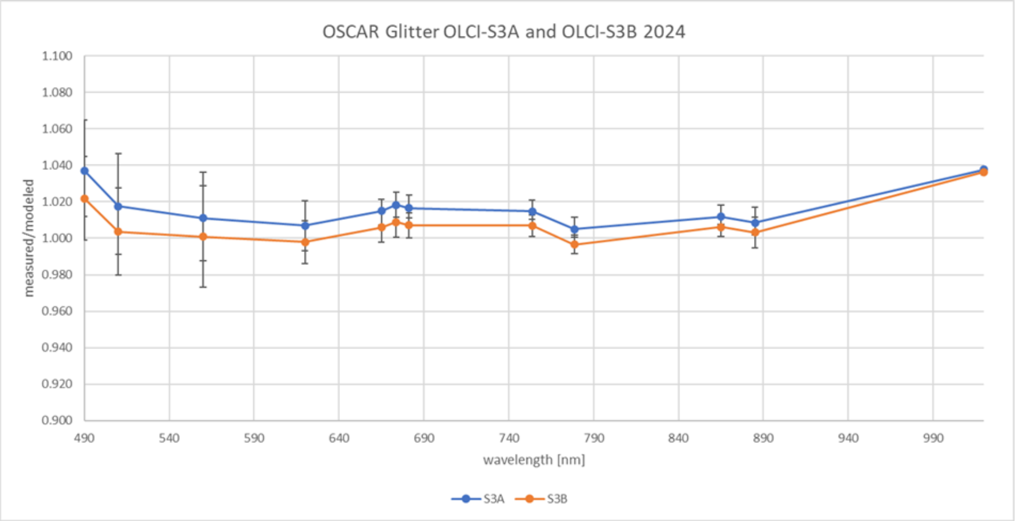

Figure 70: OSCAR Glitter OLCI-A & OLCI-B Calibration results as a function of wavelength for all acquisitions of 2024. The results are obtained with a new climatology derived from CMEMS OLCI monthly CHL products.

Table 5: OSCAR Glitter calibration results for OLCI-A and OLCI-B (average and standard deviation over all acquisitions of 2023) currently processed with the new climatology and observed difference (in %)

OLCI band	Wavelength	Oscar Glitter OLCIA		Oscar Glitter OLCIB		% difference OLCIA and OLCIB
	(nm)	avg	stdev	avg	stdev	
Oa04	490	1.037	0.008	1.022	0.006	1.47%
Oa05	510	1.018	0.005	1.004	0.004	1.37%
Oa06	560	1.011	0.003	1.001	0.003	1.01%
Oa07	620	1.007	0.002	0.998	0.001	0.90%
Oa08	665	1.015	0.000	1.006	0.000	0.89%
Oa09	673.75	1.018	0.001	1.009	0.001	0.92%
Oa10	681.25	1.017	0.001	1.007	0.001	0.93%
Oa12	753.75	1.015	0.002	1.007	0.002	0.79%
Oa16	778.75	1.005	0.003	0.997	0.002	0.83%
Oa17	865	1.012	0.004	1.006	0.004	0.57%
Oa18	885	1.009	0.005	1.003	0.004	0.53%
Oa21	1020	1.038	0.005	1.036	0.005	0.13%

3.1.4 Radiometric validation with Moon observations: LIME results

Comparison between OLCIA/B and the Lunar Irradiance Model of ESA (LIME) is demonstrated in the following section. Table 6 is the list of all processed images currently available through the O-MPC - up to January 2024 for OLCI-A and February 2024 for OLCI-B.

Table 6: List processed S3A&B acquisitions

S3A	PHASE	STATUS	S3B	PHASE	status
13/07/2022	5.63	processed	12/08/2022	6.65	processed
03/07/2023	6.57	processed	04/06/2023	5.21	processed
29/09/2023	6.38	processed	31/08/2023	4.51	processed
27/11/2023	6.65	processed	29/10/2023	4.93	processed
26/01/2024	6.12	processed	28/12/2023	6.47	processed
			24/02/2024	6.16	processed

The results for all acquisitions are shown in Figure 71 for OLCI-A and Figure 72 for OLCI-B. in general, the profile of the results over the wavelengths show a very good agreement for both sensors. The average absolute level for all bands varies between 5% and 10% for OLCI-A and between 3% and 7% for OLCI-B. This is slightly higher than reported in both OSCAR methods, especially for the higher wavelengths, but spectral profiles are smoother, except for the band OA01. The most recent acquisitions added are the oldest ones (both summer 2022) and they have been acquired with a different camera (2) compared to the routine acquisitions of 2023/2024.

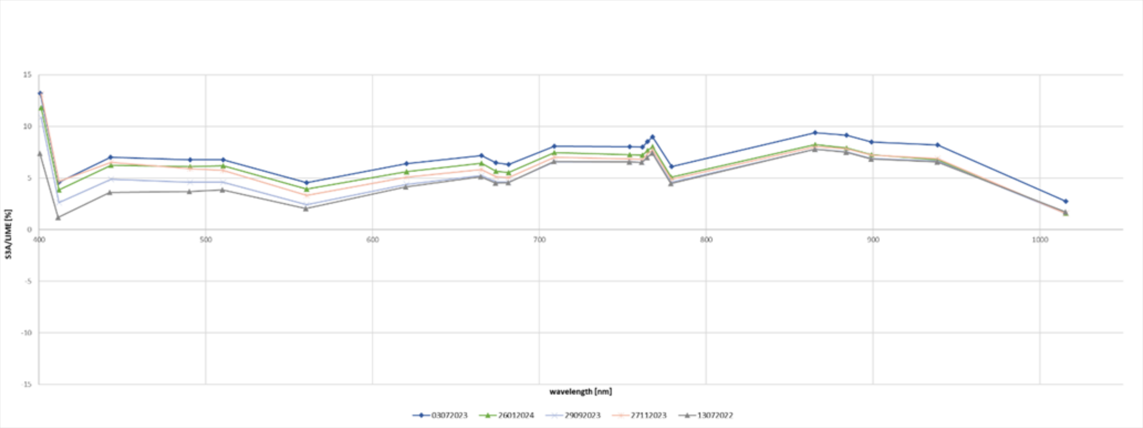

Figure 71: OLCI-A vs LIME for all acquisitions

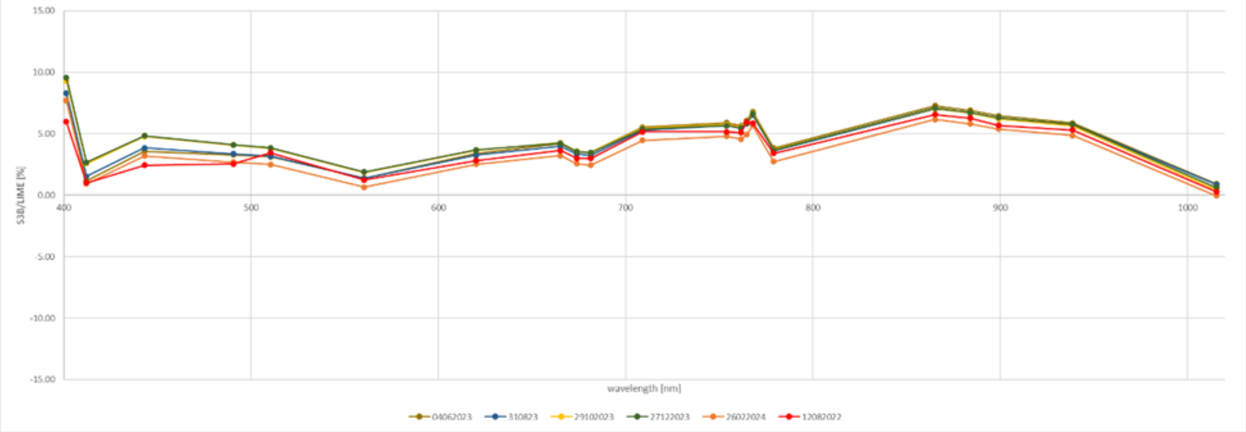

Figure 72: OLCI-B vs LIME for all acquisitions

In Figure 73 the average results of all acquisitions are shown, and it reveals a small stdev (k=1). Figure 74 is the difference between OLCI-A and OLCI-B (%) for all acquisitions. The difference varies between a maximum of 2.92% in the band Oa10 and 0.99% for Oa12 (absorption bands excluded). Detailed figures are tabulated in Table 7.

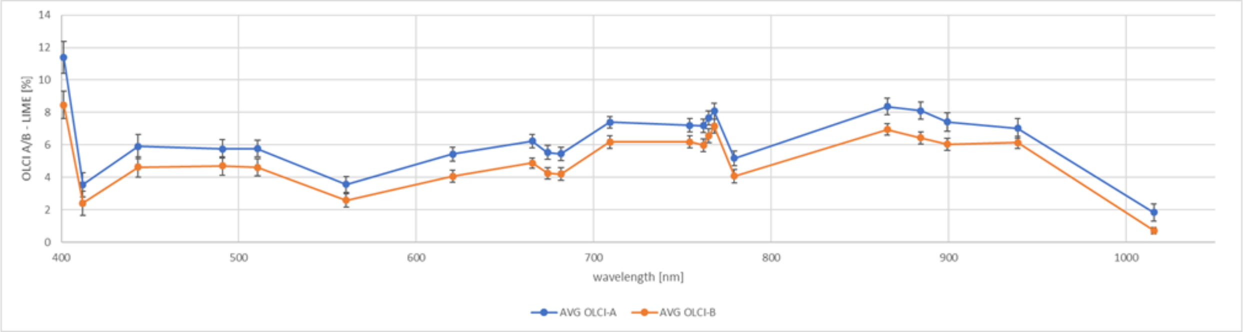

Figure 73. Average comparison between OLCI-A&B against LIME

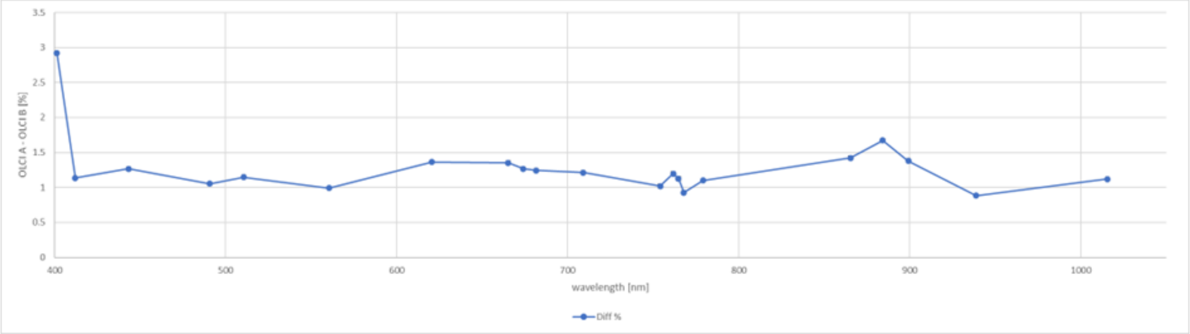

Figure 74. Difference between OLCI A&B compared with LIME

Contrary to the other methods (i.e. OSCAR), band Oa21 shows absolute levels that are lower than overall average band levels. The reason is unknown but could possibly be attributed to the LIME interpolation for SWIR bands. Currently an update of the model is being established to mitigate the model levels in the SWIR due to linear regression.

The discrepancy of 3.54% between both Oa01 bands seems exaggerated. It might be caused by the limited number of acquisitions considered for the lunar results of O-MPC (4 and 5 resp.). This will be monitored and investigated further with new measurements and (eventual) reprocessing the current ones.

Table 7: LIME calibration results for OLCI-A and OLCI-B (average and standard deviation over all acquisitions) observed difference (in %).

OLCI band	Wavelength (nm)	LIME OLCIA		LIME OLCIB		% difference OLCIA and OLCIB
		avg	stdev	avg	stdev	
Oa01	400	1.114	0.010	1.085	0.008	2.92%
Oa02	412.5	1.035	0.007	1.024	0.008	1.14%
Oa03	442.5	1.059	0.007	1.046	0.006	1.27%
Oa04	490	1.058	0.006	1.047	0.006	1.05%
Oa05	510	1.058	0.005	1.046	0.005	1.15%
Oa06	560	1.036	0.005	1.026	0.004	0.99%
Oa07	620	1.054	0.004	1.041	0.004	1.36%
Oa08	665	1.062	0.004	1.049	0.003	1.35%
Oa09	673.75	1.055	0.004	1.043	0.004	1.27%
Oa10	681.25	1.054	0.004	1.042	0.004	1.24%
Oa11	708.75	1.074	0.003	1.062	0.004	1.21%
Oa12	753.75	1.072	0.004	1.062	0.004	1.02%
Oa13	761.25	1.072	0.004	1.060	0.004	1.20%
Oa14	764.375	1.077	0.004	1.065	0.004	1.13%
Oa15	767.5	1.081	0.005	1.072	0.004	0.93%
Oa16	778.75	1.052	0.005	1.041	0.004	1.10%
Oa17	865	1.084	0.005	1.069	0.004	1.42%
Oa18	885	1.081	0.005	1.064	0.004	1.67%
Oa19	900	1.074	0.006	1.060	0.004	1.38%
Oa20	940	1.070	0.006	1.061	0.004	0.88%
Oa21	1020	1.018	0.005	1.007	0.002	1.12%

4 Level 2 Land products validation

4.1 [OLCI-L2LRF-CV-300]

4.1.1 Routine extractions

- The focus for this time period has been on the rolling archive Non Time Critical (NT) data until the 31st of December 2023. More data available for statistical analysis as a concatenation procedure for all available data in the MERMAID processing has been implemented.
- Concatenated time series of OLCI Global Vegetation Index and OLCI Terrestrial Chlorophyll Index have been regenerated on the current rolling archive availability including previous extractions since June 2016 and April 2018 for S3A and S3B respectively.

4.1.1.1 OLCI-A

Figure 75 to Figure 84 below present the Core Land Sites OLCI-A time series over the current period.

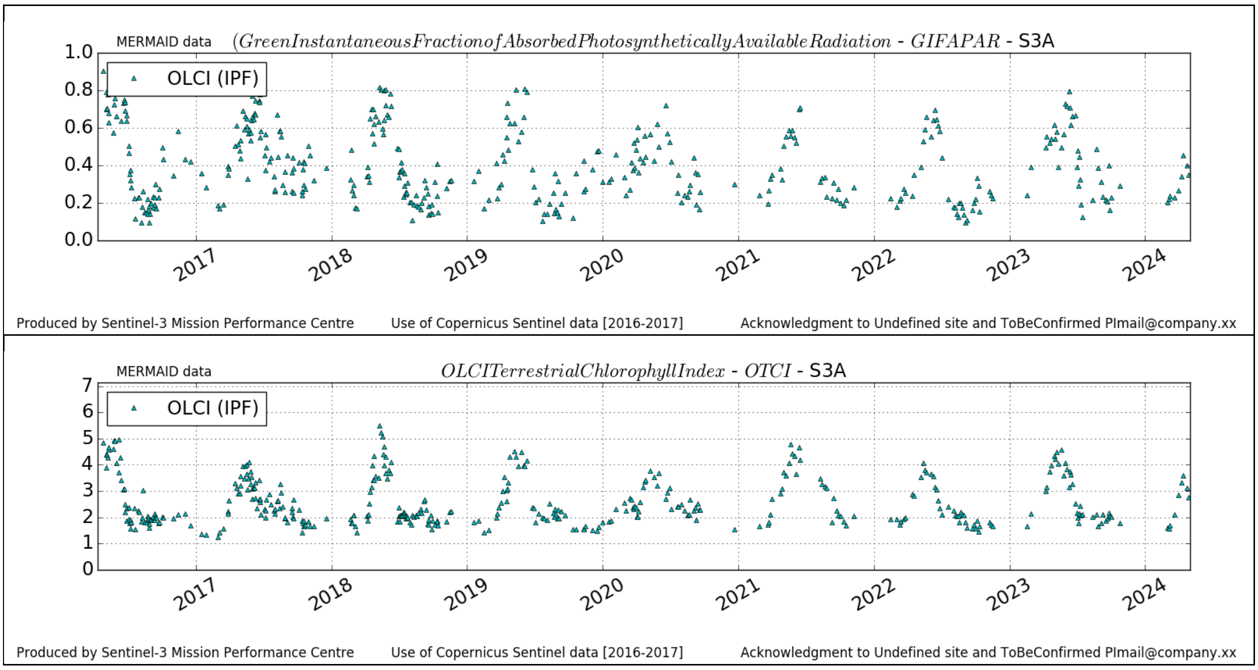

Figure 75: DeGeb time series over current report period

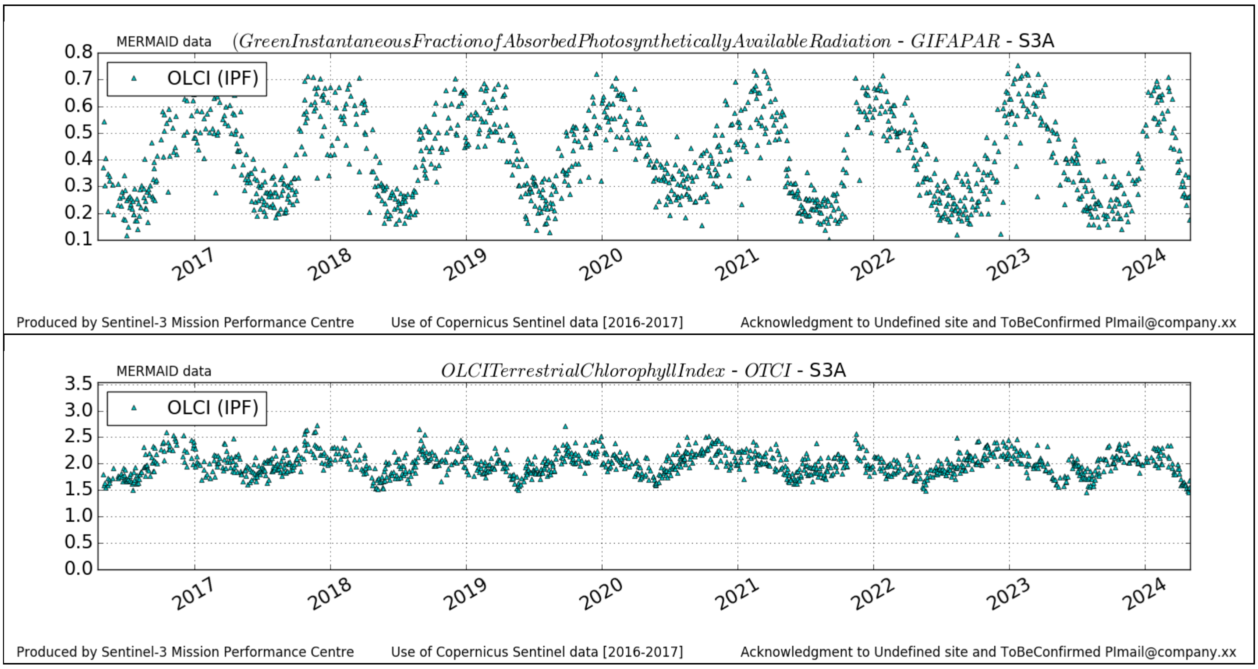

Figure 76: ITCat time series over current report period

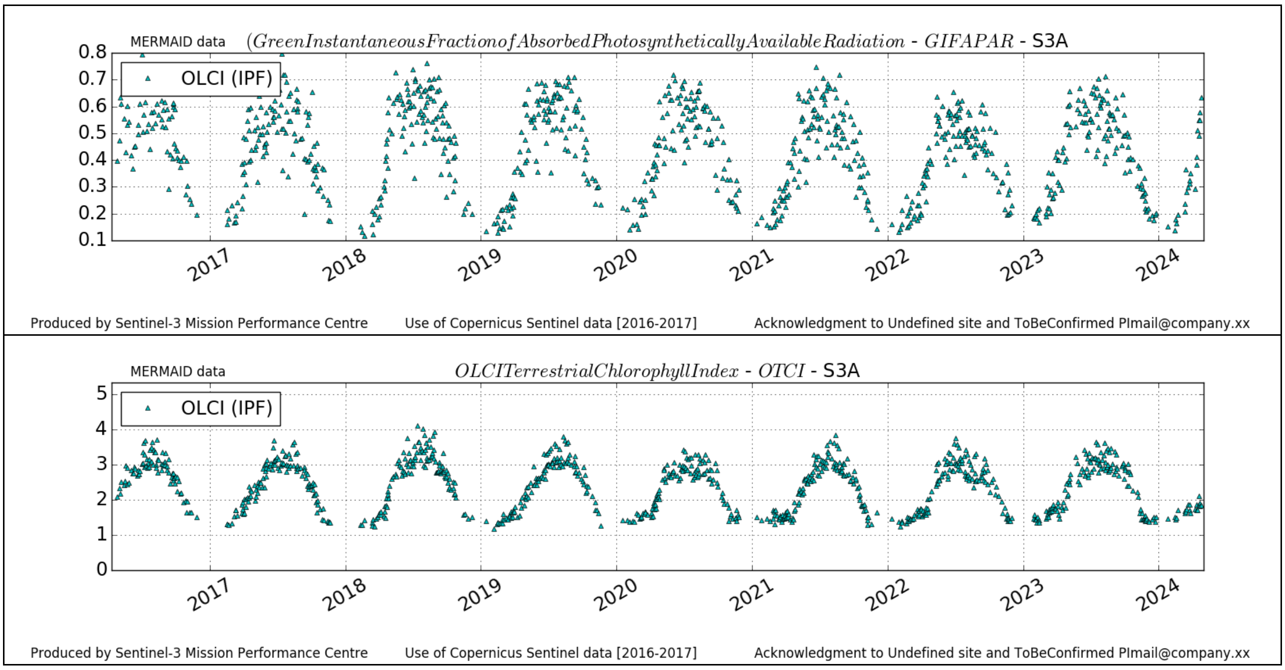

Figure 77: ITIsp time series over current report period

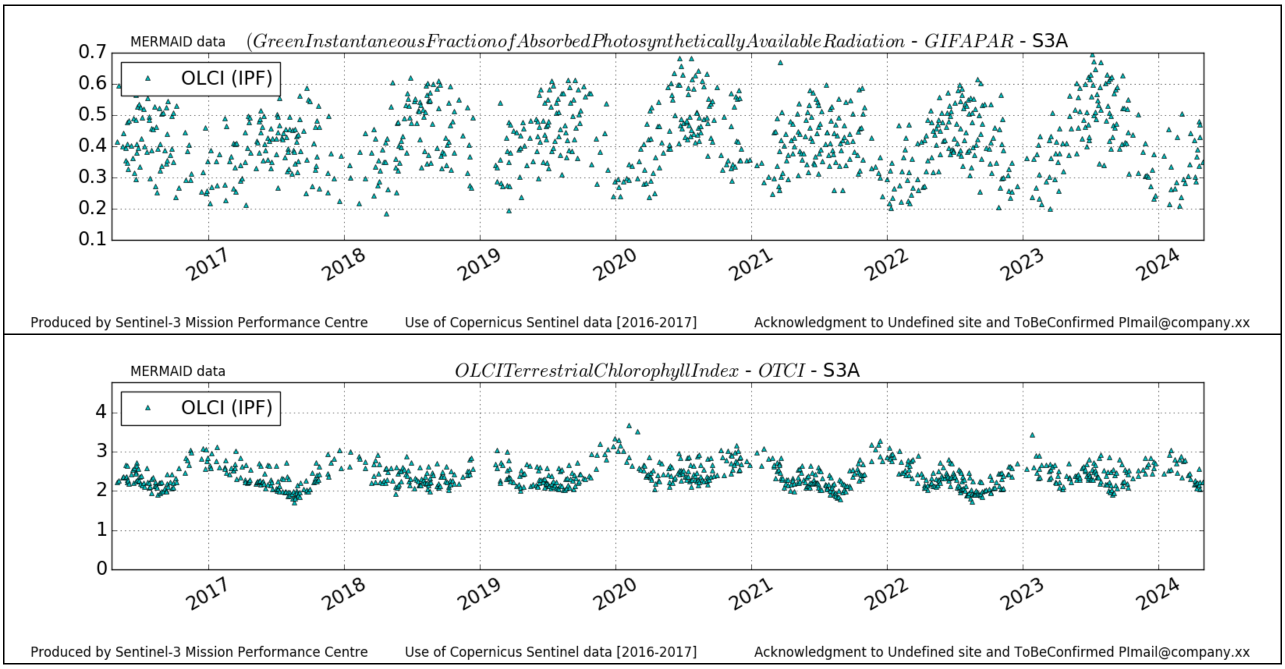

Figure 78: ITSro time series over current report period

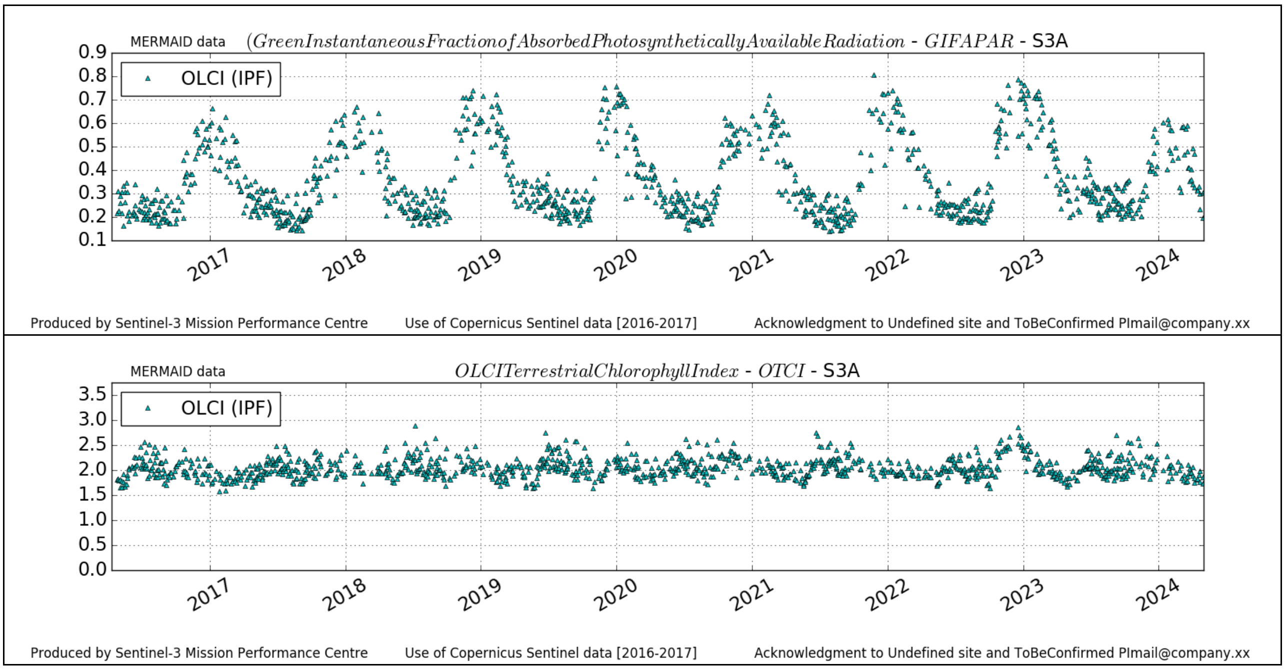

Figure 79: ITTra time series over current report period

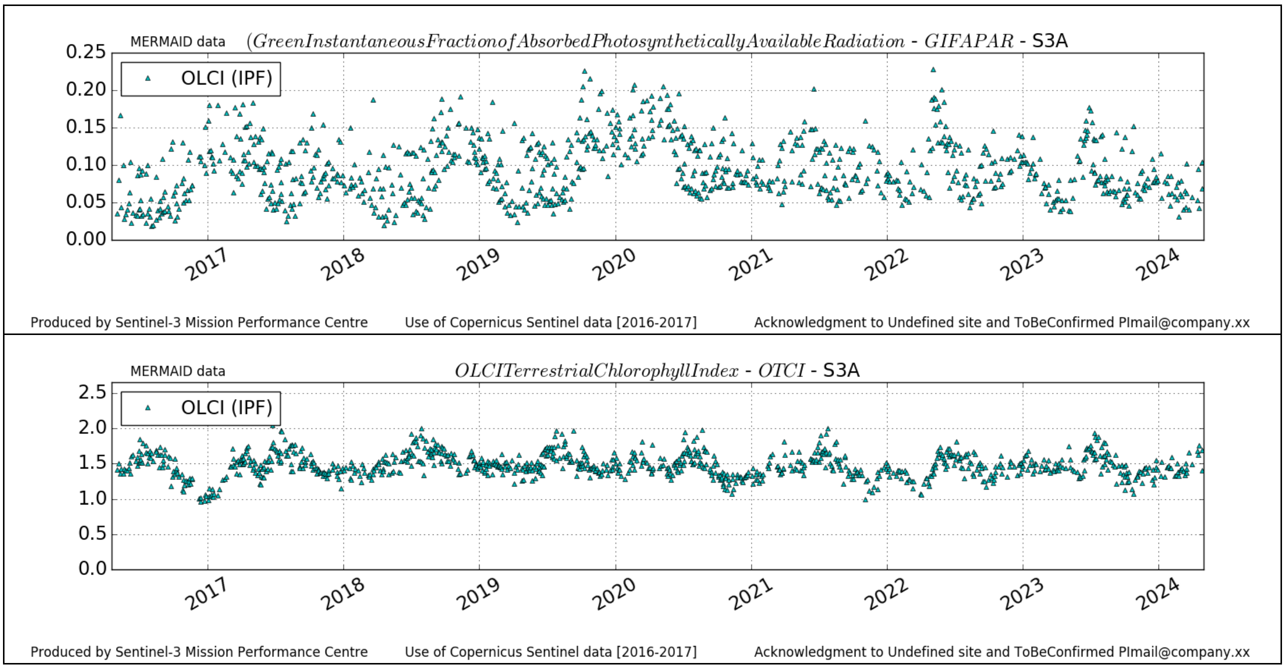

Figure 80: SPAli time series over current report period

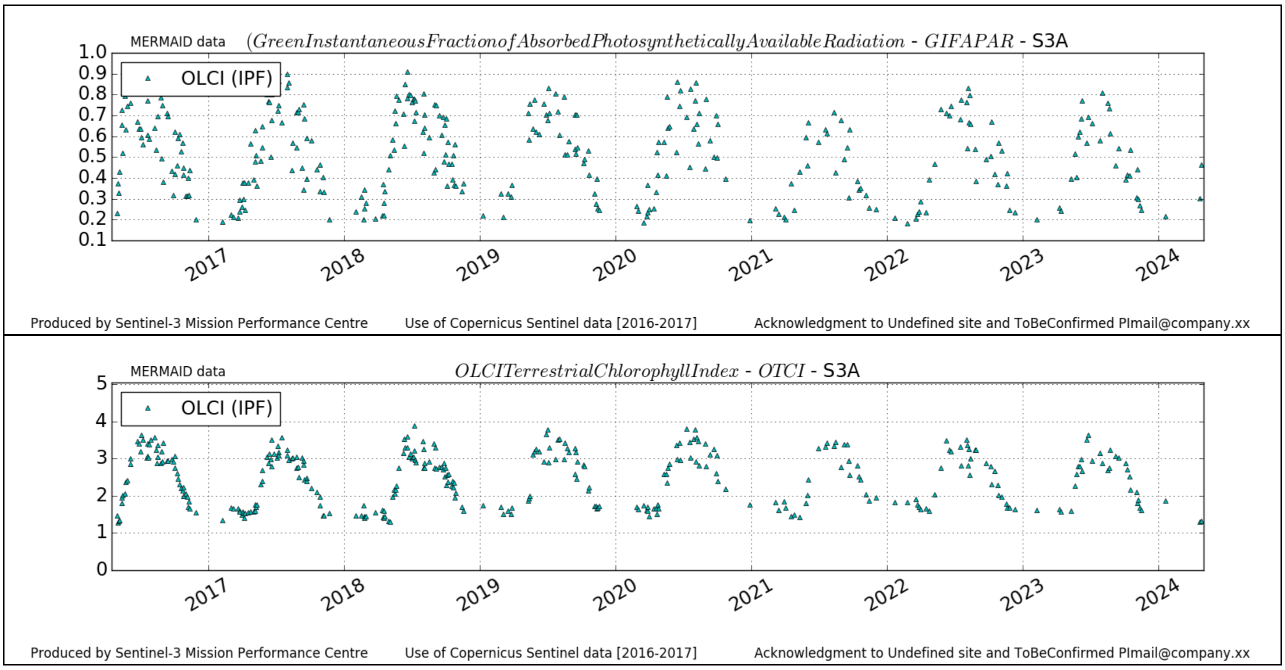

Figure 81: UKNFo time series over current report period

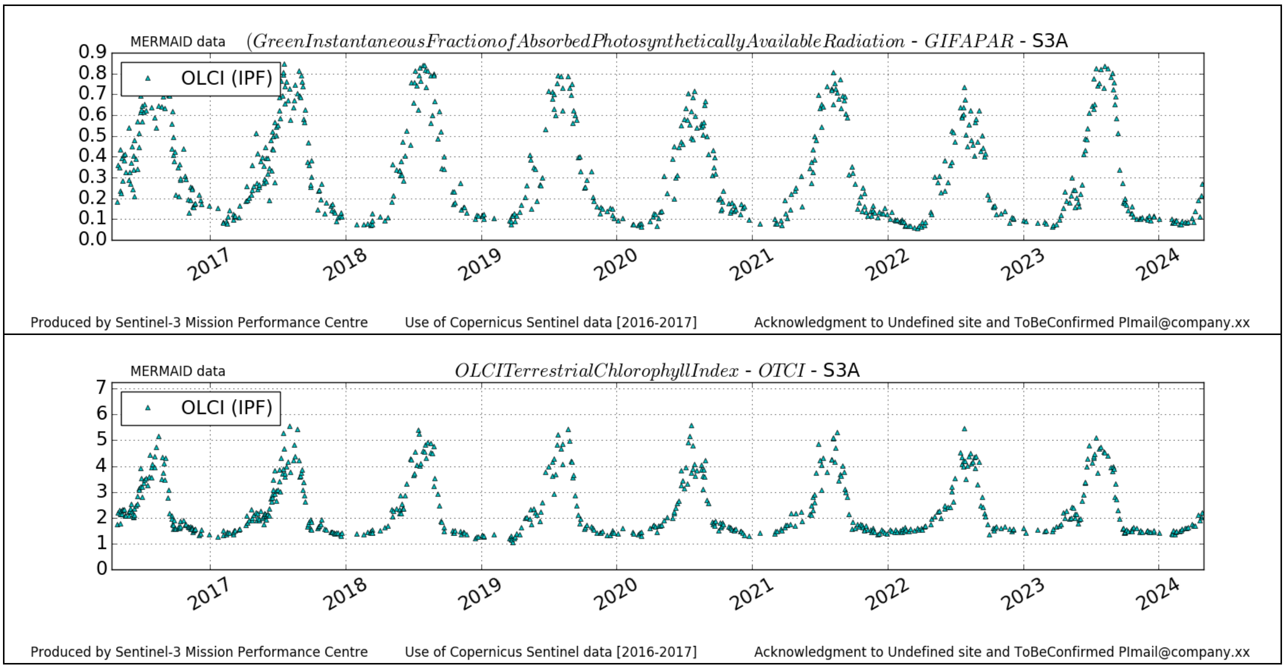

Figure 82: USNe1 time series over current report period

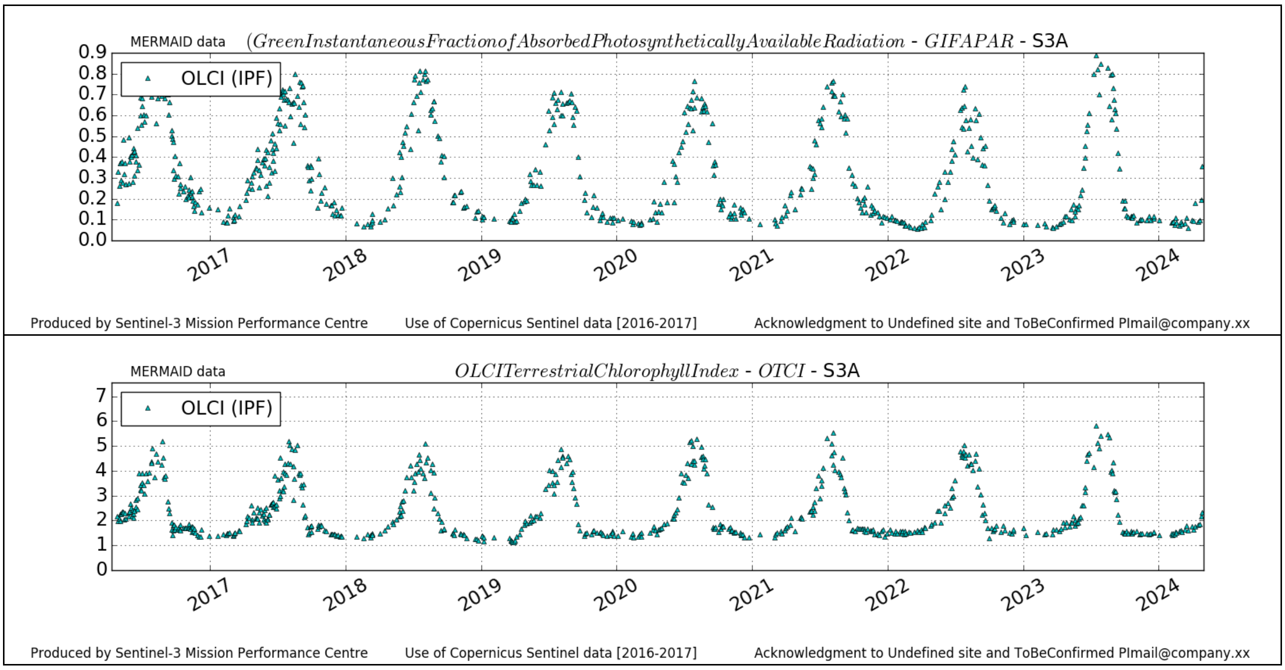

Figure 83: USNe2 time series over current report period

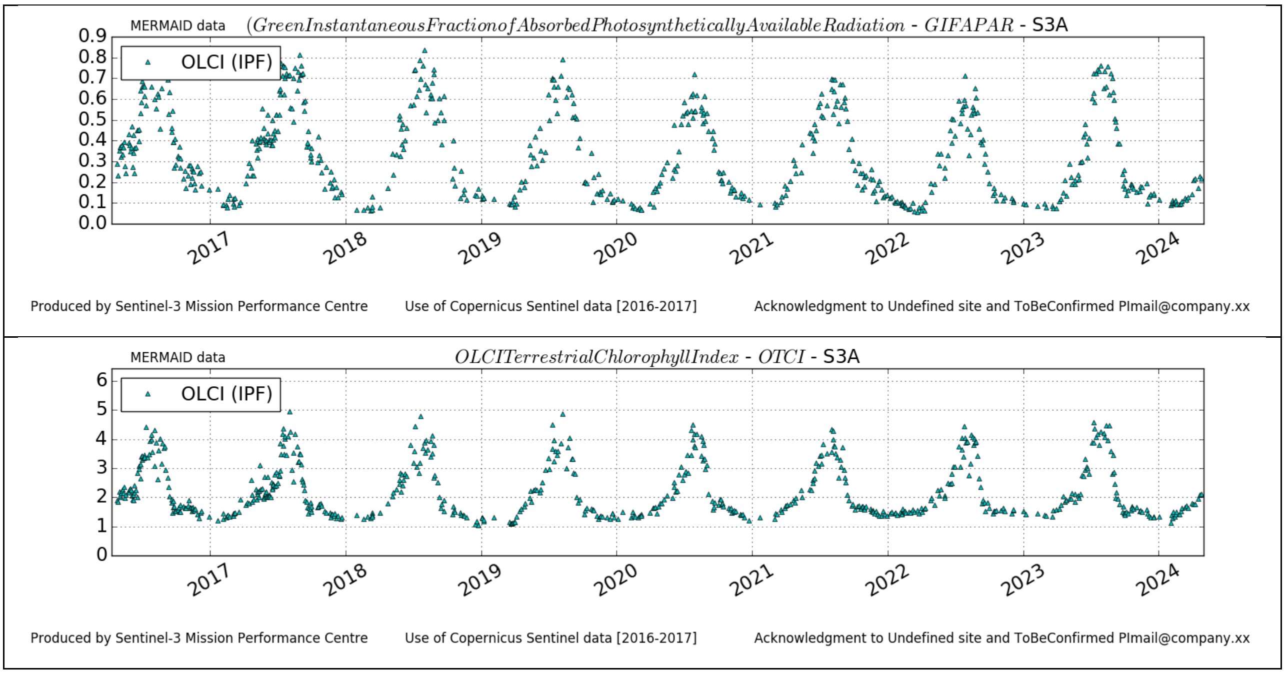

Figure 84: USNe3 time series over current report period

4.1.1.2 OLCI-B

Figure 85 to Figure 94 below present the Core Land Sites OLCI-B time series over the current period.

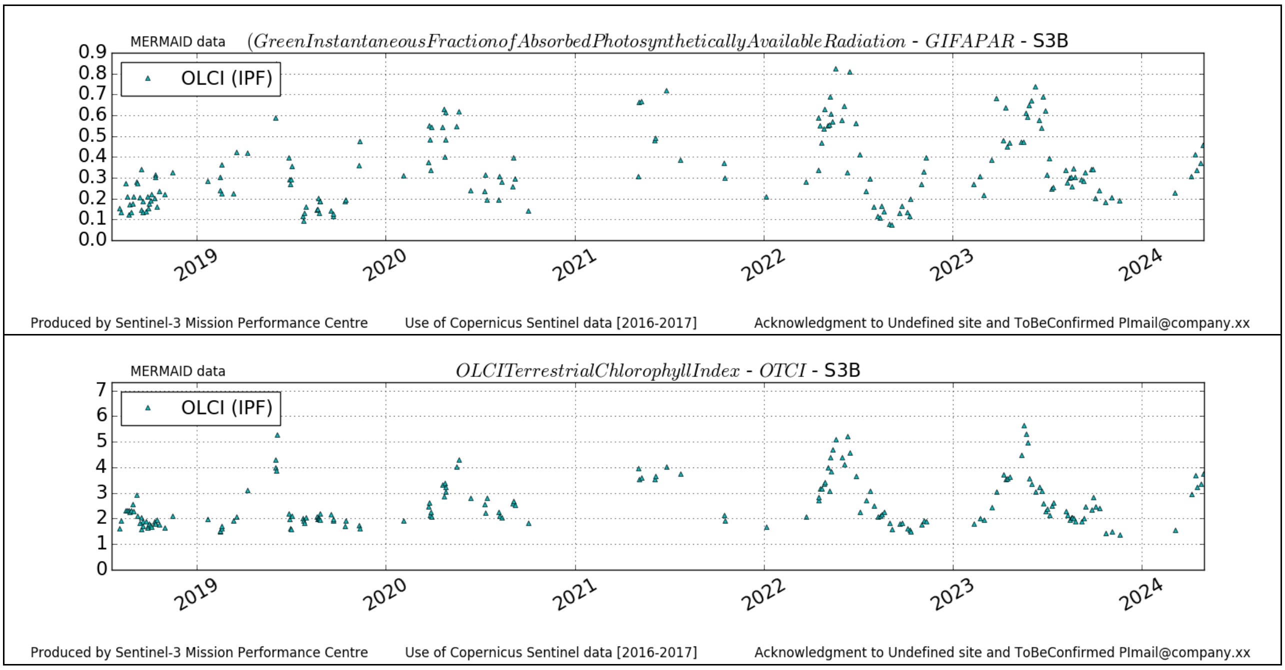

Figure 85: DeGeb time series over current report period

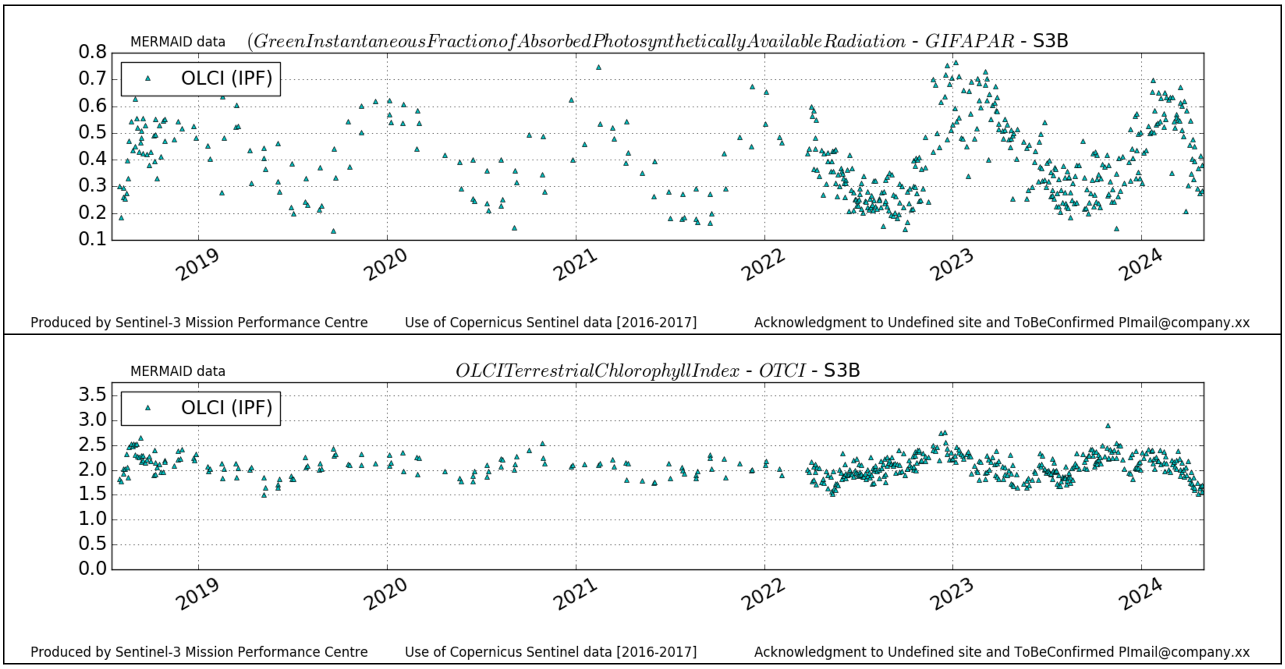

Figure 86: ITCat time series over current report period

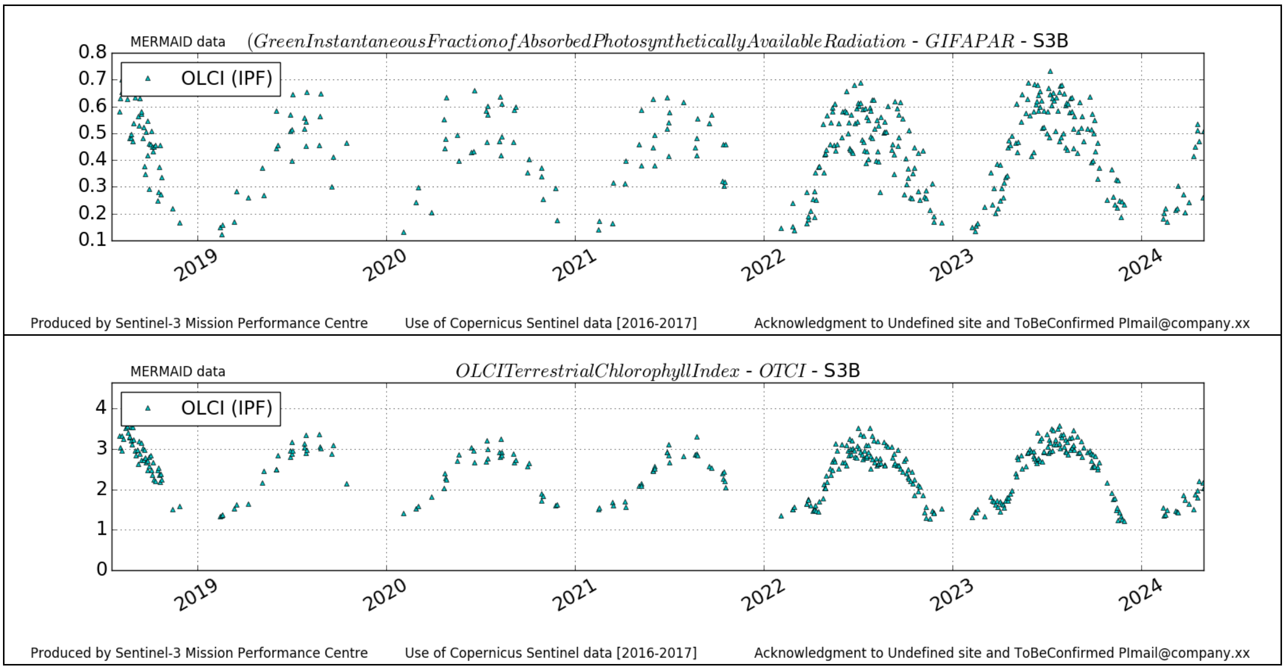

Figure 87: ITIsp time series over current report period

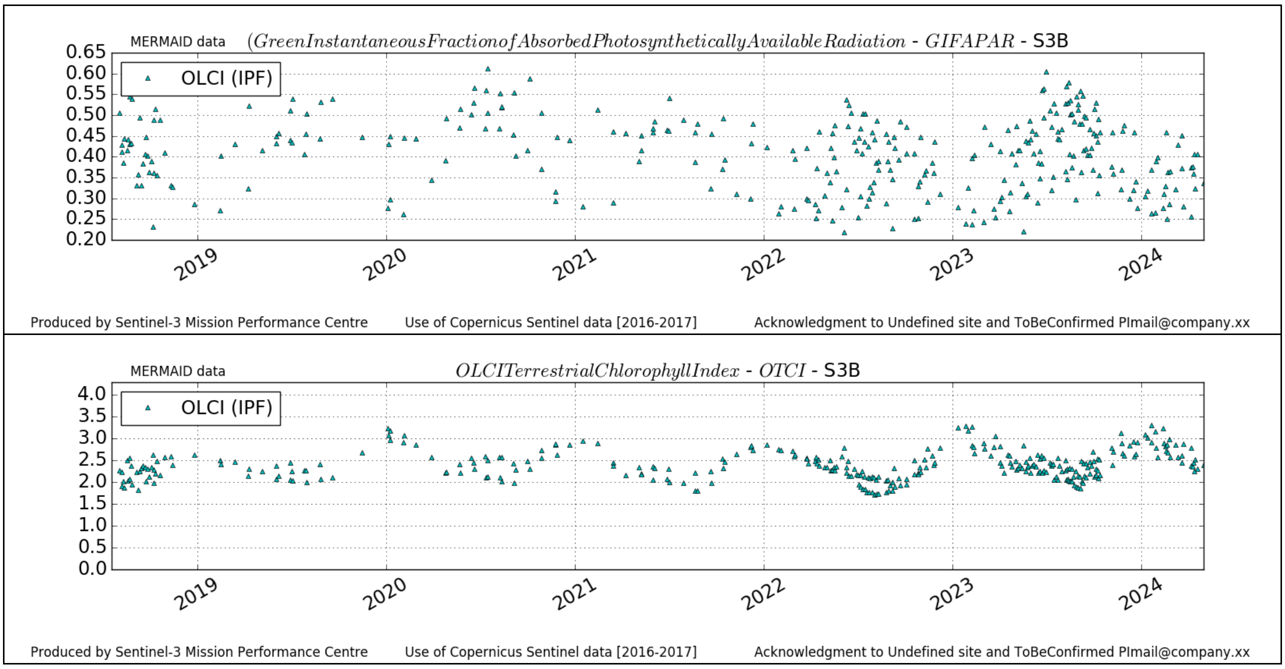

Figure 88: ITSro time series over current report period

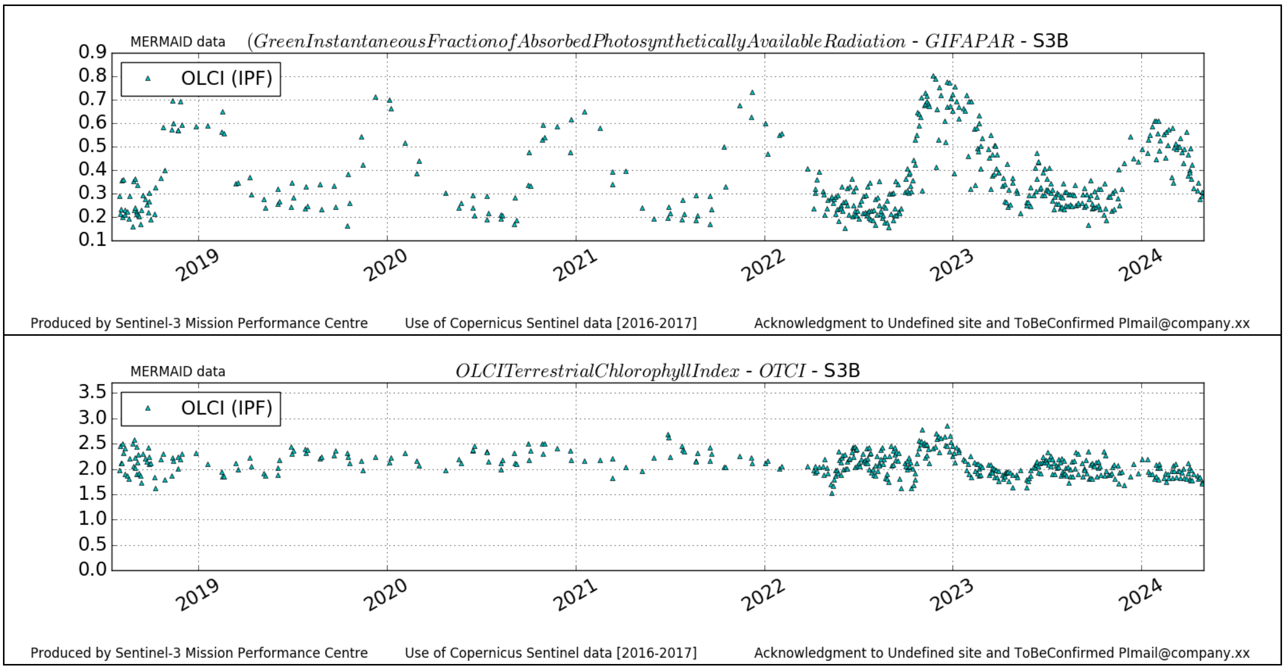

Figure 89: ITTra time series over current report period

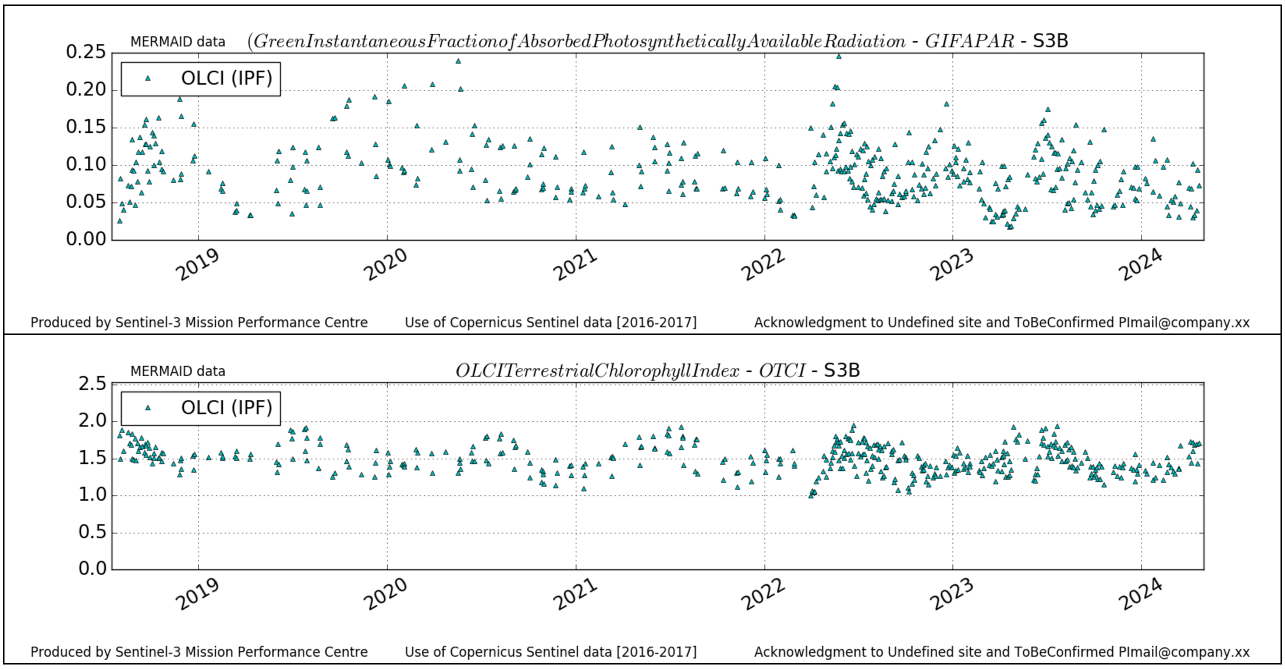

Figure 90: SPAli time series over current report period

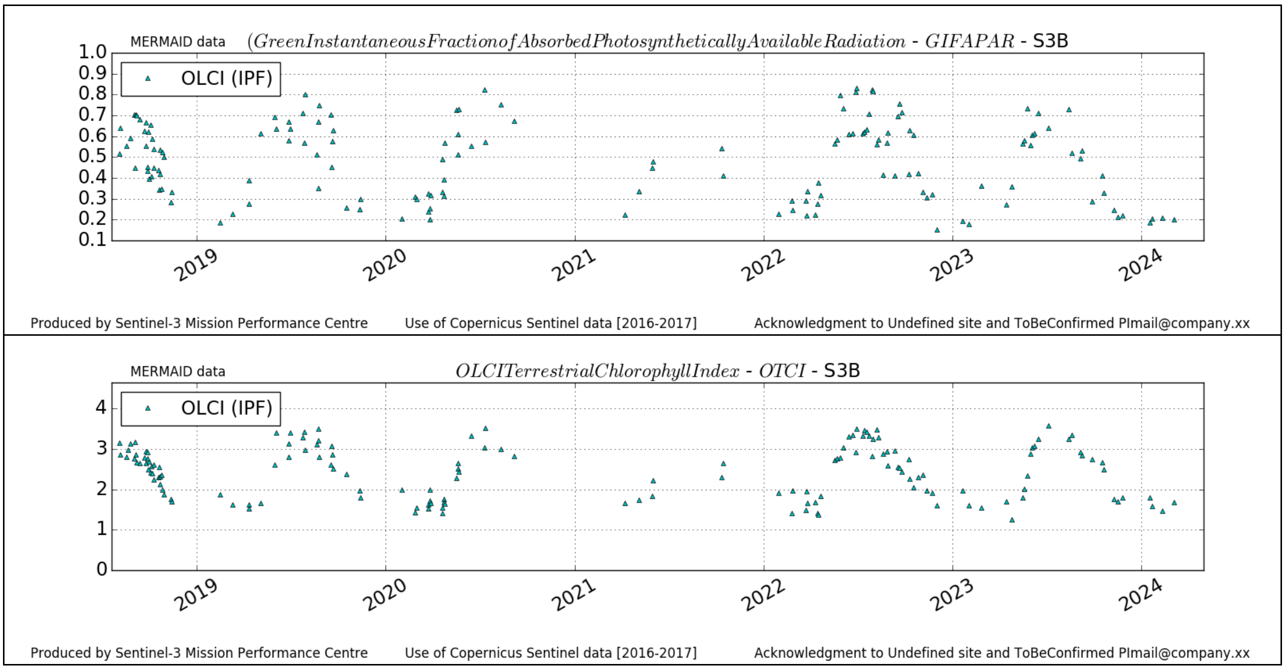

Figure 91: UKNFo time series over current report period

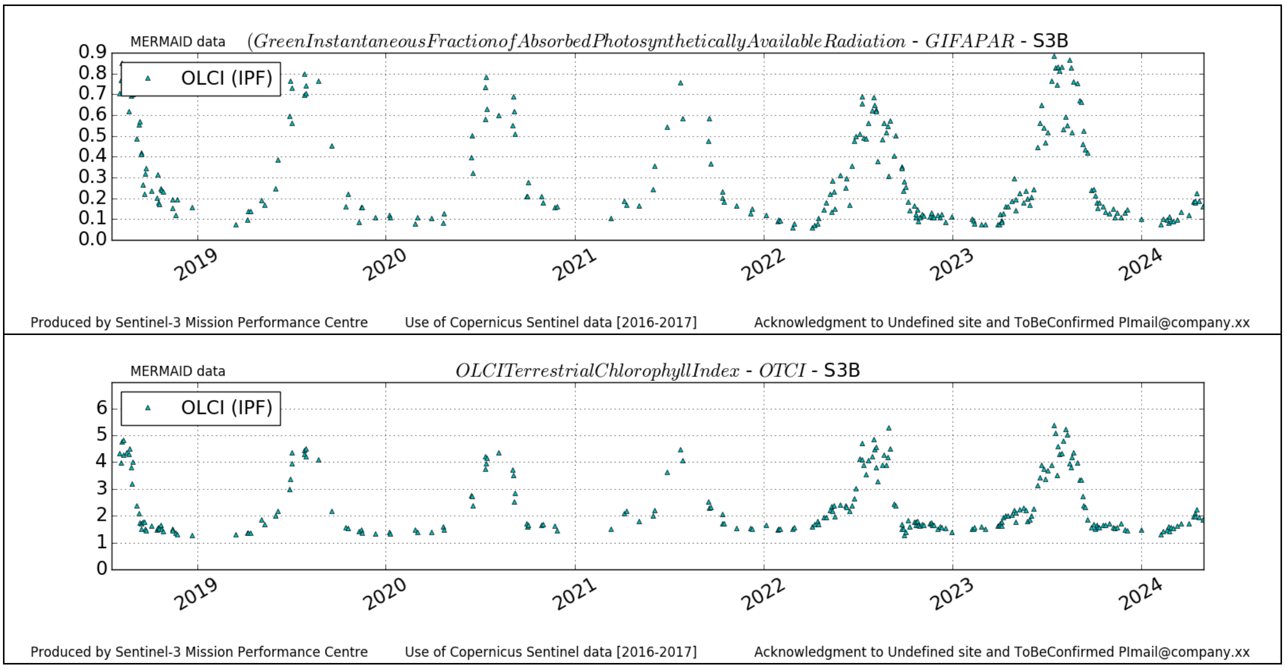

Figure 92: USNe1 time series over current report period

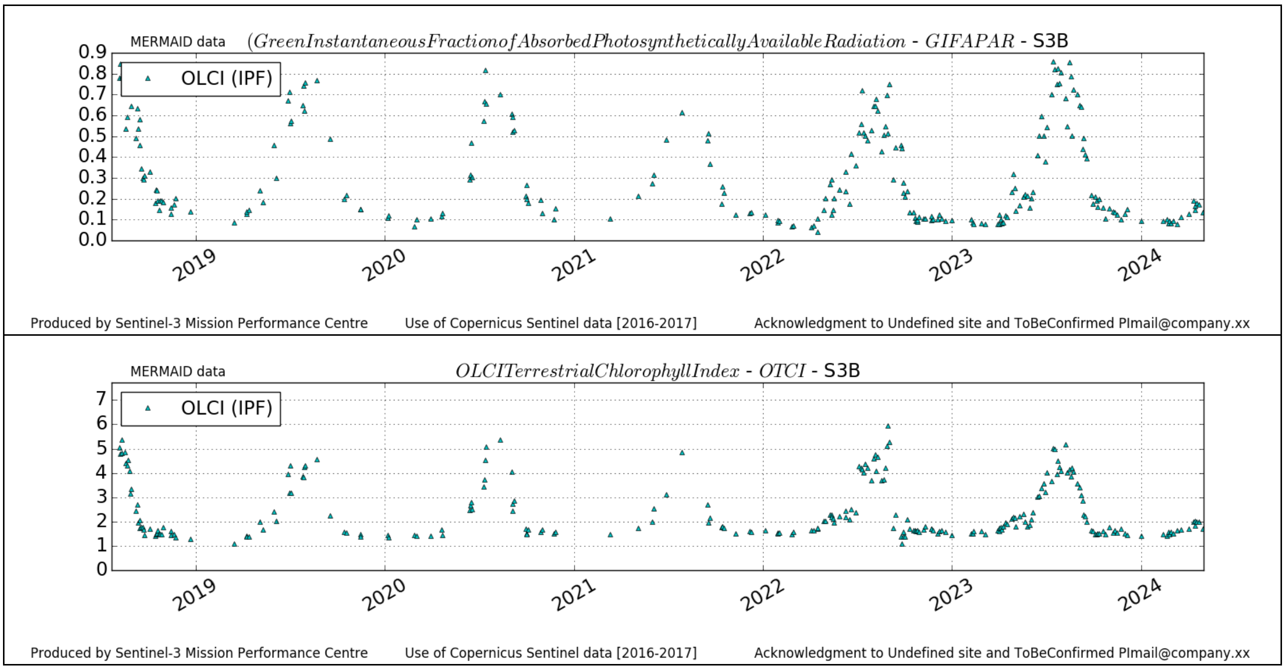

Figure 93: USNe2 time series over current report period

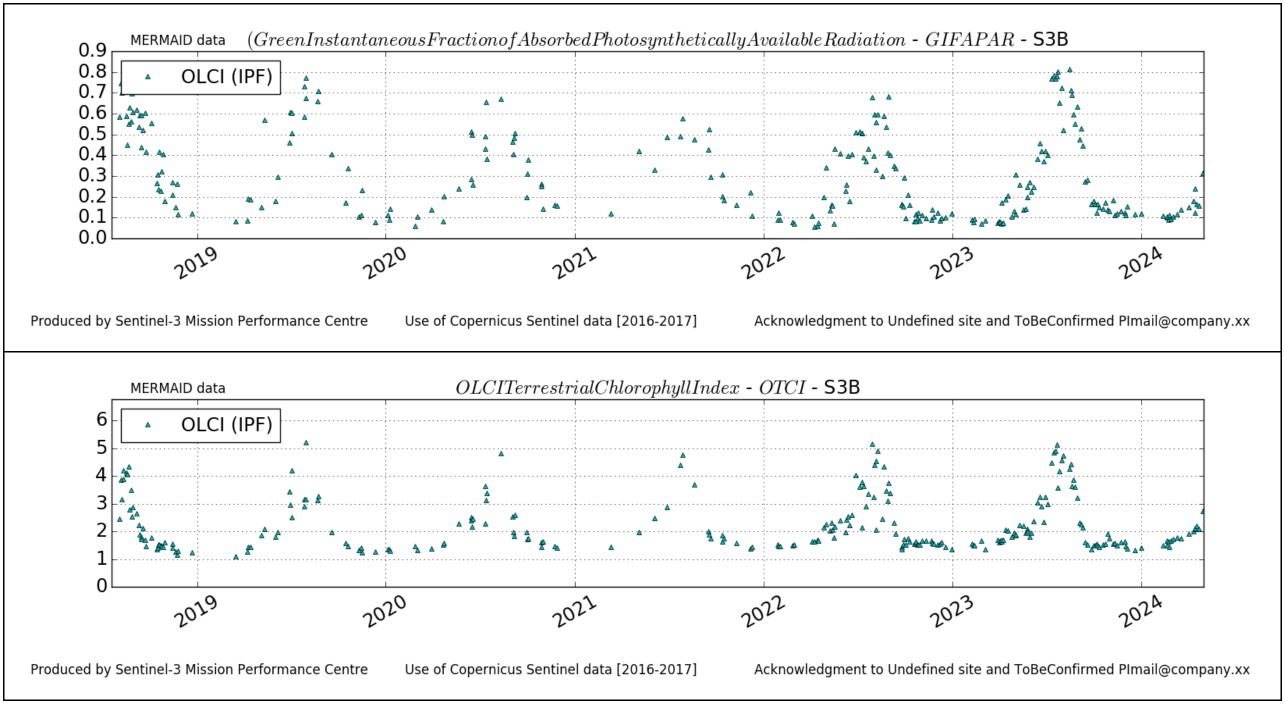

Figure 94: USNe3 time series over current report period

4.1.2 Comparison with MERIS MTCI Climatology

This section presents a comparison between MERIS and OLCI land products (GIFAPAR-*Green Instantaneous Fraction of Absorbed Photosynthetically Available Radiation*- and OTCI -*Terrestrial Chlorophyll Index* -) from 1st January 2023 to 30th April 2024 across a selection of sites from the S3VT (*Sentinel-3 Validation Team*), CEOS (*Committee for Earth Observation Satellites*) and GBOV (*Ground-Based Observations for Validation*) sites (Table 8). OTCI is compared against the L3 Envisat MERIS Terrestrial Chlorophyll Index (MTCI) composites at 1 km spatial resolution, sourced from the UK Centre for Environmental Data Analysis (CEDA). GIFAPAR is compared against MERIS FAPAR climatology (MGVI – MERIS fourth reprocessing over 2003-2011 at 1.2 km). The 15-day smoothed product from daily data is sourced by the Joint Research Centre (Gobron *et al.,* 2022).

Figure 95 depicts seasonal trends and scatterplots of the monthly mean for the period 2002-2012 (grey), 2023 GIFAPAR (blue), and 2024 GIFAPAR (red) at specific sites for S3A and S3B. Similar to previous DQRs, there is a robust alignment between GIFAPAR seasonality and MGVI climatology (R^2>0.3; NRMSD<-0.2 for nearly all sites). OTCI also demonstrates a strong concurrence with MTCI (Figure 96). This indicates its capacity to maintain continuity in the 10-year MERIS archive and provide confidence in its performance. Table 9 shows the monthly mean comparison. The worst results are observed at sites with sparse vegetation, such as shrubland and grassland. Sites with a low correlation between OTCI and MTCI also exhibit a low R2 between GIFAPAR and MGVI.

Table 8: S3VT, CEOS and GBOV validation sites analysed.

Name	Country	LAT	LON	IGBP
Sp-Ala	Spain	38.45	−1.06	Semi-arid Mediterranean
AUS-Alice Mulga	Australia	-22.28	133.25	Evergreen Needleleaf
FR-Aurade	France	43.54	1.10	Croplands
US-Bartlett	United States	44.06	-71.287	Mixed Forest
US-Blandy	United States	39.06	-78.07	Deciduous Broadleaf
CZ-Bily Kriz forest	Czechia	49.50	18.53	Evergreen Needleleaf
BE-Brasschaat	Belgium	51.30	4.51	Evergreen Needleleaf
AUS-Calperum Malle	Australia	-34.00	140.58	Shrubland
AUS-Cape Tribulation	Australia	-16.10	145.37	Evergreen Needleleaf
It-Castelporziano	Italy	41.70	12.35	Mixed Forest
It-Cat	Italy	37.27	14.88	Croplands (Orange)
US-Central Plains	United States	40.815	-104.74	Grasslands
IT-CollelongoITALY	Italy	41.84	13.58	Deciduous Broadleaf broadleaved, deciduous, closed
AUS-Cumberland Plain	Australia	-33.61	150.72	Evergreen Broadleaf
US-Dead Lake	United States	32.54172	-87.8039	Mixed Forest
US-Disney	United States	28.12504	-81.4363	Shrublands
FR-Estrees	France	49.87	3.02	Croplands
De-Geb	Germany	51.10	10.91	Croplands
US-Guanica	United States	17.96	-66.868	Mixed Forest
AUS-Great Western	Australia	-30.19	120.65	Shrublands
GE-Hainich	Germany	51.07	10.45	Mixed Forest
US-Harvard	United States	42.53	-72.17	Mixed Forest
FR-Hesse	France	48.67	7.06	Deciduous Broadleaf
DE-Hones Holtz	Germany	52.08	11.22	Deciduous Broadleaf
It-Isp	Italy	45.81	8.63	Mixed Forest
US-Jones	United States	31.19	-84.46	Evergreen Needleleaf
US-Jornada	United States	32.59	-106.84	Open shrubland
US-Konza	United States	39.11	-96.61	Croplands
US-Lajas	United States	18.02	-67.07	Grasslands
IT-Lison	Italy	45.74	12.75	Croplands
AUS-Litchfield	Australia	-13.18	130.79	Evergreen Broadleaf
NE-Loobos	Netherlands	52.16	5.74	Evergreen Needleleaf
US-Moab	United States	38.24	-109.38	Shrublands
FR-Montiers	France	48.53	5.31	Deciduous Broadleaf
US-Mountain Lake	United States	37.37	-80.52	Deciduous Broadleaf
US-Niwot	United States	40.05	-105.58	Evergreen Needleleaf
US-Oak	United States	35.96	-84.28	Mixed Forest
US-Onaqui	United States	40.17	-112.45	Shurblands
US-Ordway	United States	29.68	-81.9934	Evergreen Needleleaf
FR-Puechabon	France	43.74	3.59	Evergreen Needleleaf
AUS-Robson Creek	Australia	-17.11	145.63	Mixed Forest
AUS-Rushworth	Australia	-36.75	144.96	Deciduous Broadleaf
DE-Selhausen	Germany	50.86	6.44	Cropland
US-Smithsonian Conservation Biology (SCBI)	United States	38.89	-78.13	*Mixed Forest*
US-Smithsonian Environmental (SERC)	United States	38.89	-76.56	*Croplands*
US-Steigerwaldt	United States	45.50	-89.58	*Deciduous Broadleaf*
It-Sro	Italy	43.72	10.28	*Pinus Pinea*
US-Talladega	United States	32.95	-87.39	Evergreen Needleleaf
DE-Tharandt	Germany	50.96	13.56	Evergreen Needleleaf
It-Tra	Italy	37.64	12.85	Croplands (Vineyards and olive trees)
AUS-Tumbarumba	Australia	-35.65	148.15	Evergreen Broadleaf
USNe1	United States	41.165	-96.47	Croplands
USNe2	United States	41.16	-96.47	Croplands
USNe3	United States	41.17	-96.43	Croplands
Sp- Valencia	Spain	39.57	-1.28	Croplands
BE-Vielsalm	Belgium	50.30	5.99	Evergreen Needleleaf
AUS-Warra Tall	Australia	-43.09	146.65	Evergreen Broadleaf
AUS-Watts Creek	Australia	-37.68	145.68	Evergreen Broadleaf
US-Woodworth	United States	47.12	-99.24	Grasslands
AUS-Wombat	Australia	-37.42	144.09	Evergreen Broadleaf
AUS-Zig zag	Australia	-37.47	148.33	Evergreen Broadleaf

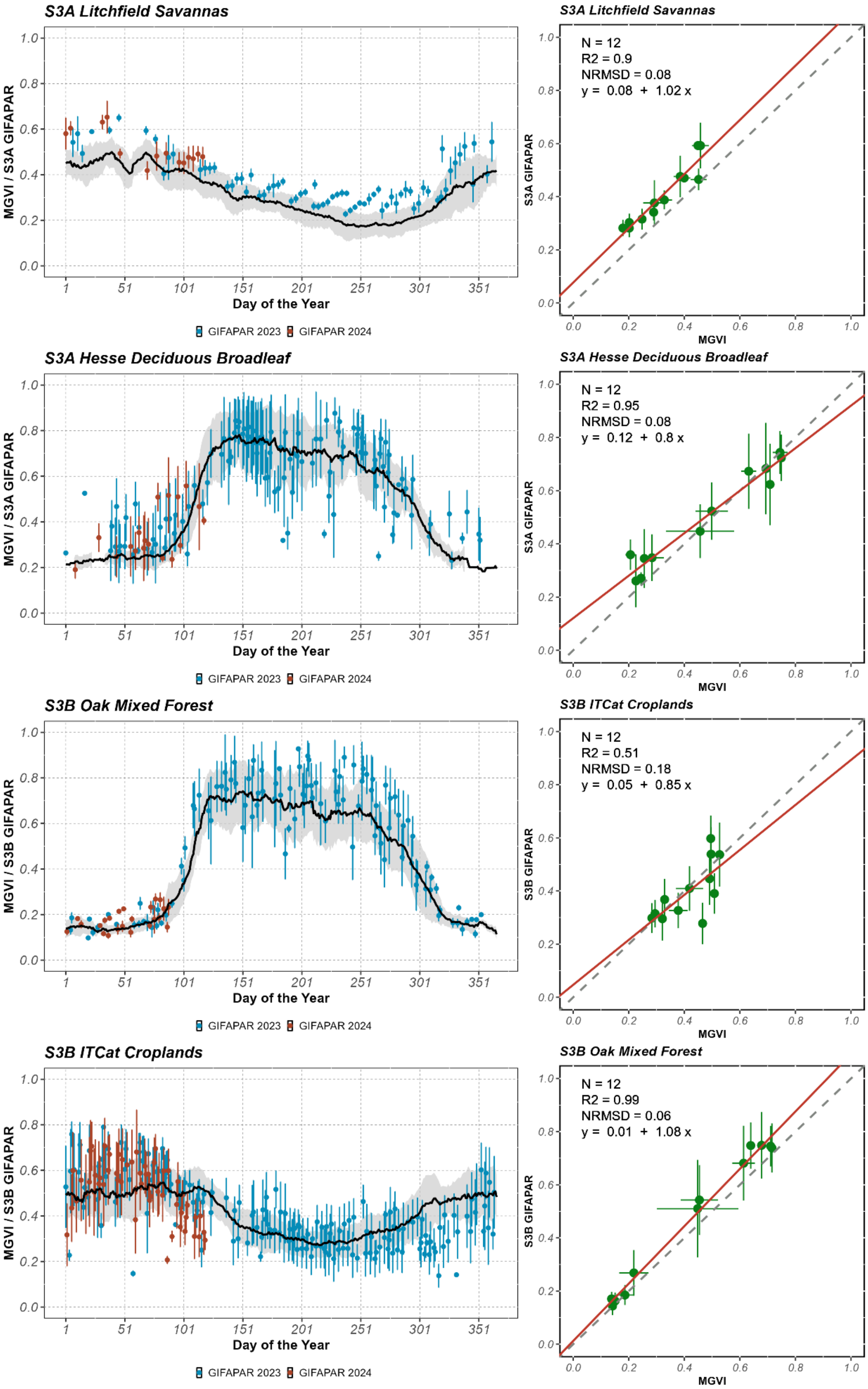

Figure 95: Time series (left) of GIFAPAR and MGVI and a corresponding scatterplot of the monthly mean for site Litchfield and Hesse (representing S3A), ItCat and Oak (representing S3B). The climatology of MERIS FAPAR (black and grey colours) is compared against 2023 (blue colours) and 2024(red colours).

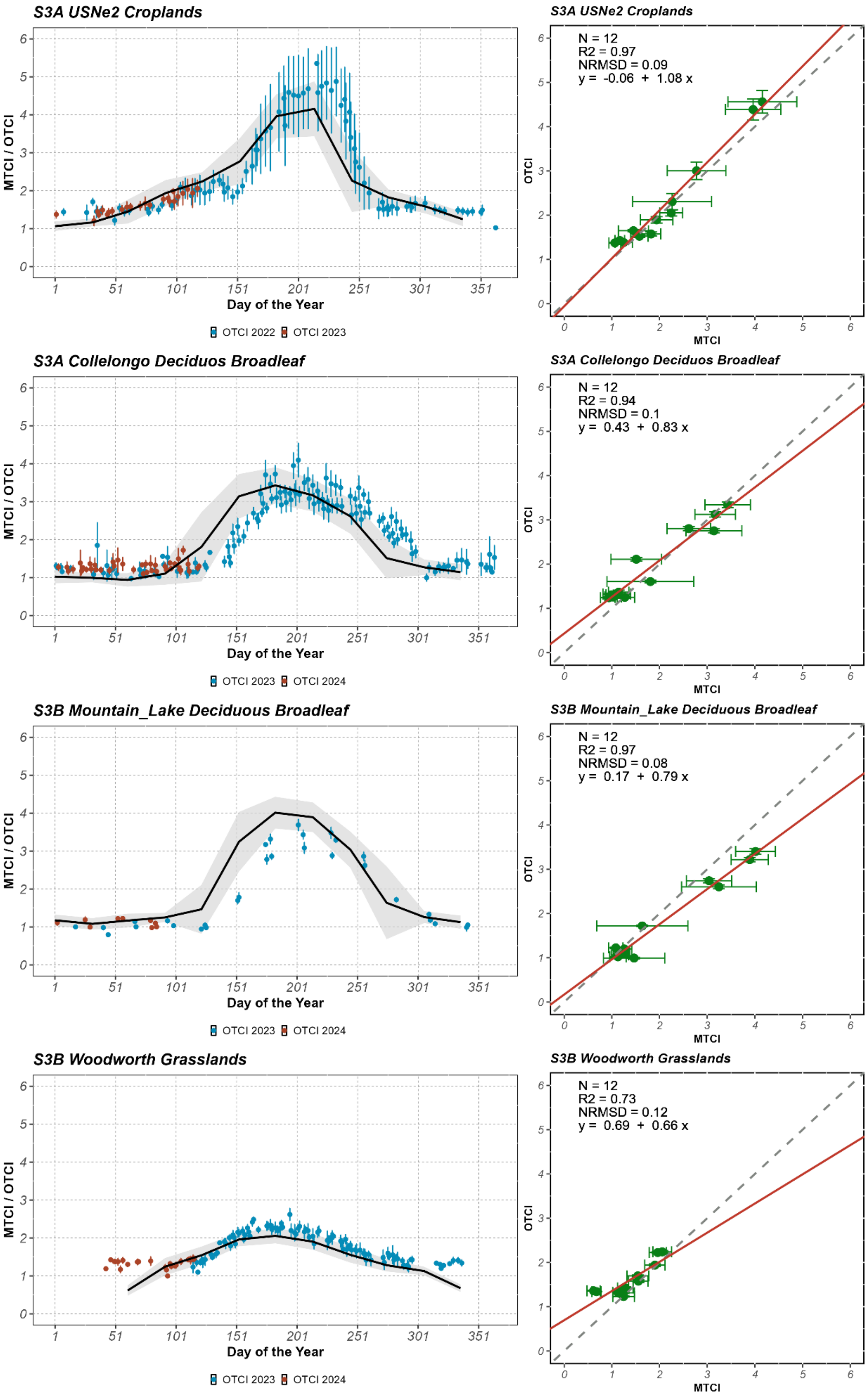

Figure 96: Time series (left) of OTCI and MTCI and a corresponding scatterplot of the monthly mean for sites USNe2 and USNe2 (representing S3A), Mountain Lake and Woodworth (representing S3B). The climatology of MERIS MTCI (black and grey colours) is compared against 2023 (blue colours) and 2024 (red colours).

Table 9: Comparison statistics between monthly S3A/B OLCI land products and MERIS archive data. Yellow is R^2<0.4, light green R^2 between 0.9-0.95, and dark green R^2>0.95.

	GIFAPAR S3A			GIFAPAR S3B			OTCI S3A			OTCI S3B		
Site	**N**	**R2**	**NRMSD**	**N**	**R2**	**NRMSD**	**N**	**R2**	**NRMSD**	**N**	**R2**	**NRMSD**
AU-Alice Mulga	12	0.43	0.1	12	0.44	0.1	12	0.27	0.08	12	0.23	0.07
AU-Calperum_Mallee	12	0.21	0.19	12	0.28	0.14	12	0.55	0.07	12	0.53	0.06
AU-Cape Tribulation	12	0.86	0.09	10	0.65	0.08	12	0.21	0.04	10	0.24	0.06
AU-Cumberland_Plain	12	0.49	0.18	12	0.45	0.17	12	0.58	0.07	12	0.75	0.06
AU-Great_Western	12	0.69	0.09	12	0.7	0.08	12	0.48	0.06	12	0.48	0.06
AU-Litchfield	12	0.9	0.08	12	0.84	0.1	12	0.86	0.03	12	0.83	0.04
AU-Robson_Creek	12	0.75	0.08	12	0.71	0.1	12	0.88	0.03	12	0.87	0.03
AU-Rushworth	12	0.85	0.07	12	0.61	0.1	12	0.85	0.07	12	0.85	0.07
AU-Tumbarumba	12	0.14	0.22	12	0.24	0.17	12	0.42	0.09	12	0.66	0.07
AU-Warra_Tall	12	0.28	0.14	12	0.46	0.1	12	0.84	0.04	12	0.86	0.04
AU-Watts_Creek	12	0.14	0.15	12	0.22	0.07	12	0.76	0.04	12	0.73	0.04
AU-Wombat	12	0.3	0.07	12	0.36	0.13	12	0.96	0.03	12	0.95	0.03
AU-Zigzag	12	0.61	0.09	12	0.44	0.1	12	0.94	0.03	12	0.91	0.03
BE-Brasschaat	12	0.91	0.11	12	0.85	0.13	12	0.95	0.06	12	0.92	0.08
BE-Vielsalm	12	0.9	0.09	12	0.72	0.16	12	0.76	0.05	12	0.88	0.06
CZ-Bili Kriz	12	0.86	0.09	12	0.81	0.11	12	0.31	0.09	12	0.47	0.09
DEGeb	12	0.74	0.2	12	0.82	0.21	12	0.9	0.11	12	0.88	0.15
DE-Hainich	11	0.95	0.11	12	0.97	0.09	12	0.91	0.15	12	0.92	0.14
DE-Hones Holz	12	0.93	0.12	12	0.93	0.13	12	0.96	0.1	12	0.96	0.09
DE-Selhausen	12	0.6	0.13	12	0.43	0.26	12	0.81	0.1	12	0.83	0.09
DE-Tharandt	12	0.85	0.16	12	0.93	0.11	12	0.89	0.08	12	0.86	0.09
FR-Aurade	12	0.95	0.07	12	0.87	0.09	12	0.89	0.07	12	0.93	0.05
FR-Estrees	12	0.49	0.2	12	0.31	0.22	12	0.81	0.12	12	0.85	0.1
FR-Hesse	12	0.95	0.08	12	0.96	0.08	12	0.94	0.07	12	0.97	0.07
FR-Montiers	12	0.97	0.07	12	0.95	0.1	12	0.95	0.09	12	0.97	0.08
FR-Puechabon	12	0.66	0.06	12	0.83	0.05	12	0.53	0.09	12	0.57	0.09
IT-Castelporziano2	12	0.92	0.05	12	0.57	0.09	12	0.83	0.04	12	0.79	0.05
IT-Cat	12	0.36	0.25	12	0.51	0.18	12	0.53	0.06	12	0.54	0.07
IT-Collelongo	12	0.94	0.12	12	0.93	0.14	12	0.94	0.1	12	0.93	0.11
IT-Isp	11	0.98	0.05	11	0.99	0.04	12	0.97	0.05	12	0.98	0.04
IT-Sro	12	0.77	0.06	12	0.71	0.06	12	0.91	0.03	12	0.89	0.04
IT-Tra	12	0.5	0.19	12	0.35	0.21	12	0.59	0.03	12	0.61	0.03
NE-Loobos	12	0.92	0.08	12	0.77	0.1	12	0.88	0.04	12	0.74	0.06
SP-Ali	12	0.16	0.21	12	0.2	0.22	12	0.7	0.04	12	0.6	0.05
SP-Valencia	12	0.4	0.15	12	0.54	0.24	12	0.87	0.04	12	0.87	0.06
UK-NFo	12	0.85	0.17	12	0.96	0.09	12	0.93	0.08	12	0.97	0.06
US-Bartlett	12	0.99	0.05	12	0.97	0.08	12	0.97	0.04	12	0.99	0.02
US-Blandy	12	0.43	0.14	12	0.89	0.1	12	0.41	0.11	12	0.82	0.06
US-Central_Plains	12	0.75	0.35	12	0.72	0.41	12	0.49	0.14	12	0.57	0.12
US-Dead_Lake	12	0.99	0.05	12	0.98	0.07	12	0.98	0.04	12	0.99	0.04
US-Disney	12	0.85	0.05	12	0.91	0.05	12	0.7	0.03	12	0.71	0.03
US-Guanica	12	0.31	0.08	12	0.7	0.05	12	0.45	0.13	12	0.52	0.11
US-Harvard	12	0.97	0.08	12	0.98	0.07	12	0.97	0.07	12	0.98	0.06
US-Jones	12	0.97	0.05	12	0.98	0.05	12	0.91	0.04	12	0.9	0.04
US-Jornada	9	0.74	0.08	12	0.24	0.35	12	0.65	0.06	12	0.75	0.05
US-Konza	12	0.93	0.17	12	0.91	0.19	12	0.89	0.1	12	0.83	0.12
US-Lajas	12	0.31	0.1	12	0.8	0.07	12	0.24	0.07	12	0.35	0.06
US-Moab	12	0.27	0.12	12	0.21	0.16	12	0.38	0.03	12	0.29	0.03
US-Mountain Lake	12	0.99	0.06	12	0.9	0.19	12	1	0.03	12	0.97	0.08
US-Niwot	9	0.25	0.12	9	0.3	0.23	12	0.23	0.07	10	0.22	0.11
US-Oak	12	1	0.03	12	0.99	0.06	12	0.99	0.03	12	0.99	0.04
US-Onaqui	12	0.67	0.12	12	0.49	0.2	12	0.75	0.1	12	0.62	0.13
US-Ordway	12	0.72	0.05	12	0.28	0.14	12	0.3	0.03	12	0.26	0.05
US-SCBI	12	0.99	0.06	12	0.91	0.16	12	0.99	0.05	11	0.99	0.04
US-SERC	12	0.99	0.06	12	0.98	0.07	12	0.99	0.05	12	0.97	0.07
US-Steigerwaldt	12	0.97	0.1	12	0.96	0.11	12	0.93	0.07	12	0.95	0.06
US-Talladega	12	0.97	0.06	12	0.99	0.04	12	0.94	0.05	12	0.96	0.04
US-Underc	12	0.98	0.08	12	0.97	0.11	12	0.95	0.07	12	0.96	0.07
US-USNe1	12	0.99	0.08	12	0.97	0.14	12	0.97	0.08	12	0.97	0.09
US-USNe2	12	0.99	0.09	12	0.98	0.13	12	0.97	0.09	12	0.96	0.1
US-USNe3	12	0.95	0.15	12	0.92	0.24	12	0.94	0.1	12	0.9	0.14
US-Woodworth	12	0.98	0.09	12	0.98	0.08	12	0.8	0.11	12	0.73	0.12

4.1.3 Comparison with GBOV (Ground-Based Observations for Validation) data v3

This DQR compares the ground-based measurements from the Copernicus GBOV service and OLCI GIFAPAR products until 31st December 2022. Compared to the May 2023 DQR, we included new sites and evaluated four protocols to improve the validation to match GBOV and Sentinel-3 data. The protocols include 1) considering all the pixels extracted by MERMAID, 2) focusing on the central point of MERMAID extractions and the surrounding 3×3 window, 3) focusing on the tower and the 3×3 window and 4) focusing on the ESU measurements of each site. This DQR presents the results corresponding to protocol 3, which proved to be one of the most robust protocols. The selected sites are distributed across various geographical locations, representing different land cover types (Table 10).

Table 10: GBOV validation sites analysed.

ID	Name	Country	LAT	LON	IGBP	Min DOY MaxDOY
USA_BART	Bartlett Experimental Forest	USA	44.0639	-71.2873	Mixed Forest	8 - 349
USA_BLAND	Blandy Experimental Farm	USA	39.0602	-78.07164	Deciduous Broadleaf	3 - 362
USA_CPER	Central Plains Experimental Range	USA	40.81555	-104.7460	Grasslands	3 - 362
USA_DELA	Dead Lake	USA	32.5417	-87.80389	Deciduous Broadleaf	8 - 349
USA_DSYN	Disney Wilderness Preserve	USA	28.12504	-81.43625	Open shrublands	8 - 349
PRI_GUAN	Guanica Forest	Puerto Rico	17.9695	-66.8687	Evergreen Broadleaf	8 - 349
GER-HAIN	Hainich	Germany	51.0792	10.4522	Mixed Forest	8-349
USA_HARV	Harvard	USA	42.5378	-72.1715	Mixed Forest	8 - 349
USA_JERC	Jones Ecological Research Center	USA	31.194	-84.468	Evergreen Needeleleaf	8 - 349
USA_JORN	Jornada	USA	32.5907	-106.842	Open Shrubland	3 - 362
USA_KONA	Konza Prairie Biological Station	USA	39.114	-96.6129	Croplands	3 - 362
PRI_LAJA	Lajas	USA	18.02125	-67.0769	Grasslands	3 - 362
AUS_LIT	Litchfield	AUS	-13.18	130.79	Woody Savannas	3 - 362
USA_Moab	Moab	USA	38.2483	-109.388	Open Shrubland	3 - 362
USA_NRMN	Niwot Ridge Mountain Research Station	USA	40.0543	-105.5824	Evergreen Needleleaf	3 - 362
USE_STER	North Sterling	USA	40.4619	-103.029	Grasslands	3 - 362
USA_ORNL	Oak Ridge	USA	35.9641	-84.2826	Mixed Forest	8 - 349
USA_ONAQ	Onaqui Ault	USA	40.1775	-112.4524	Open shrublands	3 - 362
USA_OSBS	Ordway Swisher Biological Station	USA	29.67615	-82.00847	Evergreen Needleleaf	8 - 349
USA_SRER	Santa Rita	USA	31.91068	-110.8354	Closed Shurbland	3 - 362
USA_SCBI	Smithsonian Conservation Biology	USA	38.8902	-78.1395	Mixed Forest	8 – 349
USA_SERC	Smithsonian Environmental Research Centre	USA	38.8901	-76.5601	Croplands	8 - 349
USA_STEI	Steigerwaldt Land Services	USA	45.5089	-89.5864	Deciduous Broadleaf	8 - 349
USA_TALL	Talladega National Forest	USA	32.9504	-87.3933	Evergreen Needleleaf	8 - 349
AUS_TUMB	Tumbarumba	AUS	-35.6565	148.1516	Evergreen Broadleaf	8 - 349
USA_UNDE	Underc	USA	46.23395	-89.53751	Mixed Forest	8 - 349
ESP_VASN	Valencia Anchor Station	ESP	39.5707	-1.28822	Cropland Mosaics	3 - 362
AUS_WOMB	Wombat	AUS	-37.422	144.0944	Evergreen Broadleaf	8 - 349
USA_WOOD	Woodworth	USA	47.12823	-99.2413	Grassland	3 - 362

Figure 97 shows the comparison between GBOV against OLCI-A and OLCI-B for all the analyzed sites.

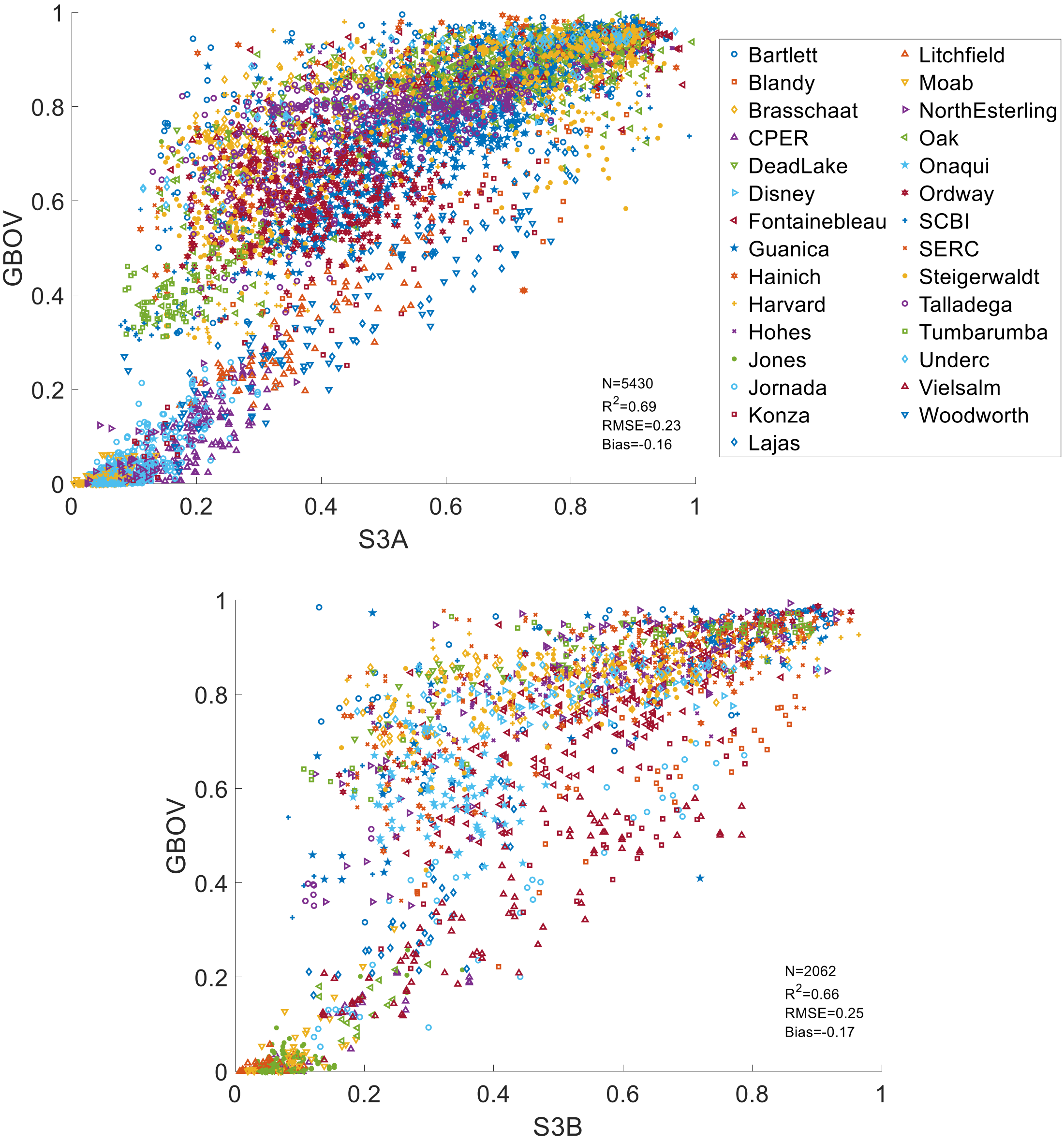

Figure 97: Comparison of GBOV vs OLCI-A (top) and GBOV vs OLCI-B (bottom).

4.1.3.1 OLCI-A

Figure 98 to Figure 100 illustrate the variability of both in situ values from GBOV and their corresponding OLCI-A matchups over time. Similarly to the results of 2021, OLCI-A and OLCI-B satisfactorily reproduce the temporal variations of GBOV values. Sites such as Moab (Figure 99) and CPER (Figure 98) exhibit some problems for 2022, with flat values for GBOV. GBOV systematically shows higher values than OLCI-A in forest classes. Conversely, satellite products report higher values than GBOV in shrubland and grassland areas.

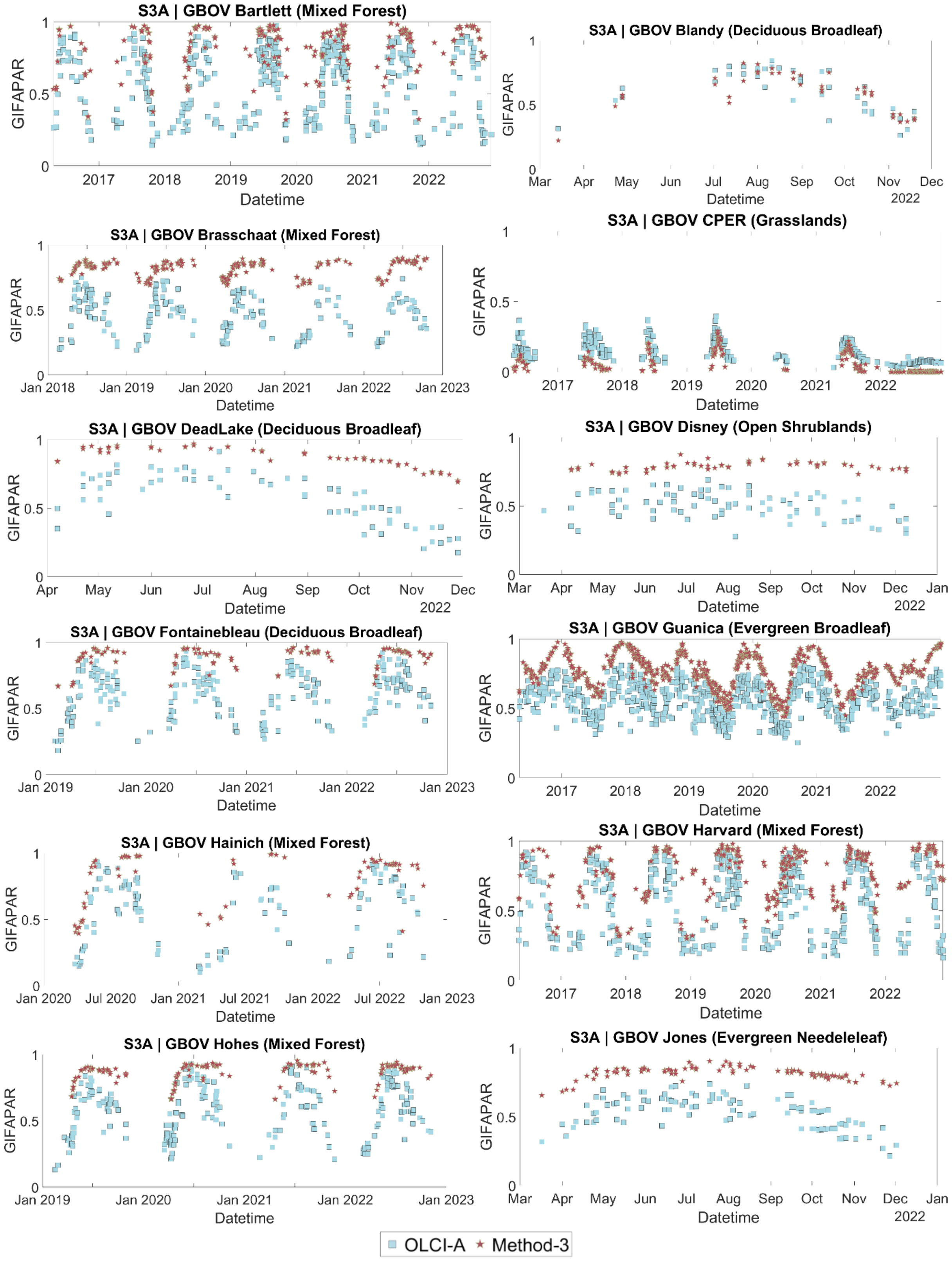

Figure 98: Time series of OLCI-A GIFAPAR (blue-sky) and GBOV data (red).

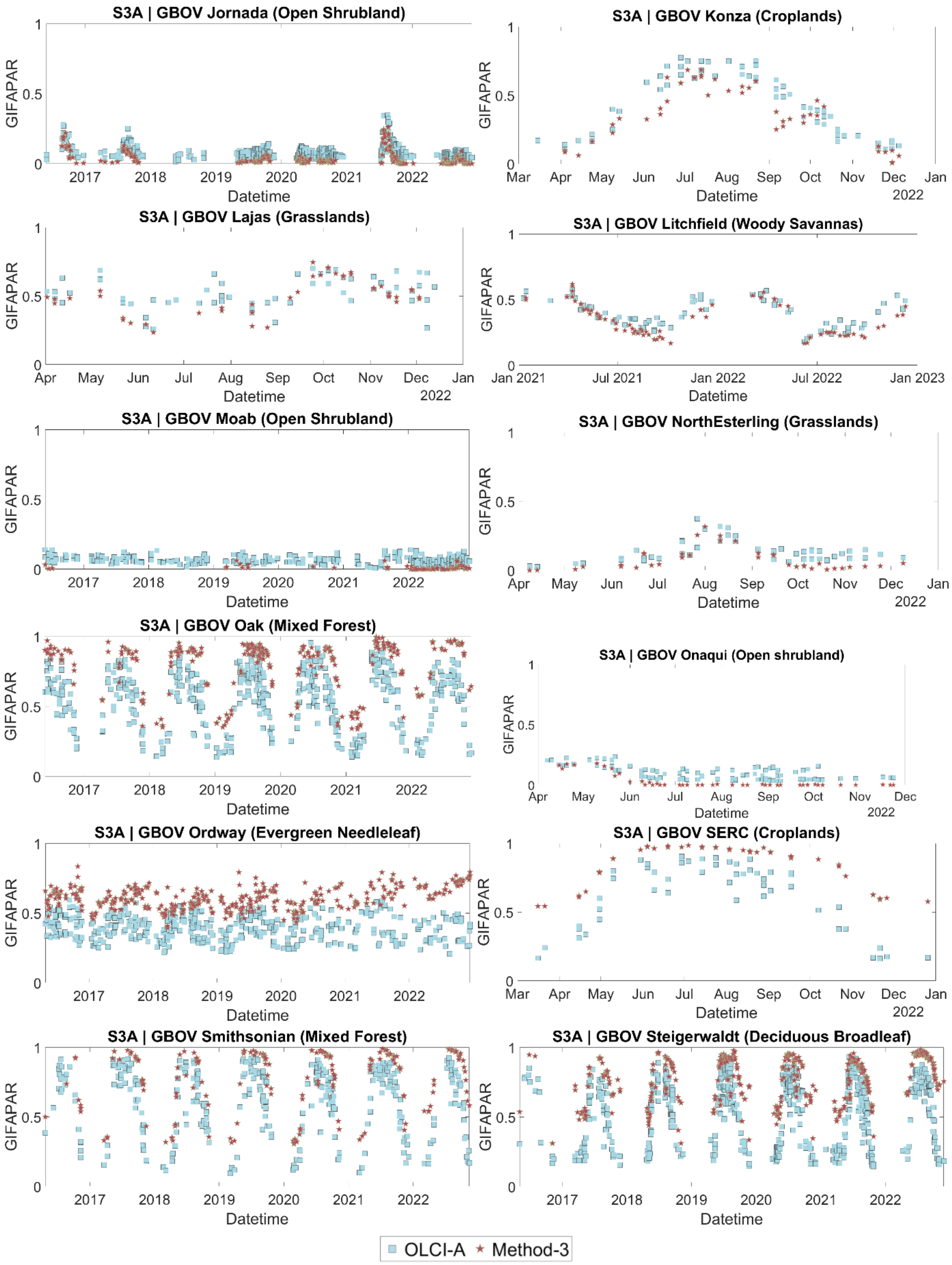

Figure 99: Time series of OLCI-A GIFAPAR (blue-sky) and GBOV data (red).

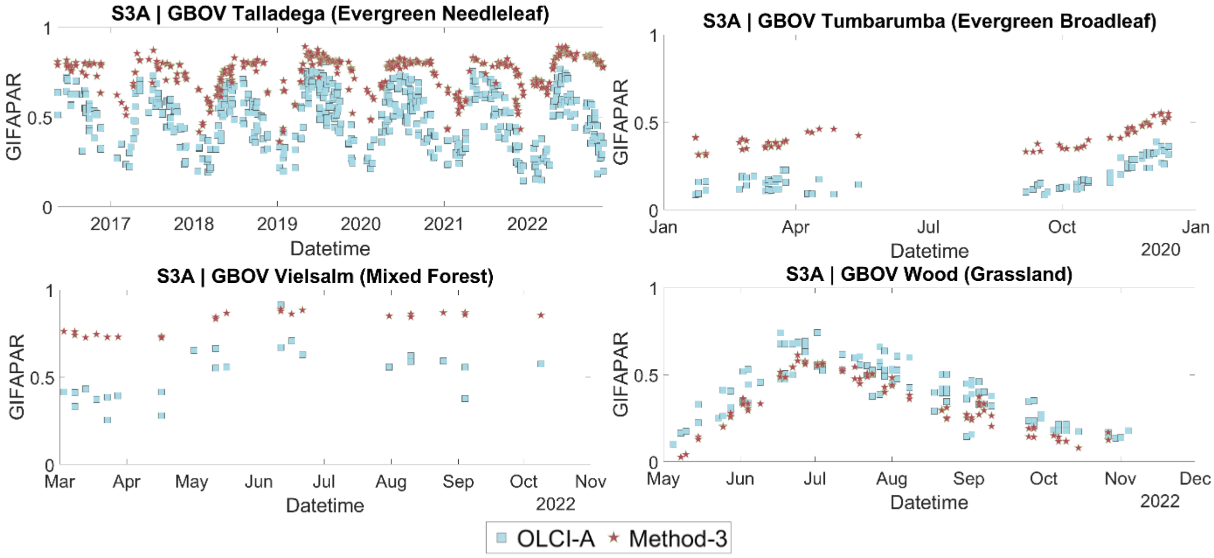

Figure 100: Time series of OLCI-A GIFAPAR (blue-sky) and GBOV data (red).

4.1.3.2 OLCI-B

Figure 101 to Figure 103 show the temporal profiles of GBOV LP4 against those of OLCI-B GIFAPAR. Overall, there are similar seasonal trajectories between OLCI-B and GBOV. The pattern is similar to OLCI-A, with higher values of GBOV than those of OLCI-B for forest classes. Similarly, grassland and shrubland classes show lower values than OLCI-B (i.e., Wood). Furthermore, the number of GBOV values after filtering (GBOV and GIFAPAR data) must be increased to perform the validation, mainly in grasslands and shrublands sites (i.e., Moab, Central Plains).

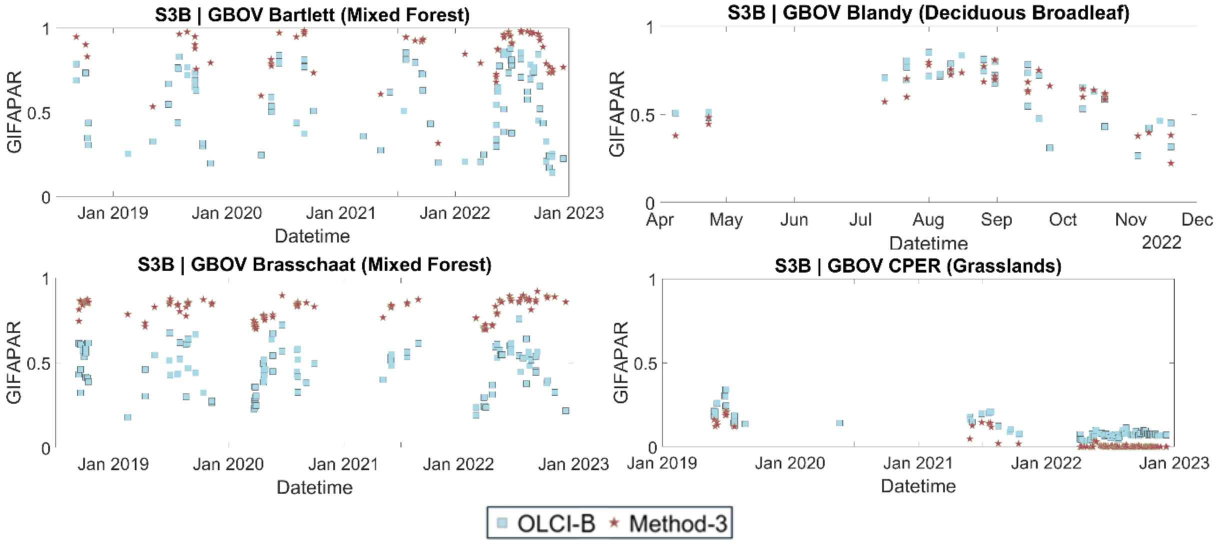

Figure 101: Time series of OLCI-A GIFAPAR (blue-sky) and GBOV data (red).

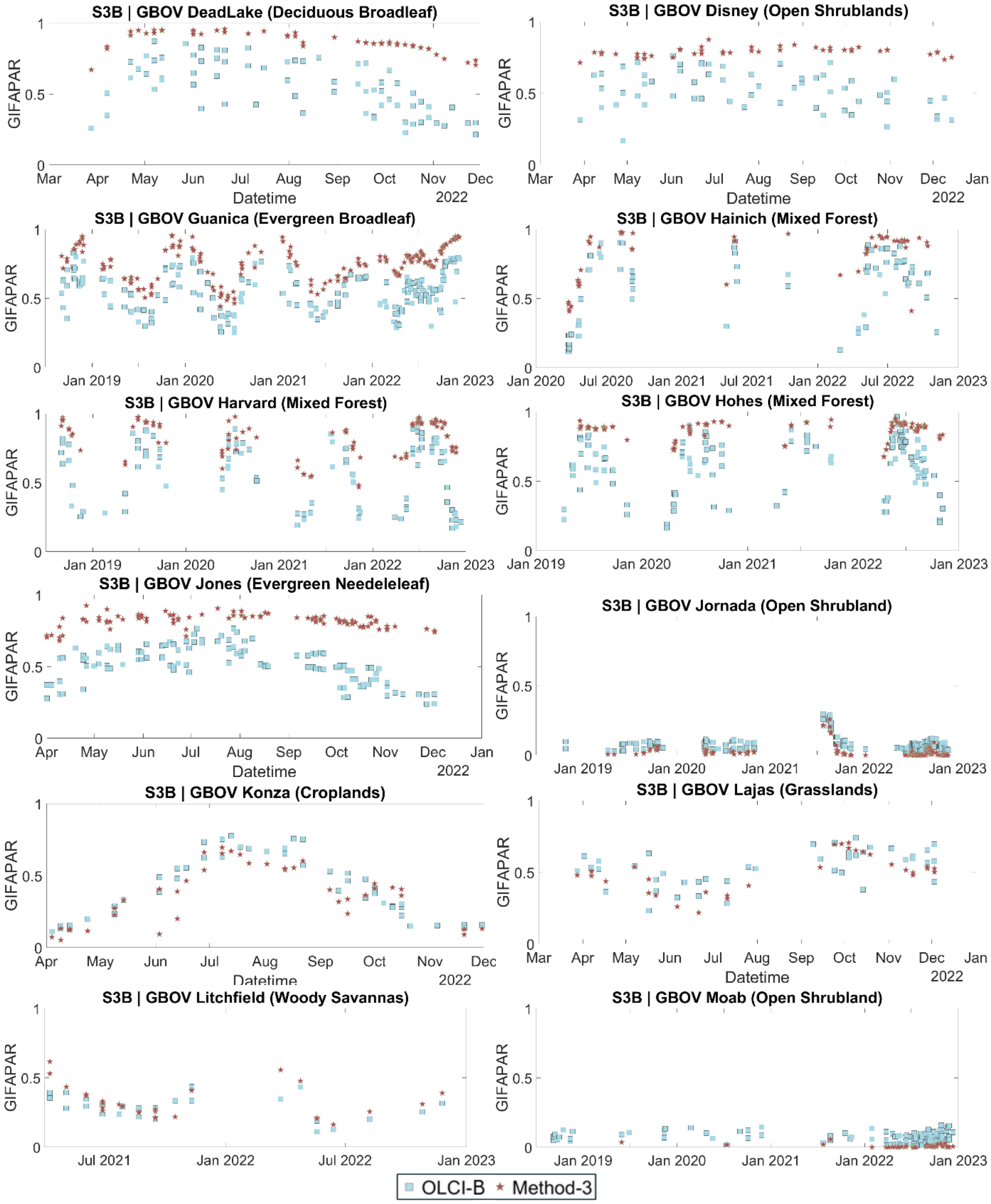

Figure 102: Time series of OLCI-A GIFAPAR (blue-sky) and GBOV data (red).

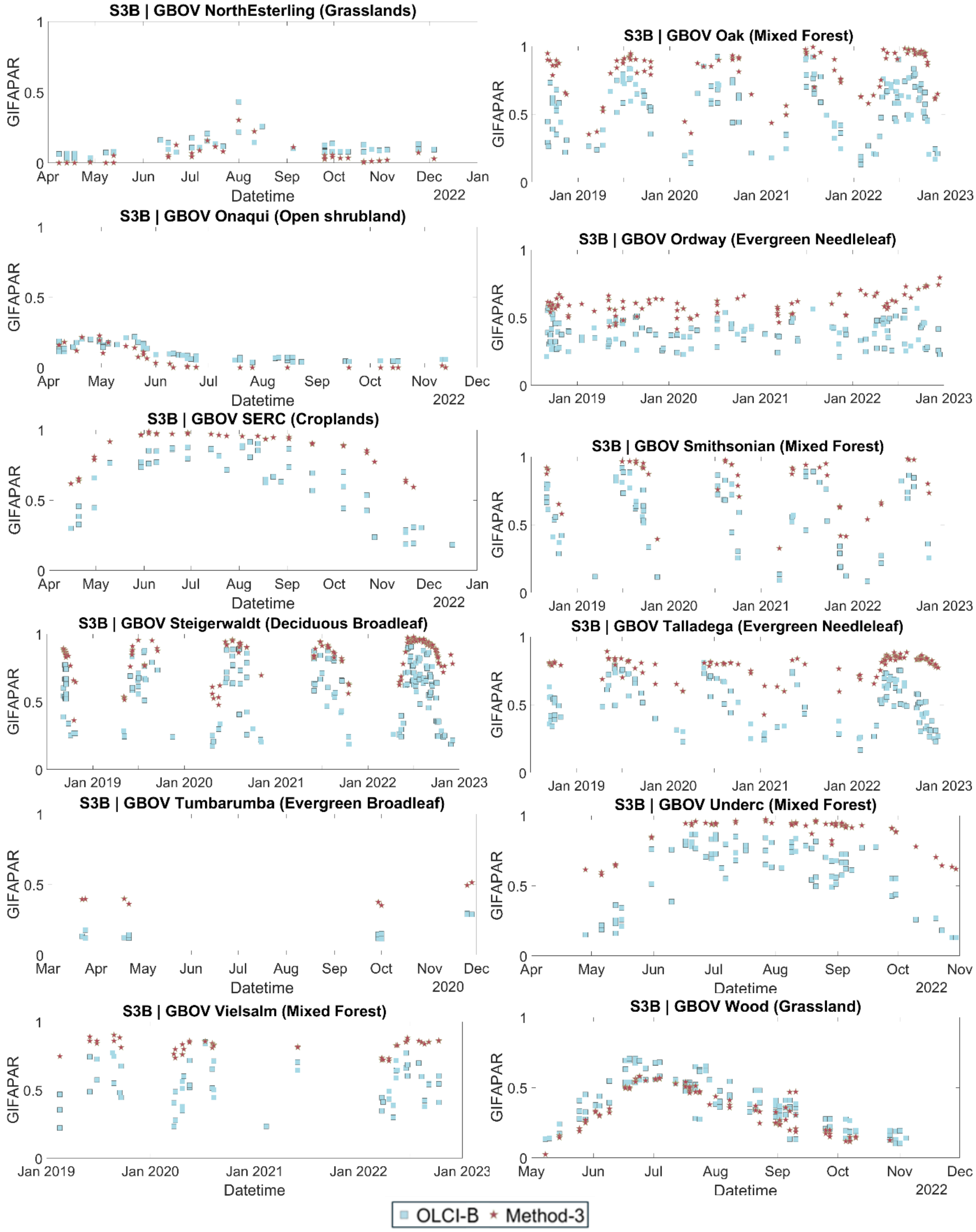

Figure 103: Time series of OLCI-A GIFAPAR (blue-sky) and GBOV data (red).

4.1.4 Sentinel-3A and 3B biophysical variables inter-annual variability results

There have been no new results during the reporting period. The latter figures (reported in the OLCI Data Quality Report covering September 2023) are considered valid.

4.2 [OLCI-L2LRF-CV-410 & OLCI-L2LRF-CV-420] – Cloud Masking & Surface Classification for Land Products

For the April 2024 reporting the prototype validation results for OLCI cloud mask using sky cameras (SC) are based on two sites, currently validated independently. The two sites are located at La Sapienza University in Rome, Italy and at the University of Valencia in Spain.

After water inleakage at SC2 at La Sapienza University, Rome and shifts in SC1, the sky cameras have been replaced in Q1 of 2024. Since April, the data is again available for validation to Brockmann Consult GmbH. Since SC1 is stable now, the validation has again switched to SC1.

The coordinates of SC 1 at La Sapienza University are:

- Lat: 41.90294
- Lon: 12.51327

The coordinates of the location of SC 1 at University of Valencia are:

- Lat: 39.50832
- Lon: -0.42084

4.2.1.1 Sky Camera based validation – prototype results April 2024

4.2.1.2 Rome

Figure 108 and Figure 109 show the prototype validation results for the Rome site in April 2024. The weather in April around Rome is quite arid with less than half of the month’s days being clouded (see Figure 104 and Figure 105). The average rainfall for April is between 3 to 8 days.

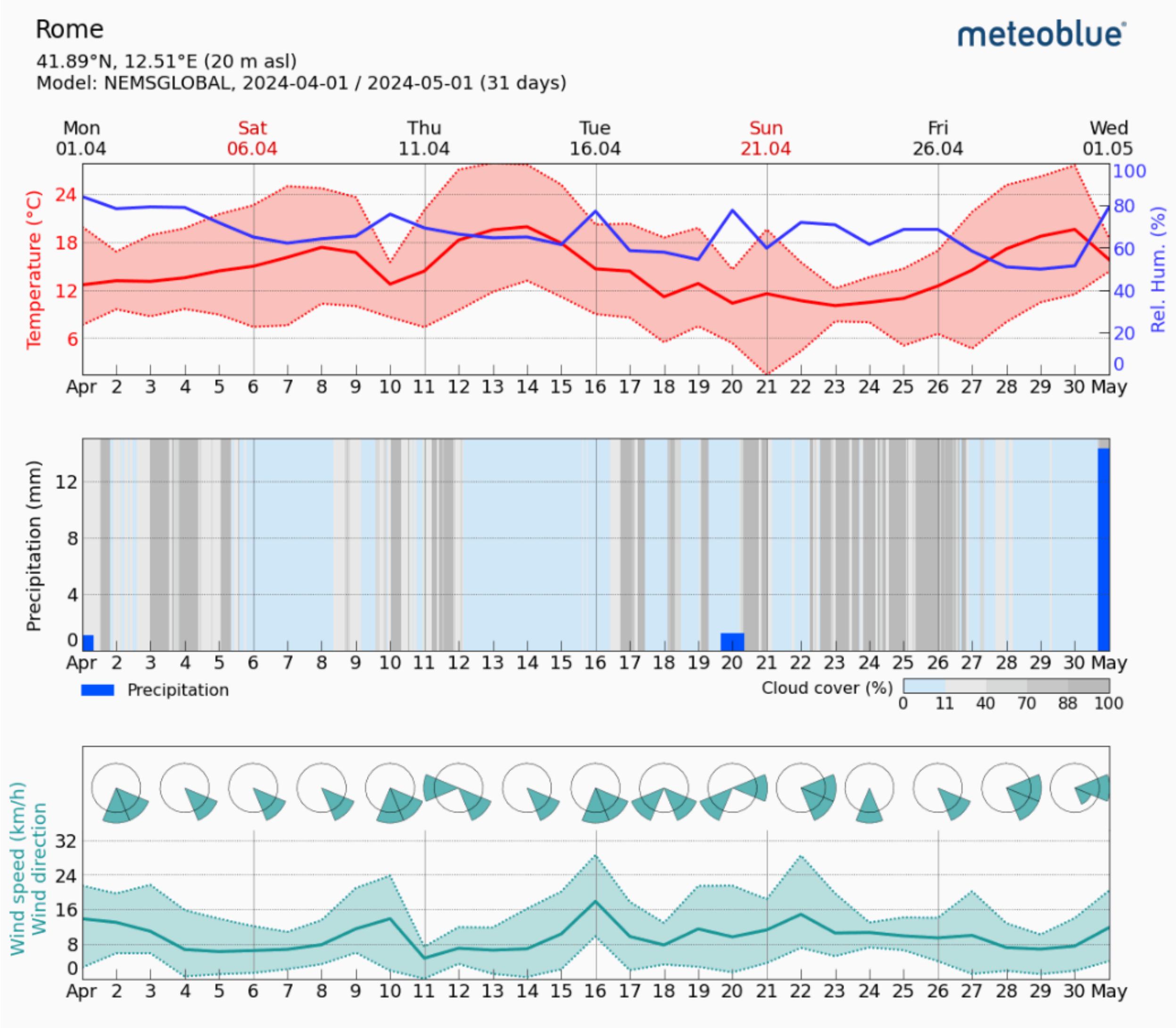

Figure 104: Temperature, cloud cover and precipitation Rome, April 2024 (source: https://www.meteoblue.com/en/weather/historyclimate/weatherarchive/rome_italy_3169070?fcstlength=1m&year=2024&month=4)

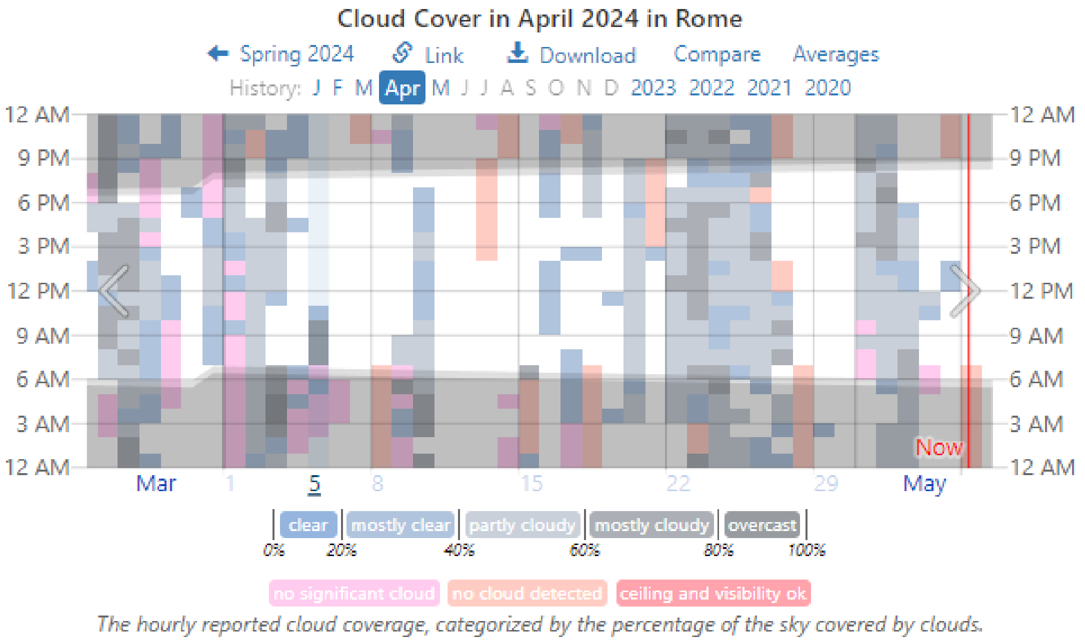

The hourly reported cloud coverage, categorized by the percentage of the sky covered by clouds.

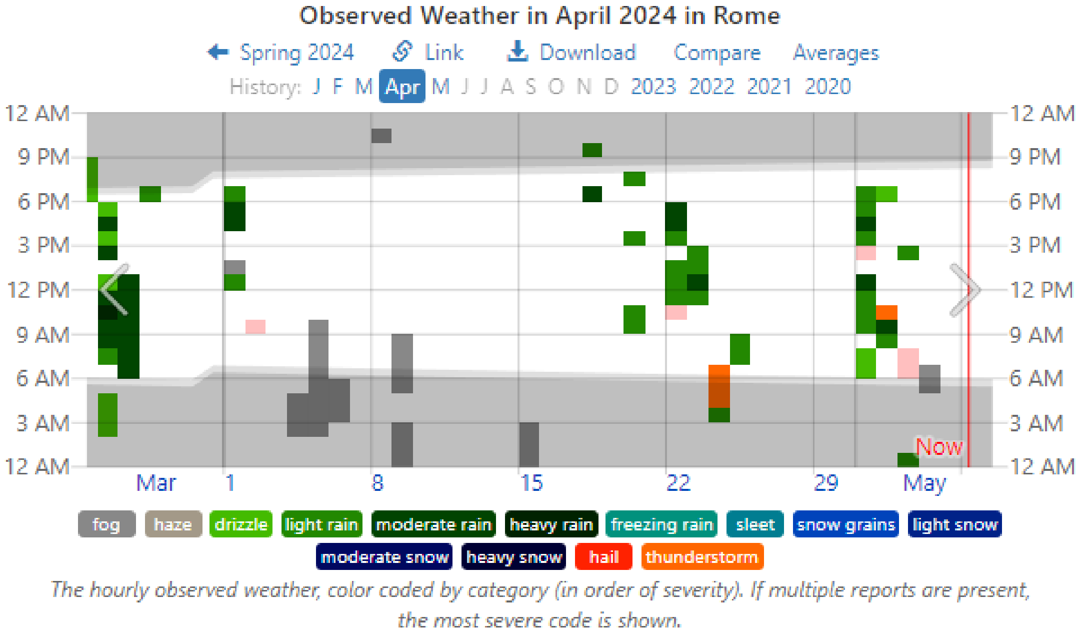

The hourly observed weather, color coded by category (in order of severity). If multiple reports are present, the most severe code is shown.

Figure 105: Cloud observations and precipitation Rome, April 2024 (source: https://weatherspark.com/h/m/71779/2024/4/Historical-Weather-in-April-2024-in-Rome-Italy#Figures-ObservedWeather)

In April, there have been 20 acquisitions below 30 degree OZA. Five to seven of the SC observation show mostly clear sky conditions (see Figure 106). Even though the sun is close to the centre of all acquisitions, the SC classification (see Figure 107) shows only a little cloud bias. When the majority of the reference window, used for the classification, is classified as sun, those observations are not used for the comparison.

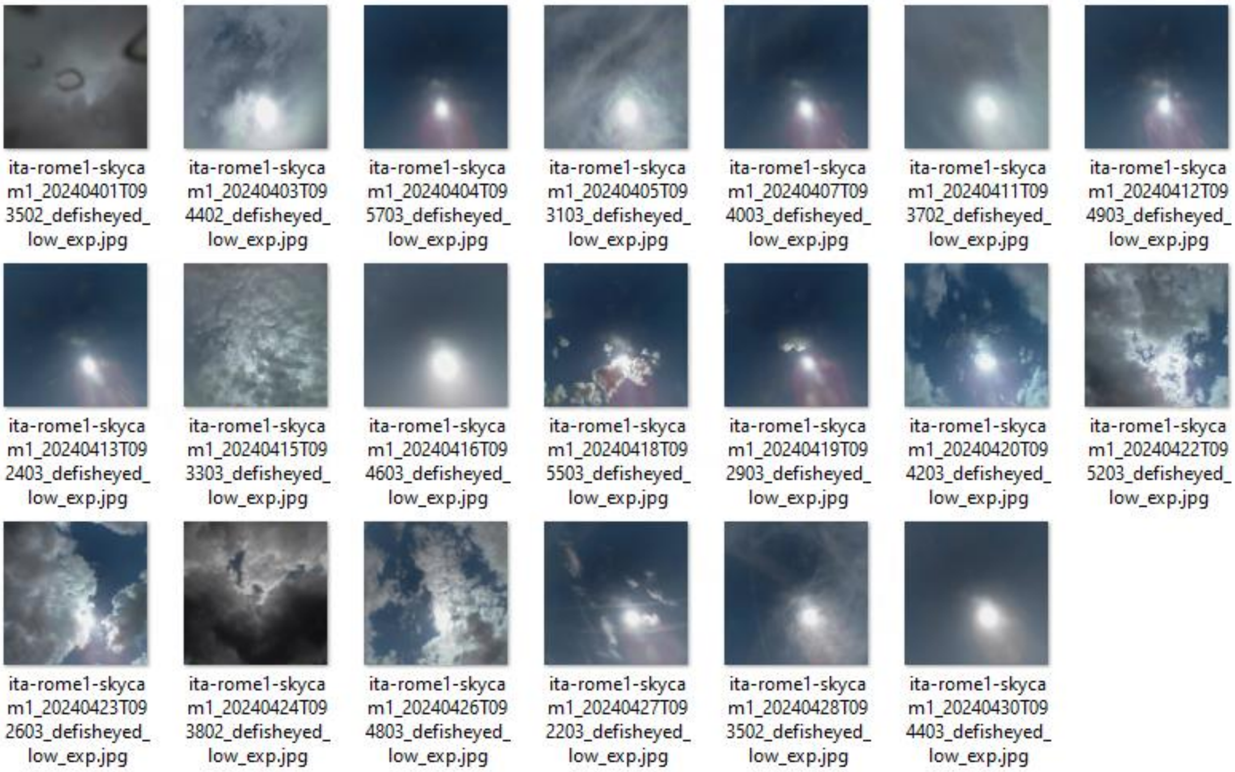

ita-rome1-skycam1_20240401T093502_defisheyed_low_exp.jpg
ita-rome1-skycam1_20240403T094402_defisheyed_low_exp.jpg
ita-rome1-skycam1_20240404T095703_defisheyed_low_exp.jpg
ita-rome1-skycam1_20240405T093103_defisheyed_low_exp.jpg
ita-rome1-skycam1_20240407T094003_defisheyed_low_exp.jpg
ita-rome1-skycam1_20240411T093702_defisheyed_low_exp.jpg
ita-rome1-skycam1_20240412T094903_defisheyed_low_exp.jpg
ita-rome1-skycam1_20240413T092403_defisheyed_low_exp.jpg
ita-rome1-skycam1_20240415T093303_defisheyed_low_exp.jpg
ita-rome1-skycam1_20240416T094603_defisheyed_low_exp.jpg
ita-rome1-skycam1_20240418T095503_defisheyed_low_exp.jpg
ita-rome1-skycam1_20240419T092903_defisheyed_low_exp.jpg
ita-rome1-skycam1_20240420T094203_defisheyed_low_exp.jpg
ita-rome1-skycam1_20240422T095203_defisheyed_low_exp.jpg
ita-rome1-skycam1_20240423T092603_defisheyed_low_exp.jpg
ita-rome1-skycam1_20240424T093802_defisheyed_low_exp.jpg
ita-rome1-skycam1_20240426T094803_defisheyed_low_exp.jpg
ita-rome1-skycam1_20240427T092203_defisheyed_low_exp.jpg
ita-rome1-skycam1_20240428T093502_defisheyed_low_exp.jpg
ita-rome1-skycam1_20240430T094403_defisheyed_low_exp.jpg

Figure 106: Sky camera acquisitions over Rome during Sentinel-3 OLCI overpass

ita-rome1-skycam1_20240401T093502_defisheyed_low_exp_NN.png
ita-rome1-skycam1_20240403T094402_defisheyed_low_exp_NN.png
ita-rome1-skycam1_20240404T095703_defisheyed_low_exp_NN.png
ita-rome1-skycam1_20240405T093103_defisheyed_low_exp_NN.png
ita-rome1-skycam1_20240407T094003_defisheyed_low_exp_NN.png
ita-rome1-skycam1_20240411T093702_defisheyed_low_exp_NN.png
ita-rome1-skycam1_20240412T094903_defisheyed_low_exp_NN.png
ita-rome1-skycam1_20240413T092403_defisheyed_low_exp_NN.png
ita-rome1-skycam1_20240415T093303_defisheyed_low_exp_NN.png
ita-rome1-skycam1_20240416T094603_defisheyed_low_exp_NN.png
ita-rome1-skycam1_20240418T095503_defisheyed_low_exp_NN.png
ita-rome1-skycam1_20240419T092903_defisheyed_low_exp_NN.png
ita-rome1-skycam1_20240420T094203_defisheyed_low_exp_NN.png
ita-rome1-skycam1_20240422T095203_defisheyed_low_exp_NN.png
ita-rome1-skycam1_20240423T092603_defisheyed_low_exp_NN.png
ita-rome1-skycam1_20240424T093802_defisheyed_low_exp_NN.png
ita-rome1-skycam1_20240426T094803_defisheyed_low_exp_NN.png
ita-rome1-skycam1_20240427T092203_defisheyed_low_exp_NN.png
ita-rome1-skycam1_20240428T093502_defisheyed_low_exp_NN.png
ita-rome1-skycam1_20240430T094403_defisheyed_low_exp_NN.png

Figure 107: Classified sky camera acquisitions over Rome during Sentinel-3 OLCI overpass

The distribution between clear and cloud observations is uneven during April. After the installation of new sky cameras in Rome, the previously used classifier for Rome was not working as expected. Therefore, the classifier trained for Valencia was used. As described in previous reports, the SC classification seems to have a small cloud bias due to sun interference. Nevertheless, the April acquisitions are partially influenced by thin high-altitude clouds that are often undetected by the OLCI cloud mask. But those clouds are so thin, that they are nearly unrecognizable in the OLCI products.

Figure 108 shows the validation results for the OLCI cloud flags including the margin. Only OLCI observations with a OZA below 30 have been considered to lower the influence of parallax between the OLCI observation and the SC observation. This time the SC suffers a little bit from a cloud bias as explained above.

When neglecting the margin (see Figure 109) the performance (BOA) is only a tiny bit better.

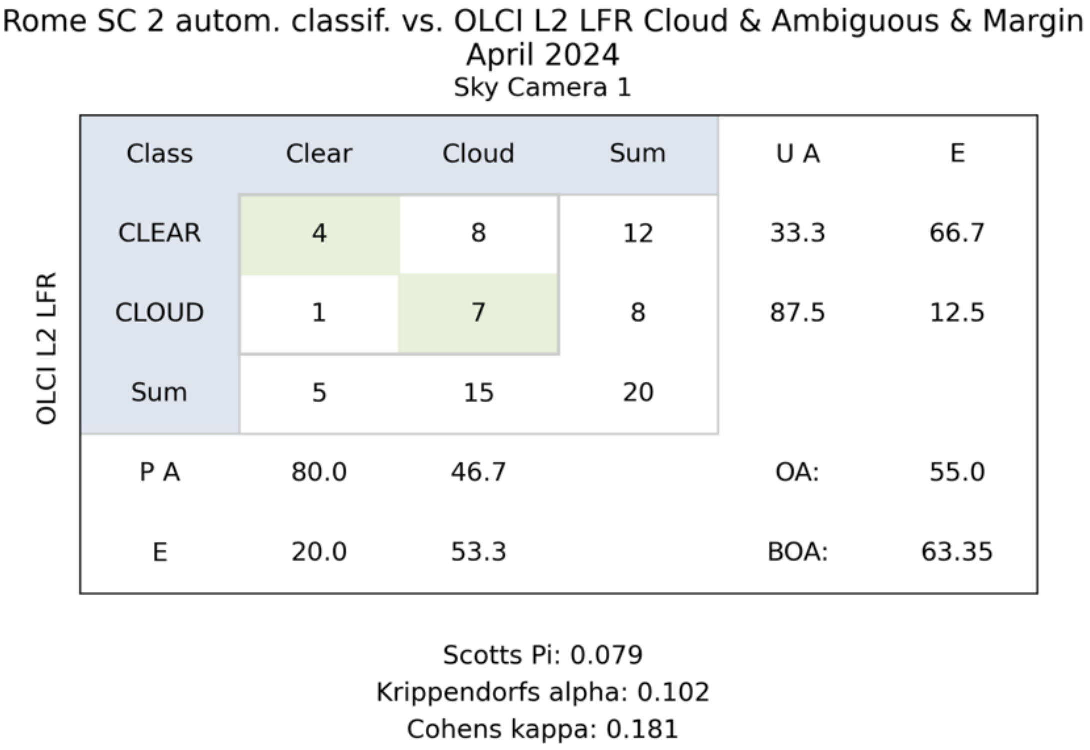

Rome SC 2 autom. classif. vs. OLCI L2 LFR Cloud & Ambiguous & Margin
April 2024
Sky Camera 1

OLCI L2 LFR

Class	Clear	Cloud	Sum	U A	E
CLEAR	4	8	12	33.3	66.7
CLOUD	1	7	8	87.5	12.5
Sum	5	15	20		
P A	80.0	46.7		OA:	55.0
E	20.0	53.3		BOA:	63.35

Scotts Pi: 0.079
Krippendorfs alpha: 0.102
Cohens kappa: 0.181

Figure 108: Confusion matrix showing validation results for OLCI L2 cloud screening including margin against SC1 automated classification.

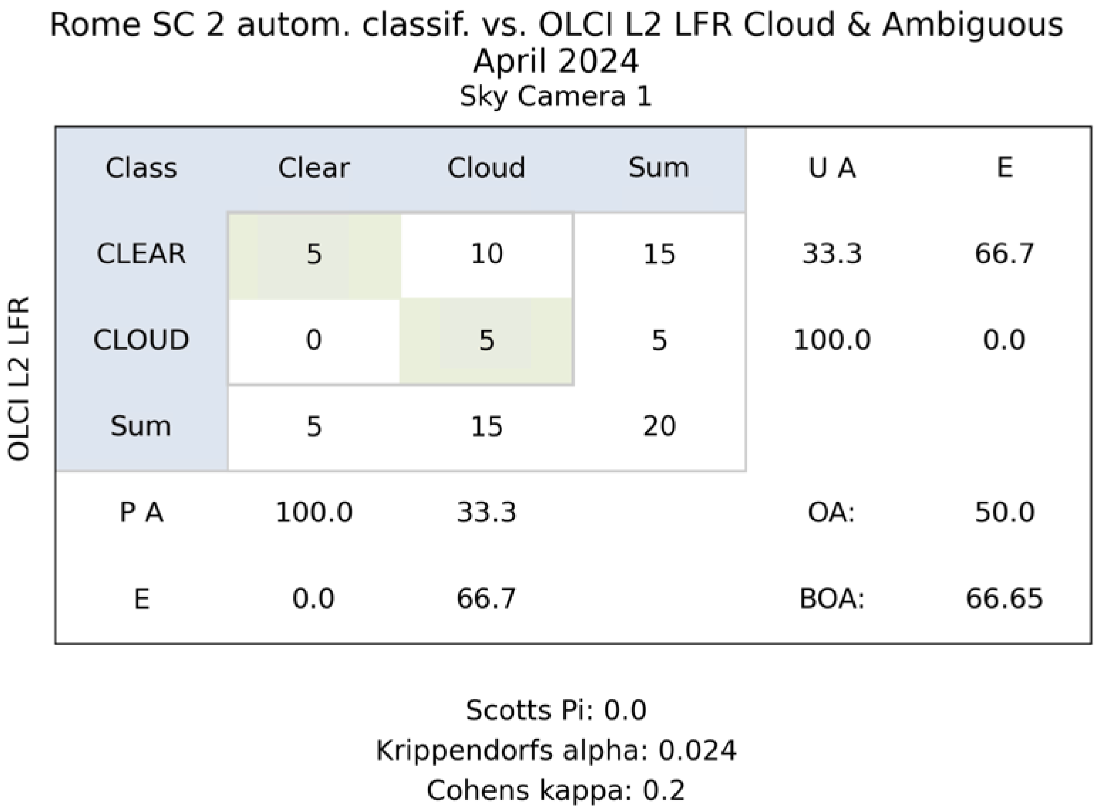

Rome SC 2 autom. classif. vs. OLCI L2 LFR Cloud & Ambiguous
April 2024
Sky Camera 1

OLCI L2 LFR

Class	Clear	Cloud	Sum	U A	E
CLEAR	5	10	15	33.3	66.7
CLOUD	0	5	5	100.0	0.0
Sum	5	15	20		
P A	100.0	33.3		OA:	50.0
E	0.0	66.7		BOA:	66.65

Scotts Pi: 0.0
Krippendorfs alpha: 0.024
Cohens kappa: 0.2

Figure 109: Confusion matrix showing validation results for OLCI L2 cloud screening excluding margin against SC1 automated classification

4.2.1.3 Valencia

Figure 114 and Figure 115 show the prototype validation results for the Valencia site in April 2024. The weather in April around Valencia is mostly dry, with a few thick cloud covered days, but also some additional days with thinner cloud cover (see Figure 110 and Figure 111).

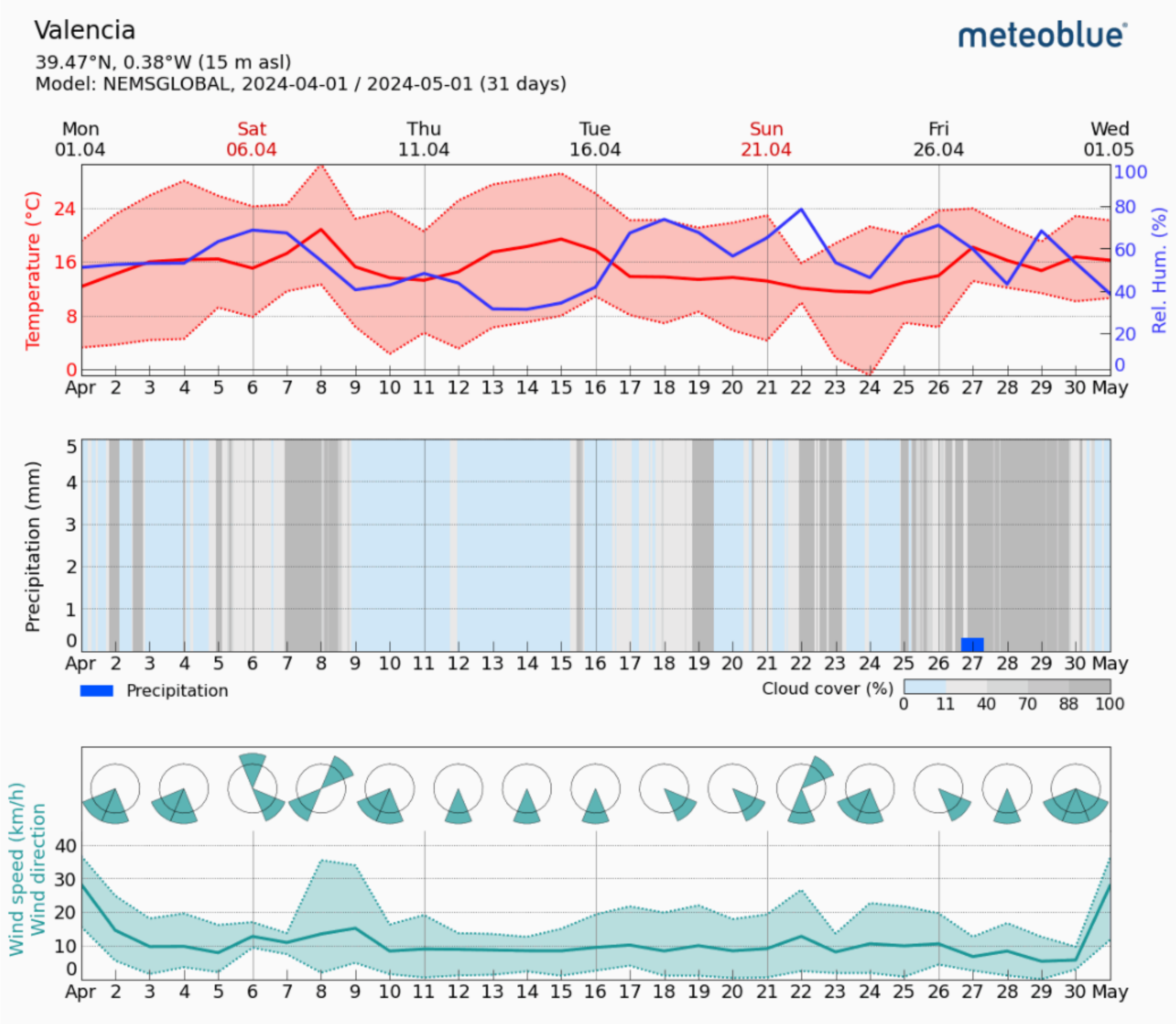

Figure 110: Temperature, cloud cover and precipitation Valencia, April 2024 (source: https://www.meteoblue.com/en/weather/historyclimate/weatherarchive/valencia_spain_2509954?fcstlength=1m&year=2024&month=4)

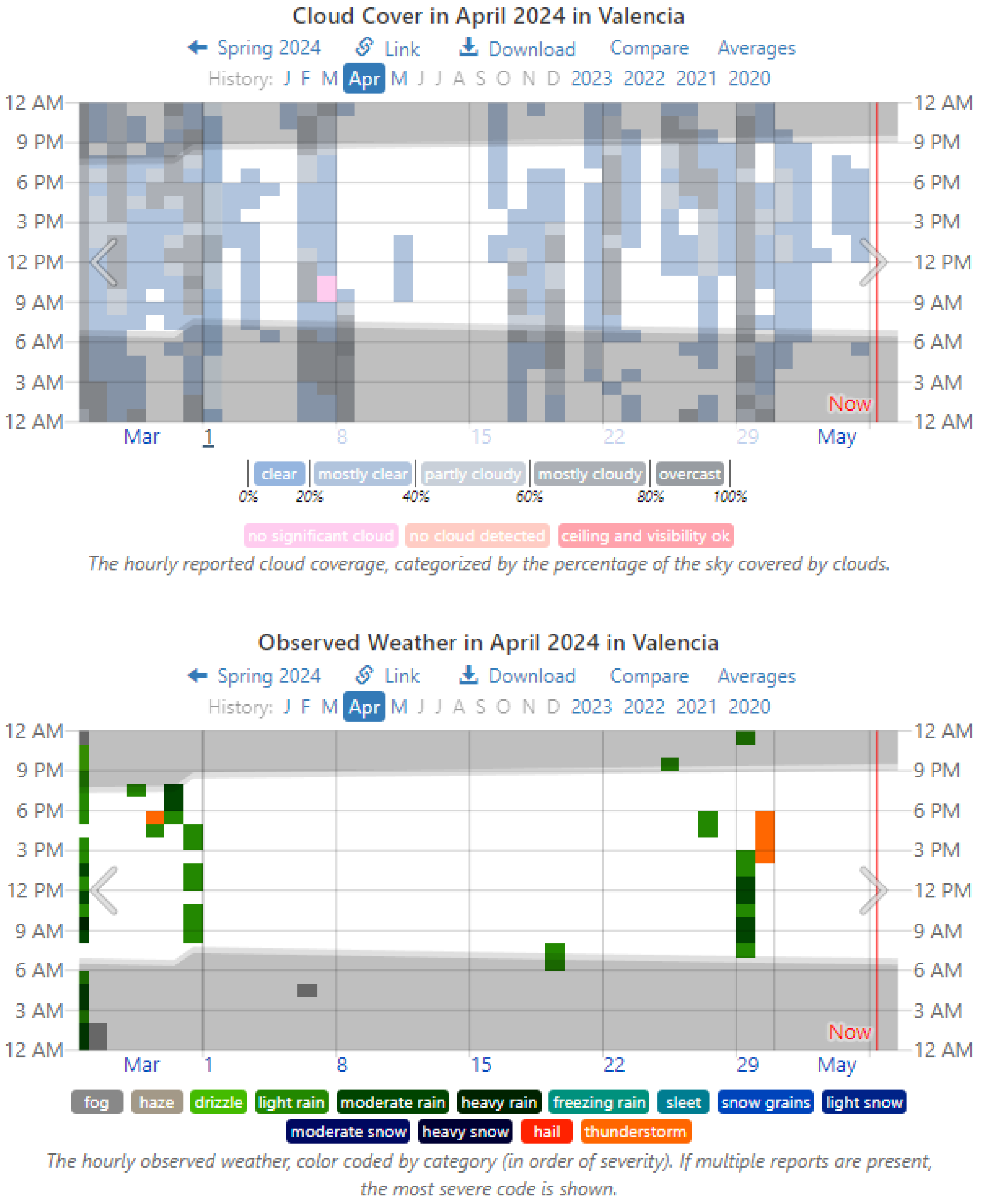

Figure 111: Cloud observations and precipitation Valencia, April 2024 (source: https://weatherspark.com/h/m/42614/2024/04/Historical-Weather-in-April-2024-in-Valencia-Spain#Figures-CloudCover)

In April, there have been 15 acquisitions below 30 degree OZA. Nine to ten of the SC observation show mostly clear sky conditions (see Figure 112). Even though the sun is close to the centre of all acquisitions, the SC classification (see Figure 113) shows only a little cloud bias. When the majority of the reference window, used for the classification, is classified as sun, those observations are not used for the comparison.

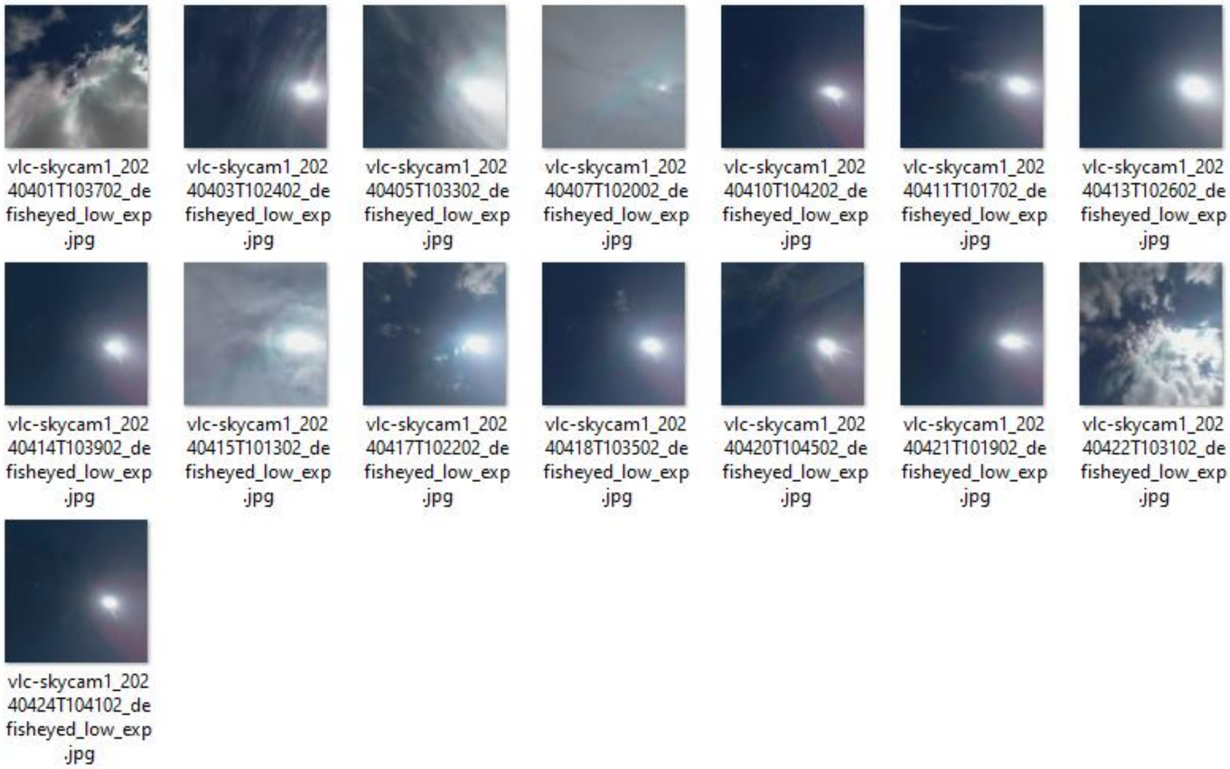

Figure 112: Sky camera acquisitions over Valencia during Sentinel-3 OLCI overpass

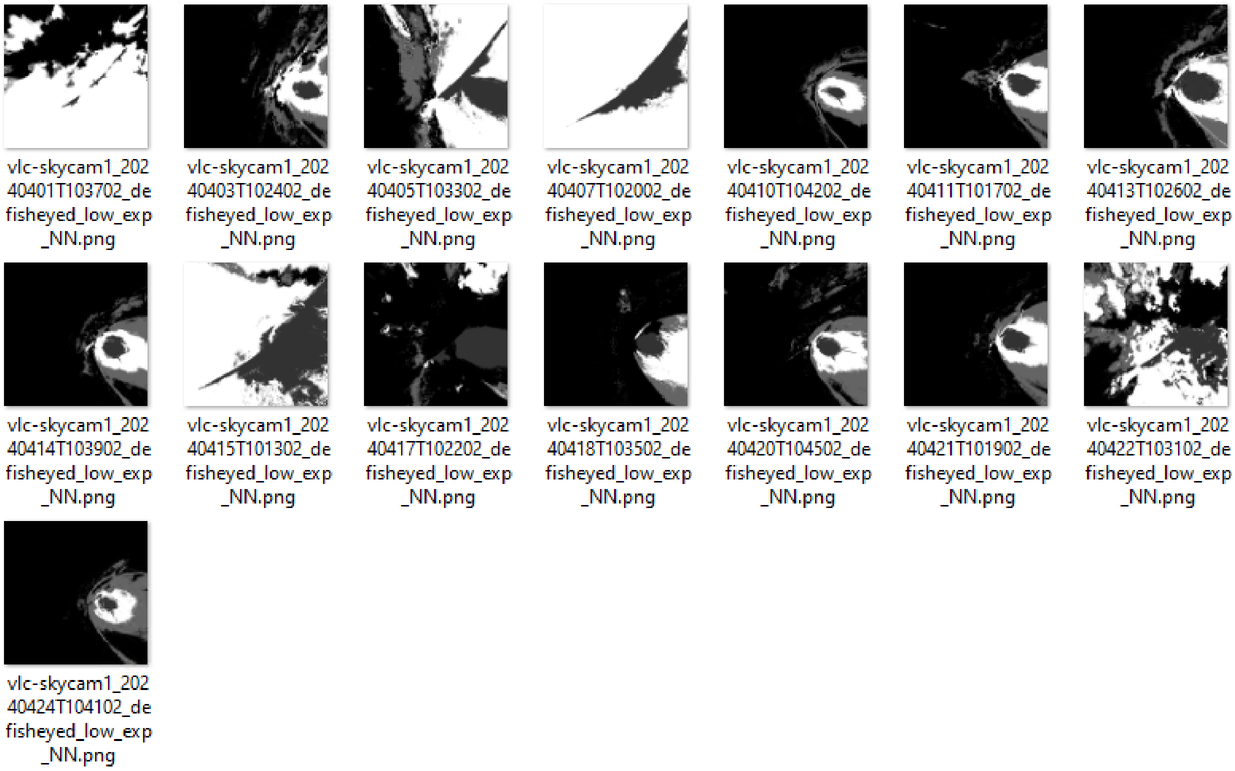

Figure 113: Classified sky camera acquisitions over Valencia during Sentinel-3 OLCI overpass

Figure 114 shows the validation results for the OLCI cloud flags including the margin. Only OLCI observations with a OZA below 30 have been considered to lower the influence of parallax between the OLCI observation and the SC observation.

The SC classification of the Valencia SC is better trained to identify the sun in the images therefore, the interference of sun is a bit better, leading to less false classifications. If pixels of the SC image are classified as sun, and the majority of the used window of the SC image shows mostly sun, those acquisitions are neglected for the comparison.

The results show 100% agreement between the sky camera reference and the OLCI L2 cloud masking, when using the margin. Figure 115 shows the results without usage of the CLOUD_MARGIN flag. This time, neglecting the margin has a small impact on the results.

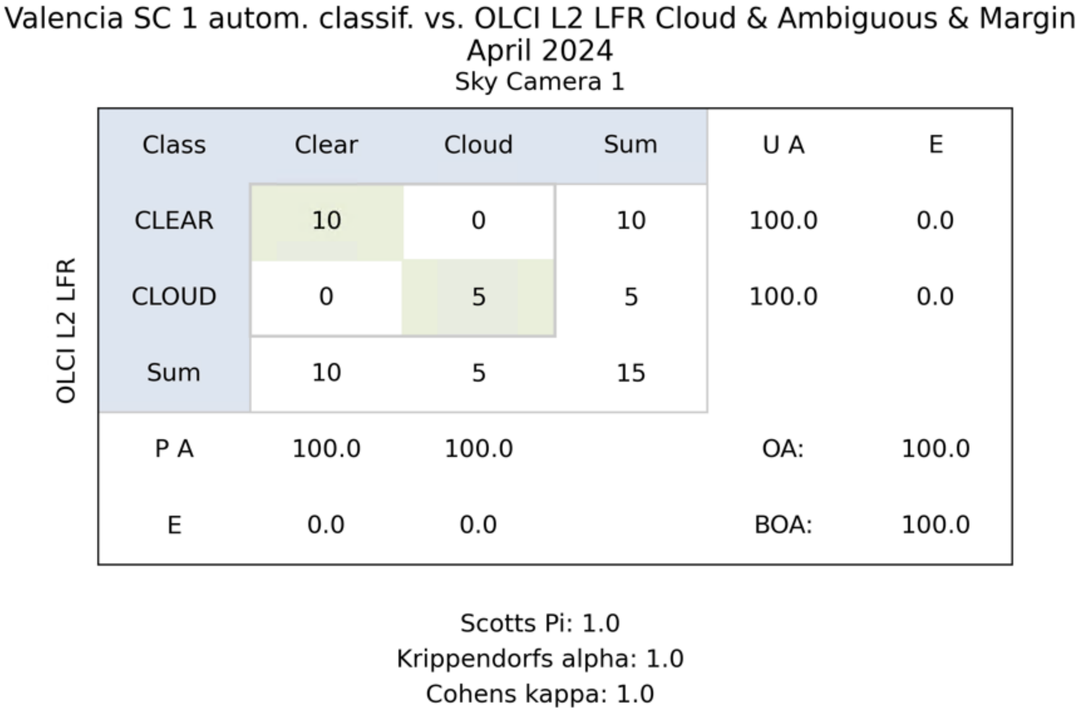

Valencia SC 1 autom. classif. vs. OLCI L2 LFR Cloud & Ambiguous & Margin
April 2024
Sky Camera 1

OLCI L2 LFR

Class	Clear	Cloud	Sum	U A	E
CLEAR	10	0	10	100.0	0.0
CLOUD	0	5	5	100.0	0.0
Sum	10	5	15		
P A	100.0	100.0		OA:	100.0
E	0.0	0.0		BOA:	100.0

Scotts Pi: 1.0
Krippendorfs alpha: 1.0
Cohens kappa: 1.0

Figure 114: Confusion matrix showing validation results for OLCI L2 cloud screening including margin against SC1 automated classification

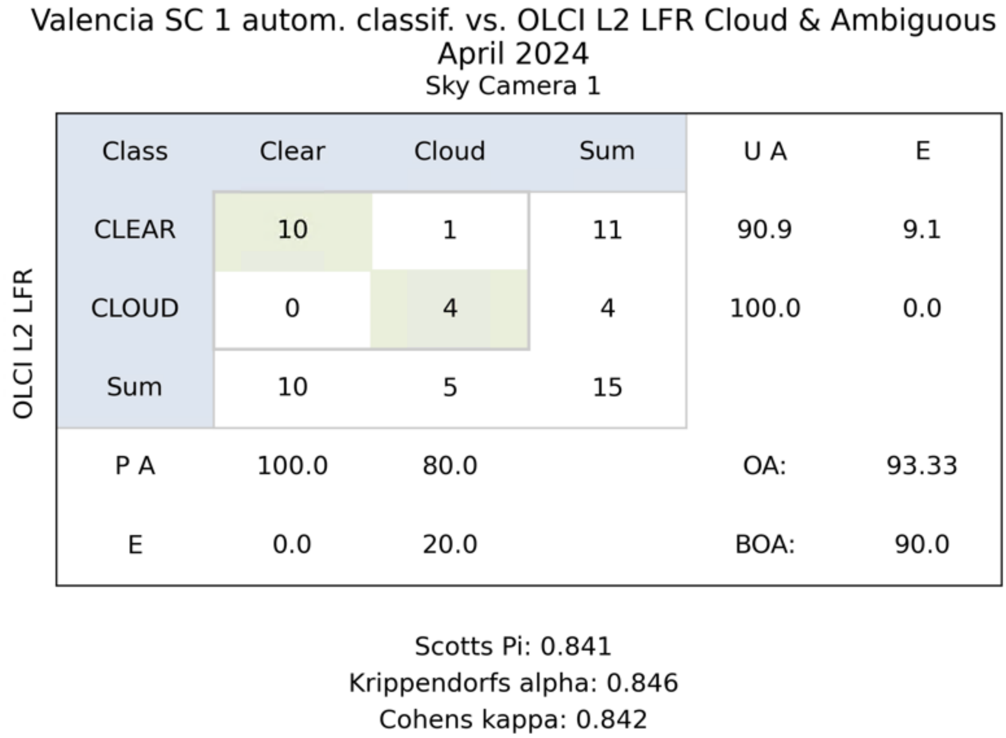

Valencia SC 1 autom. classif. vs. OLCI L2 LFR Cloud & Ambiguous
April 2024
Sky Camera 1

OLCI L2 LFR

Class	Clear	Cloud	Sum	U A	E
CLEAR	10	1	11	90.9	9.1
CLOUD	0	4	4	100.0	0.0
Sum	10	5	15		
P A	100.0	80.0		OA:	93.33
E	0.0	20.0		BOA:	90.0

Scotts Pi: 0.841
Krippendorfs alpha: 0.846
Cohens kappa: 0.842

Figure 115: Confusion matrix showing validation results for OLCI L2 cloud screening excluding margin against SC1 automated classification

5 Validation of Integrated Water Vapour over Land & Water

We continuously investigate the temporal evolution of quality measures of integrated water vapour, when comparing SUOMI NET (Ware et al. 2000) with reduced resolution data of OLCI L2 non-time-critical. All data until March 2022 has been acquired from EUMETSAT CODA, all data from Apr 2022 on has been downloaded from EUMETSAT's datastore (collection id: EO:EUM:DAT:0410). No significant changes since last reporting have been detected. 44291(OLCI-A) and 28884 (OLCI-B) valid matchups within the period of June 2016 (OLCI-A) January 2019 (OLCI-B) to end of April 2024 have been analysed.

For the cloud detection, the standard L2 cloud-mask has been applied (including the cloud ambiguous and cloud margin flags). The comparison of OLCI and GNSS shows a very high agreement (Figure 116). The correlation between both quantities is around 0.98. The root-mean-squared-difference (*rmsd*) is 1.9 -2.1 kg/m^2. The systematic overestimation by OLCI is 11%-12%. The bias corrected *rmsd* is around 1.3 kg/m^2.

The temporal evolution of several quality measures (Figure 117), indicates small seasonal variations, in particular for the *rmsd*. They are certainly related to retrieval assumptions.

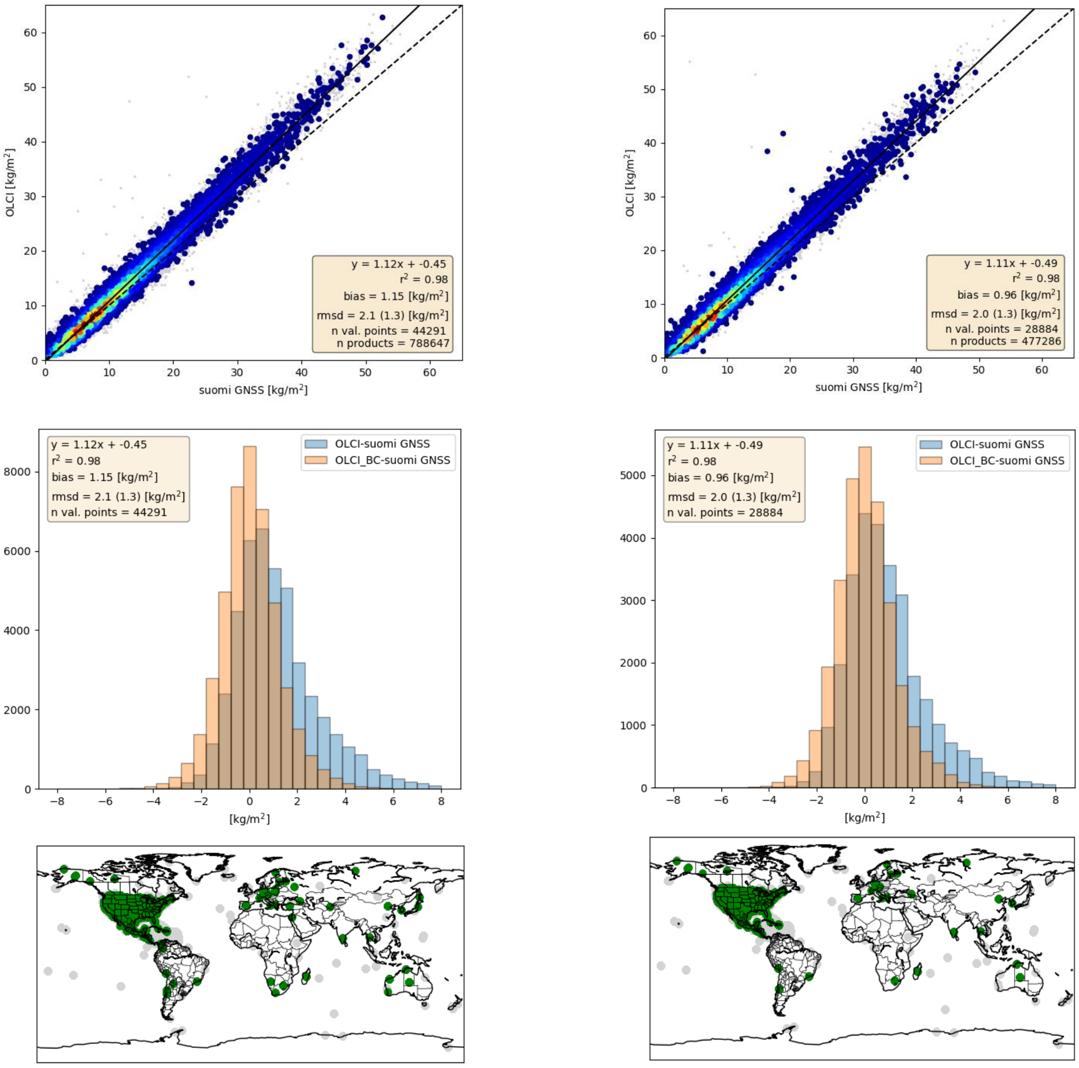

Figure 116: Upper: Scatter plot of the IWV products, derived from OLCI (A left, B right) above land and from SUOMI NET GNSS measurements. Middle: Histogram of the difference between OLCI (A: left, B: right) and GNSS (blue: original OLCI, orange: bias corrected OLCI). Lower: Positions of the GNSS (A: left, B: right).

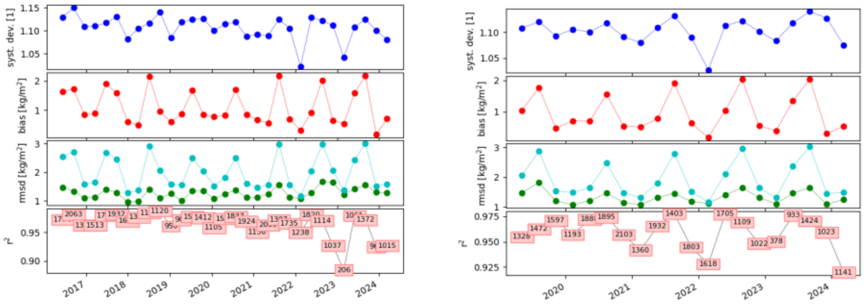

Figure 117: Temporal evolution of different quality measures for OLCI A (left) and OLCI B (right) with respect to SUOMI Net. From top to bottom: systematic deviation factor, bias, root mean squared difference (with and without bias correction), explained variance (number in boxes are the numbers of matchups)

6 Level 2 SYN products validation

6.1 SYN L2 SDR products

There have been no new results during the reporting period. The latter figures (reported in the OLCI Data Quality Report covering March 2024) are considered valid.

6.2 SY_2_VGP, SY_2_VG1 and SY_2_V10 products

The similarity of SYN VGT like products with the PROBA-V archive is evaluated through intercomparison of 10-daily composites extractions over LANDVAL [1] sites. Since there is no overlap with the PROBA-V nominal operational phase and no PROBA-V Collection 2 climatology is available yet, direct comparison is done by comparing the SY_2_V10 NTC products starting January/2021 with PROBA-V S10-TOC products since January/2017.

The temporal evolution of statistics results below are based on intercomparison over the entire periods up to April/2024. The scatterplots are based on intercomparison between SY_2_V10 products of April/2024 with PROBA-V Collection 2 S10-TOC products of April/2020.

Products availability

Availability of SY_2_VG1 and SY_2_V10 products is checked through an automated query and download via the Copernicus Data Space Ecosystem feeding the products database of the Belgian Collaborative Ground Segment (Terrascope, www.terrascope.be). For the month April/2024, there are no missing data or empty files.

Statistical consistency

The scatter density plots with geometric mean regression equation, coefficient of determination (R^2) and APU statistics based on intercomparison between SY_2_V10 products of April/2024 with PROBA-V Collection 2 products of April/2020 are shown in Figure 118. The APU statistics are defined as: Accuracy (A) or average bias, Precision (P) or the standard deviation of the bias, and Uncertainty (U) or the Root Mean Squared Distance. Accuracy is best for BLUE (< 1%) and slightly less good for the other bands (up to 4%). The relatively large values for Precision (large scatter, low R^2) are caused by the fact that acquisitions of two different years are compared.

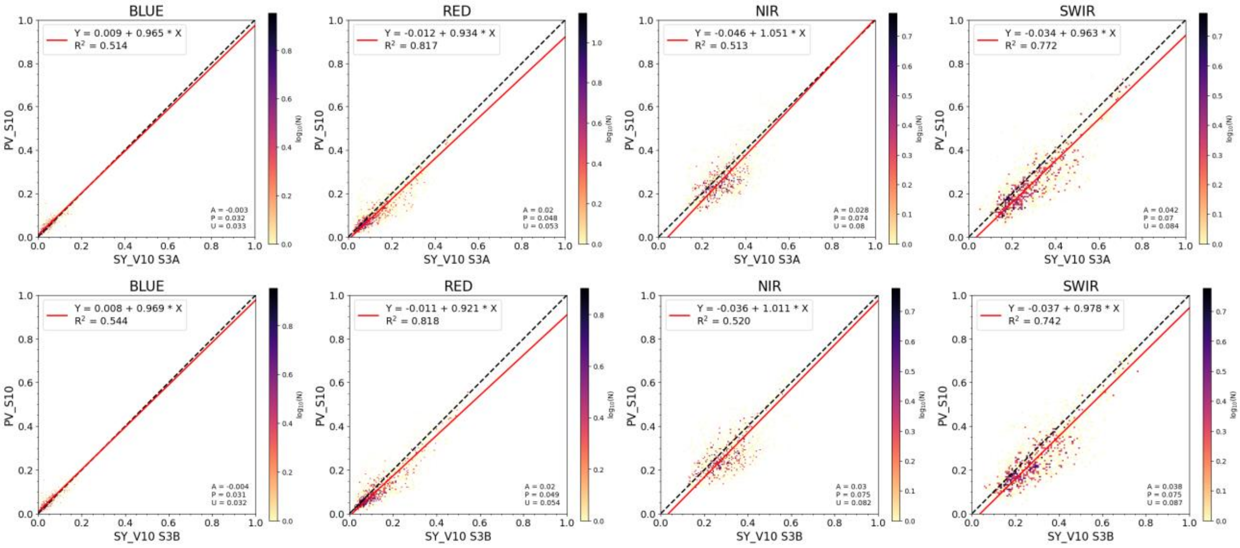

Figure 118: Scatter density plots between SY_V10 S3A (top) or S3B (bottom) and PROBA-V C2 S10-TOC for BLUE, RED, NIR and SWIR bands (left to right), April/2024 vs. April/2020

Temporal consistency

The temporal evolution of APU statistics derived from intercomparison of SY_2_V10 NTC products July/2020 – April/2024 with those of PROBA-V S10-TOC July/2016 – April/2020 (Figure 119). The APU statistics show stable evolution over time, although some seasonal pattern is observed for the mainly the SWIR channel, and to a lesser extent the RED and NIR channel. The temporal behaviour is stable, except for a strong discontinuity for the SWIR band, with improved statistics at the end of July/2023. From 18/07/2023 (for S3B) and 25/07/2023 (for S3A) an updated processing baseline is in operations, including application of SLSTR calibration factors, and aligning the spectral resampling to PROBA-V. As a result, the statistical consistency for RED, NIR and SWIR has improved in comparison to previous periods, which were affected by erroneous spectral resampling and the SLSTR calibration offset (in bands S5 and S6).

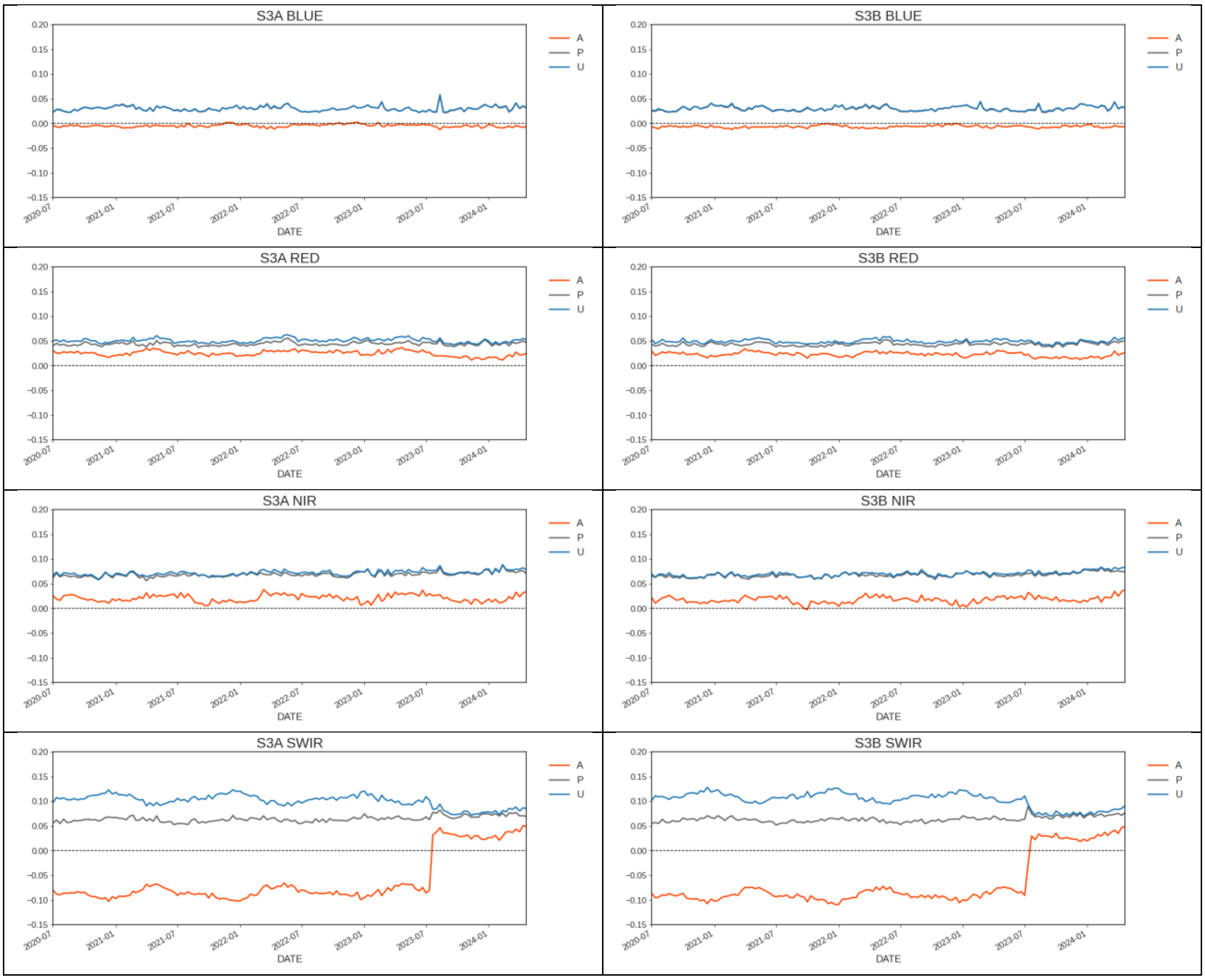

Figure 119: Temporal evolution of APU statistics between SY_2_V10 S3A (left) or S3B (right) and PROBA-V S10-TOC for BLUE, RED, NIR and SWIR bands (top to bottom), July/2020 – April/2024 (S3 SYN VGT) vs. July/2016 – April/2020 (PROBA-V)

Figure 120 shows the temporal evolution of APU statistics derived from the intercomparison of SY_2_V10 NTC products based on S3A with those based on S3B July/2020 – April/2024. The APU statistics show overall a stable temporal evolution, except for a strong discontinuity for SWIR, related to the different timing of the processing baseline update for S3A resp. S3B (see above).

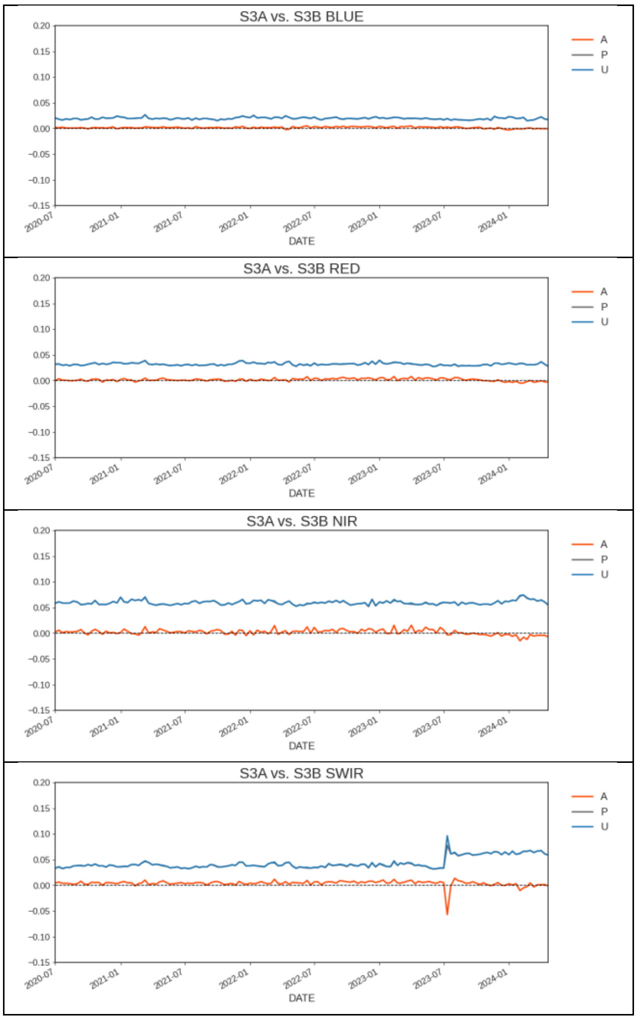

Figure 120: Temporal evolution of APU statistics between S3A_SY_2_V10 and S3B_SY_2_V10 for BLUE, RED, NIR and SWIR bands (top to bottom), July/2020 – April/2024

References

[1] B. Fuster *et al.*, “Quality Assessment of PROBA-V LAI, fAPAR and fCOVER Collection 300 m Products of Copernicus Global Land Service,” *Remote Sens.*, vol. 12, no. 6, p. 1017, Mar. 2020, doi: 10.3390/rs12061017.

6.3 SYN L2 AOD NTC products

In the previous report, the improvement of the validation statistics was shown as a consequence of implementing the SLSTR TOA correction coefficients. The current report investigates whether spatial changes in validation statistics occurred by looking at validation results per AERONET station.

Since the correction coefficients have been included on flow and direct intercomparison (analysing the same period retrieved before and after correction) is not possible, some “tricks” should be applied to get as reliable intercomparison results as possible.

Our analysis is based on a comprehensive comparison of results for three distinct periods, namely August through March of the years 2020/2021 (P1), 2021/2022 (P2), and 2022/2023 (P3), with the control period (Pc) of 2023/2024 when correction coefficients were applied. This meticulous approach ensures the reliability and accuracy of our findings.

For four periods (P1-P3 and Pc), validation statistics are shown in Figure 121 for

- **A**ll **A**vailable **M**atchups (**AAM**, left panel)
- matchups which satisfy two following criteria (**NPM**, right panel): the **N**umber of retrieved Sy_2 AOD **P**ixels (in 11*11 pixels area around AERONET) in a **M**atchup should be at least 5, and the number of AERONET measurements (in ±30 min around the satellite overpass) should be at least 3 (right panel).

The AAM approach does not account for the number of Sy retrieved pixels and AERONET measurements per matchup. In this approach, a small fraction of the retrieved/measured pixels per matchup may bias validation statistics.

The NPM approach allows for removing matchups with “unstable” (=low coverage) conditions (e.g., partly cloud-contaminated or flagged for different reasons), in which syAOD is often highly biased to the aAOD. The NPM approach removed approximately 20% of matchups from the analysis for P1-P3 and 34% for Pc. Note that (i) this approach does not remove all outliers and (ii) ‘good’ matchups with AERONET stations located at the sides of the track (the area retrieved around the AERONET station is less than 11*11 pixels because of the side location) are also removed with this approach.

We recommend looking at both AAM and NPM validation results. Removing the outliers allows us to see the retrieval approach's general performance. However, it is essential to know the existing outliers, which should be further investigated to understand how to improve the retrieval approach.

As reported earlier, applying TOA coefficients allowed AAM's global correlation coefficient to increase from 0.61/0.60/0.61 (for P1/P2/P3, respectively) to 0.66 in P4. Rms has decreased (from 0.25 to 0.20), and the fraction of matchups satisfying GCOS requirements has increased (25% to 34%). For NPM, the correlation coefficient increased from 0.68/0.73/0.71 (for P1/P2/P3, respectively) to 0.76 in P4.

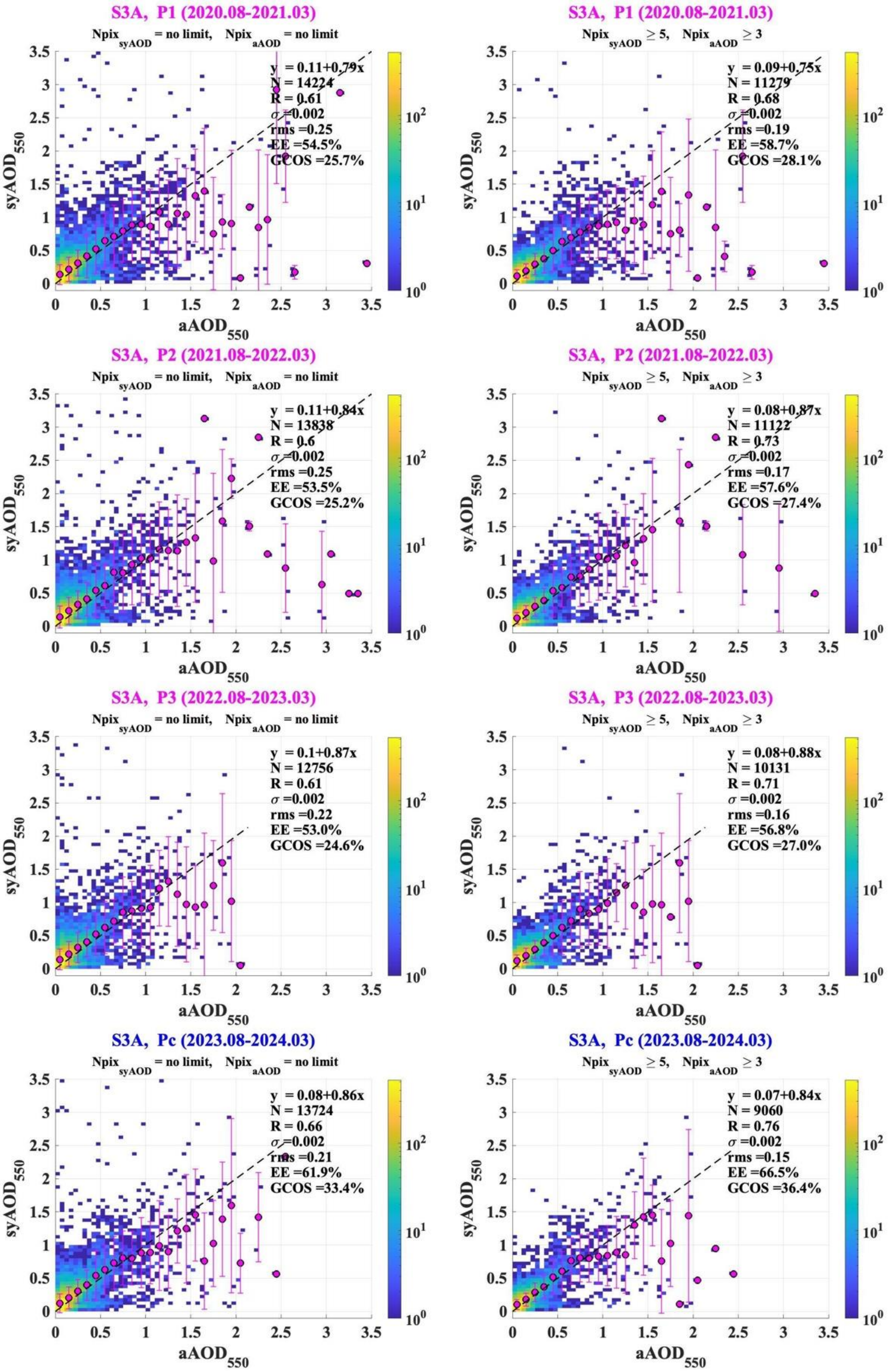

Figure 121: Scatter density plots between SY_2 AOD (syAOD) and AERONET AOD (aAOD) for four periods (P1, P2, P3 and Pc, defined in the title; panels top down) for all matchups (left panel) and matchups which satisfy the number of retrieved pixels (Npix$_{syAO}$D) and the number of measured AOD (Npix$_{aAOD}$) criteria (defined in the title).

Spatial distribution of validation statistics before and after TOA correction

Outliers strongly bias the comparison results, especially in the per-station analysis, where the number of matchups is considerably lower (and thus, statistics are more sensitive to outliers) than in the global/regional analysis.

To obtain representative inter-comparison results for three periods (Pc to P1, P2, and P3), AOD conditions within periods must be unified as closely as possible. Removing the outliers is critical for smoothing the differences in AOD ranges between different periods. (Note that the removal of the outliers is not required if the same period has been retrieved with different retrieval approaches, or, in our case, before and after the application of TOA correction coefficients).

To identify and remove **H**ighly **B**iased **M**atchups (**HBM**) left after applying NPM, we applied additional criteria for high AOD (syAOD>0.75) cases. If syAOD was three times higher than the aAOD (syAOD>3*aAOD), the matchup has been removed from the inter-comparison analysis. Those criteria were chosen as woring best to recognise outliers by examining how validation statistics and coverage are changing with testing different syAOD and syAOD offset to aAOD values.

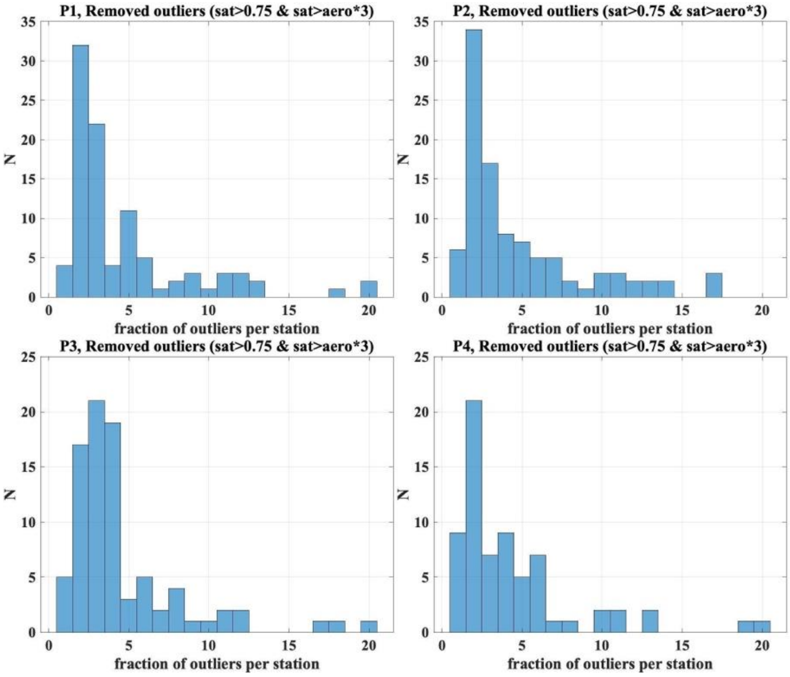

*Figure 122 For four tested periods (P1-P3, Pc), histograms for a fraction (per AERONET station) of the outliers identified with criteria: syAOD>0.75 and syAOD>3*aAOD.*

For most AERONET stations, the fraction of the outliers identified as HBM is below 5 % (Figure 122).

Validation statistics per AERONET station for four periods (P1-P3 and Pc) were calculated after removing the matchups that did not satisfy NPM and HBM criteria. The minimum required number of matchups left per station per period was set to 9.

The global spatial distribution of the correlation coefficients (R), bias, and rms is shown on the left panels of Figure 123 to Figure 125, respectively. The difference between the results for Pc and P1, P2, and P3 is shown on the right panels of the corresponding figures.

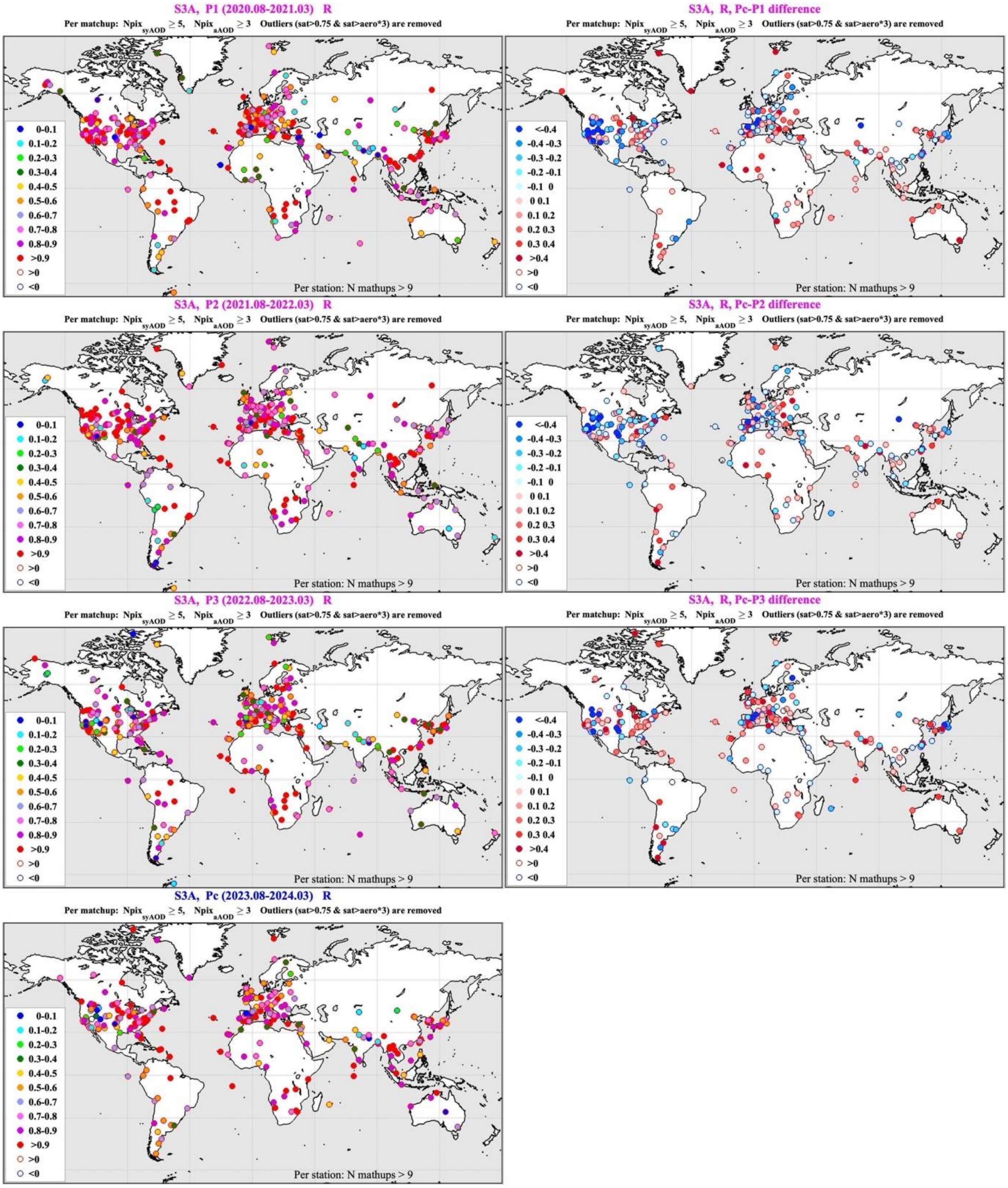

Figure 123: Left panel: for P1, P2, P3 and Pc (top-down), correlation coefficients (R) for AERONET stations. Right panel: difference in R between Pc and P1, P2 and P3 (top-down).

After applying TOA correction coefficients, R has increased for nearly half of the stations and decreased for the other half. R has generally increased in central Europe, central Africa (compared to P1 and P2), and east of the US (Figure 123). R decreased in the west of the US.

Bias (Figure 124) and rms (Figure 125) have lowered for about 2/3 of AERONET stations. No clear regions for preferably negative or positive biases have been recognised However, some worsening of the statistics can be recognised in coastal (and elevated) areas.

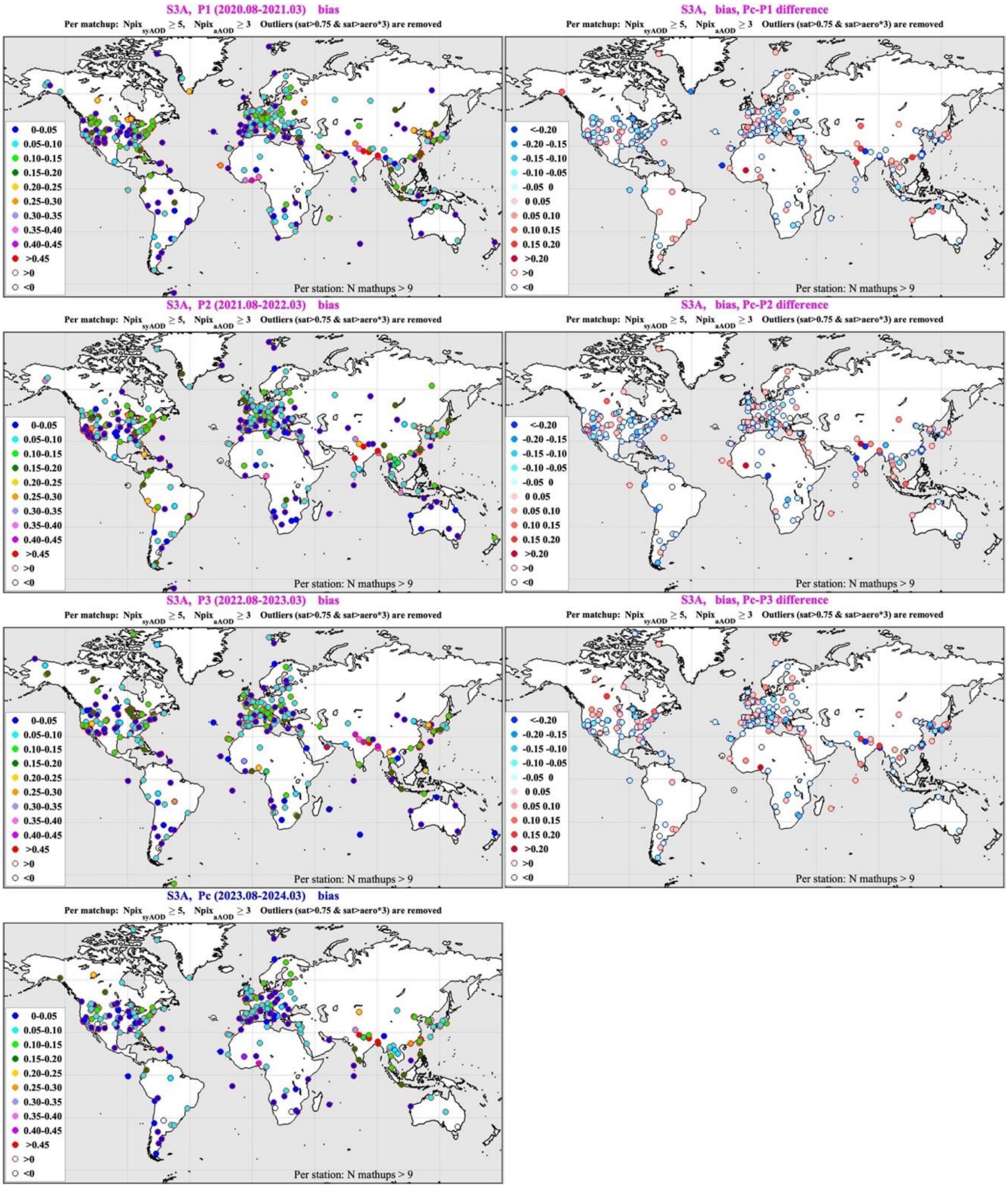

Figure 124: Left panel: for P1, P2, P3 and Pc (top-down), syAOD bias to aAOD, for AERONET stations. Right panel: difference in biases between Pc and P1, P2 and P3 (top-down).

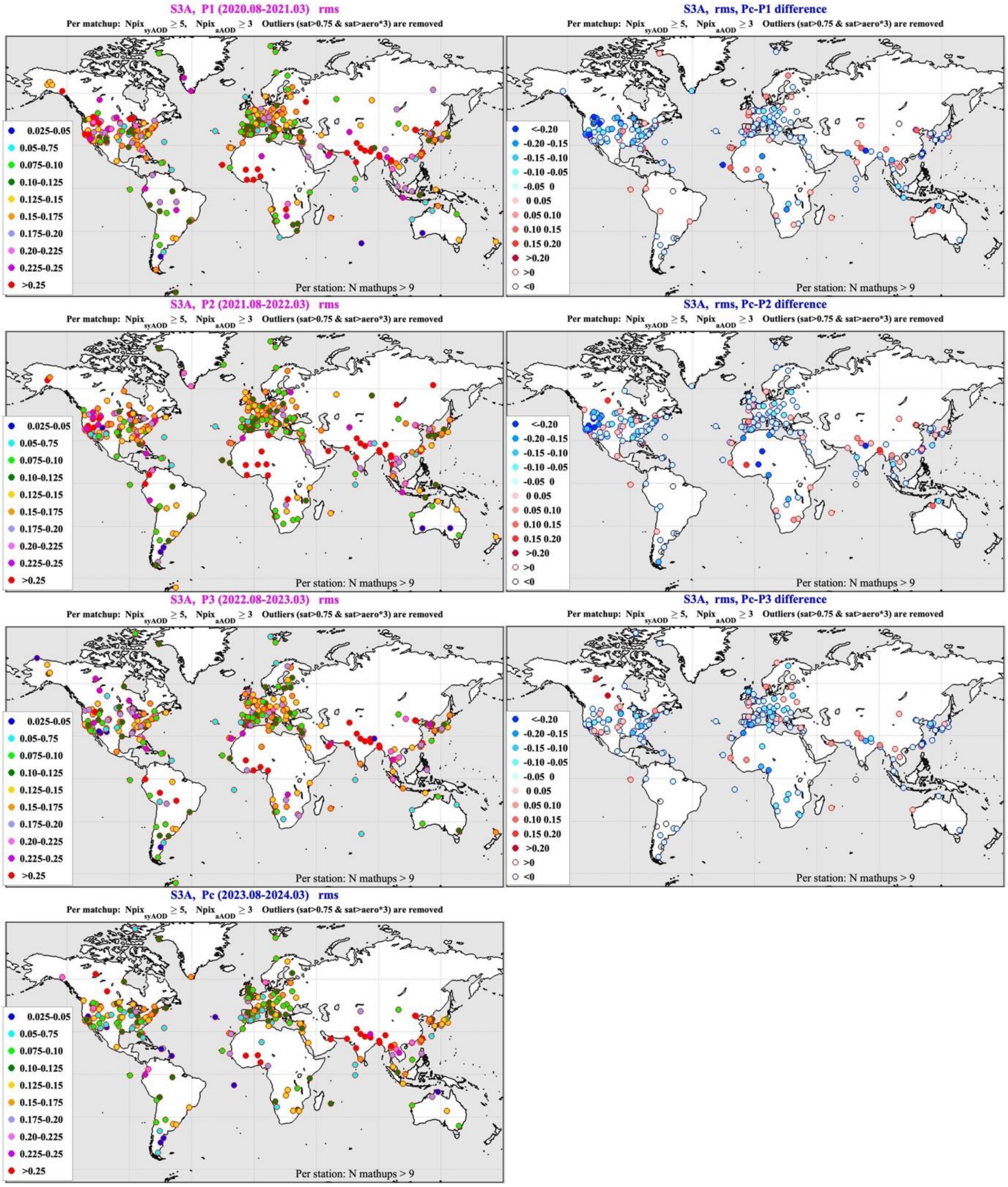

Figure 125: Left panel: for P1, P2, P3 and Pc (top-down), rms for AERONET stations. Right panel: difference in rms between Pc and P1, P2 and P3 (top-down).

For many stations, changes in statistics were positive and negative if results were compared between Pc and three other periods (P1, P2, and P3).

In Figure 126, we plot AERONET stations where changes in validation statistics showed the same tendencies for all three periods. A steady decline in R can be reported for the western US, while in the eastern US, the changes in R remain positive. Bias and rms have increased in some coastal, elevated, or bright surface stations.

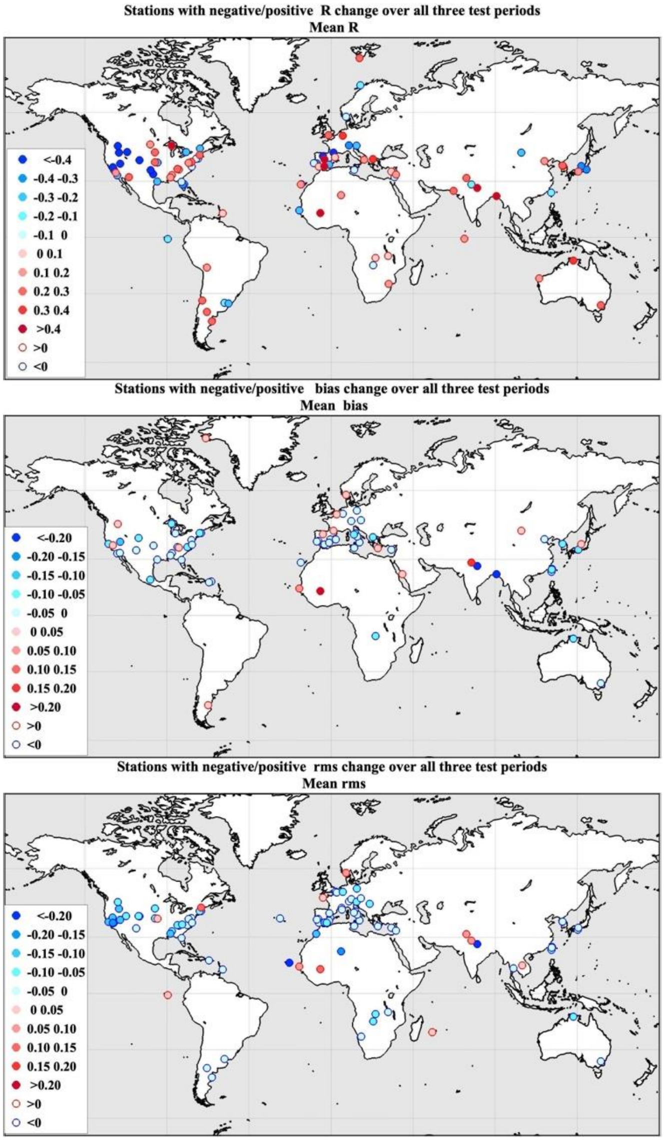

Figure 126: AERONET stations where changes in statistics – R, bias, rms (panels top-down)- are stable (only positive or only negative) if comparing the Pc validation results with ones for three periods (P1, P2 or P3).

To get a clearer picture of the implementation of the TOA correction coefficients, Timo H. Virtanen suggested looking separately at results from dual- and single-view retrieval approaches (assuming that the effect from implementing the same coefficients to nadir and oblique reflectances can be cancelled in the dual approach). This check requires further development of the FMI matchup tool (used for validation since August 2023), which currently does not include a capability for separation between dual- and single-approach retrieved pixels.

7 Events

For OLCI-A, five Radiometric Calibration sequences have been acquired during the reported period:

- S01 sequence (diffuser 1) on 03/04/2024 10:54 to 10:56 (absolute orbit 42331)
- S01 sequence (diffuser 1) on 08/04/2024 07:02 to 07:04 (absolute orbit 42400)
- S01 sequence (diffuser 1) on 12/04/2024 20:26 to 20:27 (absolute orbit 42465)
- S01 sequence (diffuser 1) on 20/04/2024 05:08 to 05:10 (absolute orbit 42570)
- S01 sequence (diffuser 1) on 30/04/2024 02:27 to 02:29 (absolute orbit 42711)

For OLCI-B, four Radiometric Calibration sequences have been acquired during the reported period:

- S01 sequence (diffuser 1) on 07/04/2024 10:11 to 10:13 (absolute orbit 30994)
- S01 sequence (diffuser 1) on 11/04/2024 18:32 to 18:34 (absolute orbit 31056)
- S01 sequence (diffuser 1) on 19/04/2024 04:56 to 04:57 (absolute orbit 31162)
- S01 sequence (diffuser 1) on 28/04/2024 17:49 to 17:51 (absolute orbit 31298)

8 Appendix A

All Data Quality Reports, as well as past years Data Quality Reports and Annual Performance Reports, are available on dedicated pages in Sentinel Online website, at:

- S2 MSI L1C Data Quality Report
- S2 MSI L2A Data Quality Report
- S3 OLCI Data Quality Reports
- S3 SLSTR Data Quality Reports
- OPT Annual Performance Report Year 2023 (PDF document)

End of document